Western Graduate&PostdoctoralStudies

2-8-2017 12:00 AM

Convection in Corrugated Slots

Seyed Arman Abtahi, *The University of Western Ontario*

Supervisor: J.M. Floryan, *The University of Western Ontario*
A thesis submitted in partial fulfillment of the requirements for the Master of Engineering
Science degree in Mechanical and Materials Engineering
© Seyed Arman Abtahi 2017

Abstract

This thesis consists of two parts. The first part deals with the development of proper methodology, i.e. a spectrally accurate algorithm suitable for analysis of convection problems in corrugated slots. The second part is devoted to the study of natural convection in corrugated slots.

The algorithm uses the immersed boundary conditions (IBC) concept to deal with the irregular form of the solution domain associated with the presence of corrugated plates. The field equations are discretized on a regular domain surrounding the flow domain using Fourier expansions in the horizontal direction and Chebyshev expansions in the vertical direction. The boundary conditions are expressed in the form of constraints and the spectrally accurate discretization of these constraints has been proposed.

The buoyancy forces associated with the temperature difference between isothermal plates drive the natural convection. This temperature difference is expressed in terms of the Rayleigh number Ra and the analysis is limited to its subcritical values where no secondary motion takes place in the absence of corrugation. Corrugations have a sinusoidal form characterized by the wave number α, the upper and lower amplitudes and the phase difference between the upper and lower corrugation systems. They create horizontal temperature gradients which lead to the formation of vertical and horizontal pressure gradients which drive the motion regardless of the intensity of the heating. Presence of corrugations affects the conductive heat flow and creates the convective heat flow. The increase of the heat flow induced by the corrugations has been determined. The convection is qualitatively similar for all Prandtl numbers with the intensity of convection increasing for smaller Pr's and with the heat transfer augmentation increasing for larger Pr's.

Keywords: Spectral discretization, Natural Convection, Conduction, Immersed boundary conditions method, Linear solvers, Corrugation, Membrane

Co-Authorship Statement

This thesis is prepared in the monograph format. Chapters 2 and 3 are based on manuscripts which have been previously published or finalized for submission.

Chapter 2: A. Abtahi, M. Z. Hossain, J. M. Floryan, Spectrally Accurate Algorithm for Analysis of Convection in Corrugated Conduits, Journal of Computers and Mathematics with Applications, 72 (2016) 2636–2659.

Chapter 3: A. Abtahi & J. M. Floryan, Natural Convection in a Corrugated Slot, Journal of Fluid Mechanics, doi:10.1017/jfm.2017.73.

I am the first author on these manuscripts, with Professor Floryan and Dr. Hossain as co-authors. They taught me the basis of the IBC algorithm and convection.

Dedication

This is for you Mom and Dad, for believing in me.

Acknowledgements

First and foremost, I would like to appreciate my advisor Prof. J. M. Floryan for his continuous support of my study and research, for his patience, motivation, enthusiasm, and immense knowledge. His guidance helped me in all the time of research and writing of this thesis.

Besides my advisor, I would like to thank the rest of my thesis committee: Prof. C. Zhang and Prof. A. G. Straatman for their encouragement, and insightful comments.

The members of the laboratory for Complex Flow Systems have contributed immensely to my personal and professional time at Western. My sincere thanks also goes to my colleagues, Dr. Mohammad Zakir Hossain, Dr. Alireza Mohammadi, Dr. Hadi Vafadar Moradi, Sahab Zandi, Md Nazmus Sakib, Amirreza Seddighi, Yanbei Wang, and Sakib Shadman, for their friendship and encouragement. I am especially grateful for Dr. Hossain and I very much appreciated his enthusiasm, and knowledge.

I also want to thank my hard-working parents, Azar and Mehdi, who have devoted their lives to make the best possible life for my brothers and me and provided unconditional love and care. My elder brothers, Mehran and Iman have been my best friends all my life despite the age difference and I thank them for all their advices and supports. Special thanks to the lovely newest additions to my family, Zari and Behnoush, my sisters-in-law, I dedicate this thesis to them as I missed their weddings because of that.

The best outcome of these past two years is finding my best friend Dr. Maysam Shahedi. I thank his unfailing help and support all the time. I also thank all of my friends here in Canada and back in Iran. I wish for each one of them prosperity and success.

Finally I would like to mention that the support from The University of Western Ontario and the Natural Sciences and Engineering Research Council (NSERC) of Canada is gratefully acknowledged.

Table of Contents

List of Figures

List of Appendices

List of Abbreviations and Nomenclature

Abbreviations

FFT   Fast Fourier transform;

IBC   Immersed boundary conditions;

MAC   Marker and Cell;

RB   Rayleigh-Bénard;

RF   Relaxation factor;

RHS   Right-hand side;

SVD   Singular value decomposition;

VOF   Volume of Fluid.

Nomenclature used in Chapter 1

Pr Prandtl number.

Nomenclature used in Chapter 2

$*$ Superscript denoting dimensional quantities;

$*$ Superscript denoting complex conjugate;

A Mean pressure gradient;

A_c Mean pressure gradient correction;

$A_1, A_3, B_1, B_3, C_1, C_3, D_1, D_3$ Components of the rearranged coefficient matrices L_1, L_2, L_3;

$A_{1,0}, A_{3,0}, B_{1,0}, B_{3,0}, C_{1,0}, C_{3,0}, D_{1,0}, D_{3,0}$ Elements of the rearranged coefficient matrices $L_{1,0}, L_{3,0}$;

$A_U^{\langle n \rangle}, A_L^{\langle n \rangle}$	Coefficients of Fourier expansions describing the geometry;
c	Specific heat;
C_L, C_U	Corrugation amplitudes at the lower and upper plates;
D	Derivative with respect to the transverse direction;
$\widehat{DU}_k^{(m)}$	Coefficients of the Fourier expansions for the first derivative of the Chebyshev polynomials evaluated at the upper and lower plates;
$\left\| D\varphi^{(n)} \right\|_\omega$	Chebyshev norm of $D\varphi^{(n)}$;
Er_1, Er_2	Errors of the field quantities;
$\langle f, g \rangle$	Inner product of two functions;
$F_U^{\langle n \rangle}, F_L^{\langle n \rangle}$	Coefficients of Fourier expansions for $u_0(\hat{y}_U(x))$ and $u_0(\hat{y}_L(x))$;
g	Gravitational acceleration;
$\widehat{G\varphi}_k^{(n)}$	Chebyshev coefficients in the Chebyshev expansion representing $\varphi^{(n)}$;
$\widehat{G\emptyset}_k^{(n)}$	Chebyshev coefficients in the Chebyshev expansion representing $\emptyset^{(n)}$;
$\widehat{Guu}_k^{(n)}, \widehat{Guv}_k^{(n)}, \widehat{Gvv}_k^{(n)}, \widehat{Gu\theta}_k^{(n)}, \widehat{Gv\theta}_k^{(n)}$	Coefficients of the Chebyshev expansions of the modal functions in the Fourier expansions representing velocity and temperature products;
h	Half of the average channel height;
$H_{1,0}, H_{3,0}, K_{1,0}, K_{3,0}$	Elements of the rearranged coefficient matrices $L_{1,0}, L_{3,0}$;
i	Imaginary unit;
$I_k(\hat{y})$	Integral of kth Chebyshev polynomials of the first kind;
k	Thermal conductivity;
L,U	Subscript denoting the lower and upper plates;

l	Iteration number;
$\boldsymbol{L_1, L_2, L_3}$	Coefficient matrices defined by Eq.(2.5.1);
$\boldsymbol{L_{1,0}, L_{2,0}, L_{3,0}}$	Coefficient matrices defined by Eq.(2.8.1) and Eq.(2.8.8);
$\boldsymbol{L_{1,0}^+, L_{3,0}^+}$	Generalized inverse of $\boldsymbol{L_{1,0}, L_{3,0}}$;
$mean$	Subscript denoting mean value;
$\langle n \rangle$	Superscript denoting Fourier mode;
N_f	Number of Fourier modes in the Fourier expansions for the modification velocity components evaluated along the plates;
N_M	Number of Fourier modes used for discretization in the x-direction;
$N_{M,B}$	Number of Fourier modes used for boundary constraints in the over-determined formulation;
N_S	Number of Fourier modes used to describe the Chebyshev polynomials and their derivatives evaluated at the upper and lower plates;
$N_{VV}, N_{V\theta}$	Nonlinear terms;
N_T	Number of Chebyshev polynomials used for discretization of the modal functions in the $\hat{y}$-direction;
N_x	Number of grid points along the x-direction in $(x, \hat{y})$ plane;
p	Subscript denoting periodic value;
p	Total pressure;
p_0	Pressure associated with the Poiseuille flow;
$p^{(n)}$	Modal functions of Fourier expansions for the periodic part of the pressure modification;
Pr	Prandtl number;
Q	Net flow rate through the conduit;

Q_0	Flow rate associated with the Poiseuille flow;
$\boldsymbol{R_1}, \boldsymbol{R_2}$	Right-hand side vectors defined by Eq.(2.5.2);
$\boldsymbol{R_{1,0}}, \boldsymbol{R_{2,0}}$	Right-hand side vectors defined by Eq.(2.8.1) and Eq.(2.8.8);
$Ra_{p,L}, Ra_{p,U}$	Rayleigh numbers associated with intensities of the lower and upper heating;
Ra_{uni}	Rayleigh number associated with intensity of the uniform heating;
Re	Flow Reynolds number;
T_k	kth Chebyshev polynomials of the first kind;
T_U, T_L	Temperatures of the upper and lower plates;
$\boldsymbol{T_1}$	Vectors of unknowns $\widehat{G\emptyset}_k^{(n)}$ for $n \in \langle -N_M, N_M \rangle$ and $k \in \langle 2, N_T - 1 \rangle$;
$\boldsymbol{T_2}$	Vectors of unknowns $\widehat{G\emptyset}_k^{(n)}$ for $n \in \langle -N_M, N_M \rangle$ and $k \in \langle 0,1 \rangle$;
$\boldsymbol{U}, \boldsymbol{Z}, \boldsymbol{W}, \boldsymbol{Z_1}$	Matrices used in the SVD method;
u, v	Velocity components in the x- and y- directions;
u_0, v_0	Velocity components of the Poiseuille flow in the x- and y-directions;
U_{max}	Maximum of the streamwise velocity component of the Poiseuille flow;
$\|u_{Le}\|_\infty$	L^∞ norms of the u-velocity at the lower plate;
$U_{Le}^{(n)}, \theta_{Le}^{(n)}$	The Fourier spectra of $u_{Le}(x)$ and $\theta_{Le}(x)$;
U_v	Velocity scale;
$\widehat{uu}, \widehat{uv}, \widehat{vv}, \widehat{u\theta}, \widehat{v\theta}$	Velocity and temperature products in the physical space;
$\widehat{uu}^{(n)}, \widehat{uv}^{(n)}, \widehat{vv}^{(n)}, \widehat{u\theta}^{(n)}, \widehat{v\theta}^{(n)}$	Modal functions of the velocity and temperature products $\widehat{uu}, \widehat{uv}, \widehat{vv}, \widehat{u\theta}, \widehat{v\theta}$;

V, T	Vectors of unknowns defined by Eq.(2.5.2);
V_1	Vectors of unknowns $\widehat{G\varphi}_k^{(n)}$ for $n \in \langle -N_M, N_M \rangle$ and $k \in \langle 4, N_T - 1 \rangle$;
V_2	Vectors of unknowns $\widehat{G\varphi}_k^{(n)}$ for $n \in \langle -N_M, N_M \rangle$ and $k \in \langle 0,3 \rangle$;
$\|V\|^2$	The L^2 norm of vector V;
$\widehat{WU}_k^{(m)}$	Coefficients of Fourier expansions for the Chebyshev polynomials evaluated at the upper and lower plates;
(x, y)	physical coordinate system;
$(x, \hat{y})$	Computational coordinate system;
$\|X_{ref} - X\|^2$	L^2 norm of the difference between the reference solution and the solution obtained with the prescribed N_T and N_M;
$\|X_{ref}\|^2$	L^2 norm of the reference solution;
y_b, y_t	Amplitudes of the corrugation at the lower and upper plates;
y_U, y_L	Shapes of the upper and lower plates in the physical coordinate system;
$\hat{y}_U, \hat{y}_L$	Shapes of the upper and the lower plates in the computational coordinate system;
α	Corrugation wave number;
Γ	Thermal expansion coefficient;
Γ	Constant associated with the coordinate transformation for the IBC method;
θ	Relative temperature;
$\|\theta_{Le}\|_\infty$	L^∞ norms of temperature at the lower plate;
κ	Thermal diffusivity;
λ	Wavelength of the corrugation and heating;

μ	Dynamic viscosity;
ν	Kinematic viscosity;
ρ	Density;
$\emptyset^{(n)}$	Modal functions in the Fourier expansion representing the temperature;
$\left\lVert \emptyset^{(n)} \right\rVert_\omega$	Chebyshev norm of $\emptyset^{(n)}$;
$\varphi^{(n)}$	Modal functions in the Fourier expansion representing the stream function;
ψ	Stream function;
$\Omega_{T,L}, \Omega_{T,U}$	Phase shifts of the heating patterns with respect to the corrugation patterns at the lower and upper plates;
ω	Weight function.

Nomenclature used in Chapter 3

C	Free constant in the pressure field;
$c_1, \dots, c_6$	Constants in the solution for $\widehat{v_1}$;
$Dif_1, Dif_{1,L}$	Pressure forces contributing to either the flattening or growing of the corrugation at the lower plate;
$Dif_{1,U}$	Pressure forces contributing to either the flattening or growing of the corrugation at the upper plate;
Dif_2	Difference between $Nu_{loc,L}$ at $x = 0$ and at $x = \lambda/2$;
$\lVert Er \rVert_{max}$	Difference between the complete and asymptotic solutions;
$F_{x,L}, F_{x,U}$	Forces acting on the lower and upper plates;
$F_{xv,L}, F_{xp,L}$	Viscous and pressure components of $F_{x,L}$;
$F_{xv,U}, F_{xp,U}$	Viscous and pressure components of $F_{x,U}$;

$G, F_1, \dots, F_9$	Coefficients given in Appendices B and D;
$H_{t,L}, H_{t,U}$	The total stretching forces per half of the corrugation wavelength;
$H_{y,peak}, H_{y,trough}$	y-components of forces acting on the upper and the lower parts of the corrugation;
$k_1, \dots, k_{14}$	Coefficients given in Appendix B;
$L_u, LS_{u,n}, LC_{u,n},$ $L_v, LS_{v,n}, LC_{v,n},$ $L_p, LS_{p,n}, LC_{p,n},$ $L_\theta, LS_{\theta,n}, LC_{\theta,n},$ $L_{vL}, LS_{vL,n}, LC_{vL,n},$ $L_{vU}, LS_{vU,n}, LC_{vU,n},$ $L_{pL}, LS_{pL,n}, LC_{pL,n},$ $L_{pU}, LS_{pU,n}, LC_{pU,n},$ $L_1, \dots, L_6$	Coefficients given in Appendix D;
M	Moment due to forces acting on the plates in the x-direction;
$n_{x,L}, n_{y,L}$	Outward normal unit vectors at the lower plate;
N_L, N_U	Components of the normal vectors at the lower and upper plates;
Nu_{loc}	The local Nusselt number;
Nu_{av}	The mean Nusselt number;
$Nu_{cond,loc,L}, Nu_{cond,av}$	Local and mean conductive Nusselt numbers;
$p_{-1}, u_0, v_0, \theta_0, \theta_{c0}$	The leading-order terms in the asymptotic expansions for pressure, velocity and temperature components in the limit of $\alpha \to 0$;
$p_0, u_1, v_1, \theta_1, \theta_{c1}$	Terms of $O(\alpha^1)$ in the asymptotic expansions for pressure, velocity and temperature components in the limit of $\alpha \to 0$;
$p_1, u_2, v_2, \theta_2, \theta_{c2}$	Terms of $O(\alpha^2)$ in the asymptotic expansions for pressure, velocity and temperature components in the limit of $\alpha \to 0$;
p_0, u_0, v_0, θ_0	The leading-order terms in the asymptotic expansions for pressure, velocity and temperature components in the limit of

$y_b \rightarrow 0$;

p_1, u_1, v_1, θ_1	Terms of $O(y_b{}^1)$ in asymptotic expansions for pressure, velocity and temperature components in the limit of $y_b \rightarrow 0$;
$\vec{q}_L, \vec{q}_U$	Temperature gradients at the lower and upper plates;
$q_{x,L}, q_{y,L}$	Components of $\vec{q}_L$;
R	The ratio of the Nusselt numbers for slots with corrugations placed at both plates and at a single plate;
Ra	Intensity of the uniform heating;
S	Amplitude of corrugations at the lower and upper plates;
$\widehat{v_1}, \widehat{\theta_1}, \widehat{P_1}$	Modal functions for v_1, θ_1, P_1;
$\varepsilon_1, \dots, \varepsilon_6$	Roots of the characteristic polynomial defined in Eq.(C.13);
(ξ, η)	Horizontal and vertical coordinates in the transformed coordinate system;
η_x, η_{xx}	First and second derivative of η with respect to x;
η_y	Derivative of η with respect to y;
$\theta_{cond}, \theta_{conv}$	Conduction and convection components of temperature fields;
θ_s	Rayleigh number associated with the relative temperature of the lower plate;
$\vec{\sigma}_L$	Stress vector acting on the lower plate;
$\sigma_{x,L}, \sigma_{y,L}, \sigma_{x,U}, \sigma_{y,U}$	Distribution of the x-and y-components of the local forces per unit length of the channel acting on the plates;
$\sigma_{xv,L}, \sigma_{xp,L}, \sigma_{xv,U}, \sigma_{xp,U}$	Viscous and pressure components of $\sigma_{x,L}, \sigma_{x,U}$;
$\sigma_{yv,L}, \sigma_{yp,L}, \sigma_{yv,U}, \sigma_{yp,U}$	Viscous and pressure components of $\sigma_{y,L}, \sigma_{y,U}$;
$\sigma_{n,L}, \sigma_{t,L}, \sigma_{n,U}, \sigma_{t,U}$	Distribution of the normal and tangential forces per unit length of the channel acting on the plates;

$\sigma_{nv,L}, \sigma_{np,L}, \sigma_{nv,U}, \sigma_{np,U}$ Viscous and pressure components of $\sigma_{n,L}, \sigma_{n,U}$;

$\sigma_{tv,L}, \sigma_{tp,L}, \sigma_{tv,U}, \sigma_{tp,U}$ Viscous and pressure components of $\sigma_{t,L}, \sigma_{t,U}$;

$\tau_{xx}, \tau_{xy}, \tau_{yy}$ Components of the shear tensor;

$\phi_n(\xi, \eta)$ Complete solutions for u, v, θ, p;

$\phi_a(\xi, \eta)$ Asymptotic solutions for u, v, θ, p.

Chapter 1

Introduction

1.1. Objectives

The objective of this thesis is to analyze convection inside a heated corrugated slot. The effects of corrugations on the heat transfer, the intensity of fluid movement and the forces created at the bounding plates are of interest. The heat transfer characteristics are sought for engineering applications. The convection-generated forces are of interest in systems where erosion is possible and in systems involving membranes which may be either stretched, or deformed or both.

1.2. Motivation

Boundary irregularities are found in many physical systems, e.g. heat transfer devices, biological membranes, the surface of the earth, etc. Understanding the effect of such irregularities is of vital interest in many applications including enhancing performance of heat exchangers, in designing microfluidic components, and in developing cell analyzers, e.g. counting and measuring blood cells, to name just a few. Analysis of the effects of corrugations on convection helps in understanding the mechanism of natural phenomena such as circulation in urban and rural environments, convection above ocean bottoms, weather prediction, surface erosion and many other cases.

Boundary irregularities include geometric irregularities as well as temperature irregularities. Their spatial distribution and shape may have many forms but, regardless, one is interested in providing a general assessment of their effect on convection. The existing analysis represents case studies as they are focused either on specific geometries or on specific temperature distributions (Choi & Orchard 1997; Stalio & Nobile 2003; Herwig et al. 2008; Gamrat et al. 2008). It is rather difficult to extrapolate such results to arbitrary irregularities and this prevents their use for improvement of efficiency of

convection processes and/or control of such processes through the proper design of such irregularities. Geometric irregularities result in irregular flow domains and systematic analysis of their effects requires development of algorithms capable of handling variable geometries with a minimum of manual effort. The first objective of this study is therefore development of the required algorithms.

1.3. Methodology development

Analysis of effects of corrugations on the convection processes must address the issue of modelling of corrugation geometry. As there are a countless number of possible corrugation shapes, it appears that a general solution is not possible. Typical approaches rely on the selection of the geometry of interest and construction of boundary fitted coordinates followed by a solution of the field equations (Choi 1997; Stalio & Nobile 2003; Herwig et al. 2008; Gamratet al. 2008). These methods are usually based on the finite-volume, finite-element, or finite-differences and have low-order spatial accuracy. Increase of accuracy necessitates use of finer grids which is computationally expensive. These methods are impractical for geometry optimization and for systematic investigation of a large number of corrugation geometries.

Convective motion is highly unstable and their analysis requires the determination of the onset condition and form of secondary motions. The prediction of the onset of secondary states requires a highly accurate solution of the primary state, but very few high-accuracy grid generation methods are available, e.g. conformal mapping based on the Schwartz-Christoffel transformation whose parameters can be determined with near spectral accuracy (Floryan 1986; Floryan & Zemach 1987; 1993). One alternative is offered by the domain transformation method, which relies on the analytical mapping of the irregular physical domain to a rectangular computational domain. However, such mappings are available only for a limited class of geometries (Hamed & Floryan 1998; Cabal et al. 2001). The other alternative involves the immersed (or fictitious) boundaries concept, whose origin can be traced to the analysis of moving boundary problems and the development of interface tracking methods (Floryan & Rasmussen, 1989). In this class of

problems, the grid is fixed while the solution domain moves through this grid eliminating the high computational cost of the adjustment of boundary fitted grids. The available algorithms rely either on surface tracking, or on volume tracking (Floryan & Rasmussen, 1989)

1.3.1. Surface tracking

In this method, a discrete set of points is used to mark the location of the interface which is represented using interpolated curves. At each time-step, the location of the marker points and the sequence in which the curves are connecting them are saved. In the case of two-dimensional surface tracking, the points are saved either as a sequence of heights above the reference line (See Fig.1.1A) or the points follow a parametric representation (See Fig.1.1B). This method provides precise information about the interface location but is expensive due to the need to maintain a separate grid system (marker points) defining interface location.

(A)   (B)
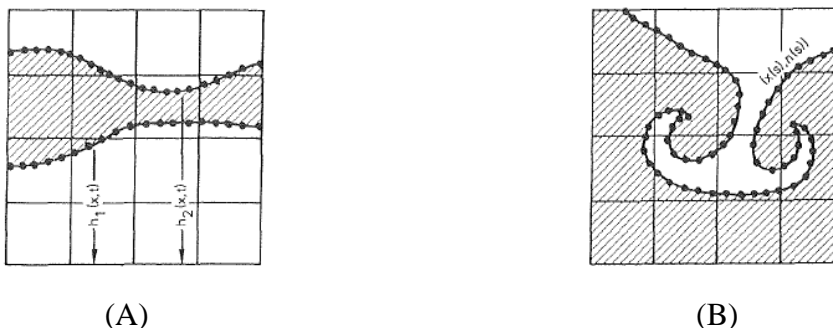
Figure 1.1: Surface tracking of an interface. The interface is determined by (A) a sequence of heights above a reference line or (B) a series of points (Hyman 1984).

1.3.2. Volume tracking

In this method, the location of the interface is reconstructed when needed rather than being explicitly tracked. There are several versions of volume tracking.

Marker-And-Cell method (Harlow & Welch 1966) represents the simplest form of volume tracking (Floryan & Rasmussen 1989). This method decomposes the computational domain into cells with velocities defined at the faces of the cells and

scalars defined at the centres of the cells. Rectangular mesh grids are used to cover the solution domain. The interface tracking is based on the idea of the so-called fraction function. If the fraction is 1, the cell is completely occupied by the fluid and if the fraction is 0 the fluid does not occupy the cell. There is no interface present if the fraction is 1 or 0. An interface is to be constructed only if the fraction is between 0 and 1. The method does not give any details about the exact location, orientation, and curvature of the interface (see Figs.1.2A and 1.2B).

Volume-Of-Fluid method developed by Hirt & Nichols (1981) reconstructs the interface in the relevant cells by approximating it with a straight line (see Fig 1.2.C). This method provides approximation for the location and slope of the interface (see Hyman 1984 for details).

(A)   (B)   (C)
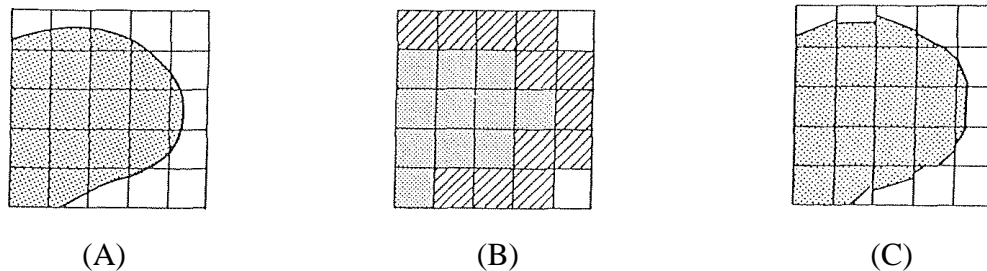
Figure 1.2: Reconstruction of interface using volume tracking procedures: (A) the actual form of the interface; (B) reconstruction based on a MAC procedure (the interface is somewhere inside the shaded area); (C) reconstruction based on a VOF procedure (Hirt & Nichols 1981).

Improvements in the surface tracking and volume tracking have lead to the front tracking (Glimm et al. 1998) and level set (Sethian 1999; Sethian & Smereka 2003) methods, respectively. The standard form of these algorithms relies on spatial discretization with a low-order accuracy consistent with the diffused boundary locations resulting from the tracking procedures.

1.3.3. Immersed Boundary Method

The immersed boundaries concept has re-emerged recently and has undergone a rapid development (Peskin 2002; Mittal & Iaccarino 2005). This method is suitable for simulations of problems involving the interaction of fluids and immersed elastic

structures. It uses finite-difference discretization, Eulerian grid points for the fluid variables and Lagrangian variables for the immersed boundary (see Fig.1.3). These two types of variables are linked by a smooth version of the Dirac delta function.

<div align="center">(A)   (B)</div>
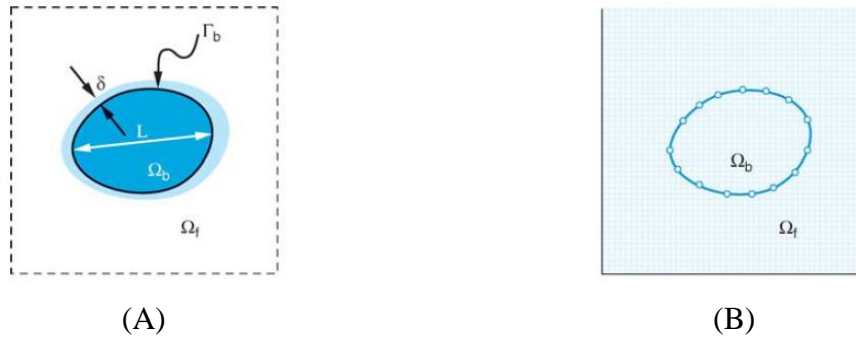
Figure 1.3: A general body immersed into a fluid (Fig1.3.A). The body and fluid ocupy the volume Ω_b, and Ω_f, respectively with boundary Γ_b. L is the charactristic length of the body and δ is the thickness of the boundary layer developed over the body. Figure 1.3.B shows the schematic body immersed in a Cartesian grid discrtizing the governing equations (Mittal & Iaccarino 2005).

The common limitation is the spatial accuracy, as most of these methods are based on either low-order finite-difference, finite-volume or finite-element techniques (Kim, 2001; Deng et al. 2006; Taira & Colonius 2007). The second, less known limitation is the use of the local fictitious forces required to enforce the no-slip and no-penetration conditions at the boundaries. These forces locally affect the flow physics and this may lead to incorrect estimates of derivatives of flow quantities, i.e. misrepresentation of the local wall shear. This problem is likely to be more pronounced in the case of methods with high spatial accuracy.

1.3.4. Immersed Boundary Conditions method

The spectrally-accurate version of the immersed boundary concept, referred to as the Immersed Boundary Conditions (IBC) method, was proposed in 1999 (Szumbarski & Floryan 1999) for the solution of the Navier-Stokes equations and is still the only method which guarantees spectral accuracy of the complete solution rather than just the spectral discretization of the field equations. In this method, the flow domain is immersed into a fixed rectangular computational domain, the solution is represented in terms of global basis functions and boundary conditions are expressed as boundary constraints resulting

in a gridless system (see Fig1.4). This method has been extended to two- and three-dimensional conduction problems (Husain & Floryan 2007; Del Rey Fernandez et al. 2010) as well as conduction problems with moving boundaries (Husain & Floryan 2008). This method will be used as the starting point to develop an algorithm suitable for the analysis of convection in corrugated slots.
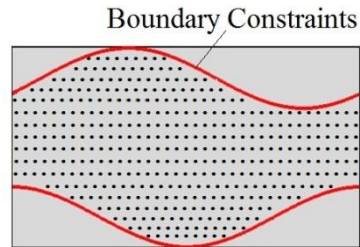
Figure 1.4: Sketch of flow domain (dotted-area) immersed into a gridless rectangular computational domain (gray-area); boundary conditions are replaced by boundary constraints.

1.4. Natural Convection

Thermal convection is one of the most common forms of fluid motions. It occurs in many application areas such as heat exchangers, biological systems, weather predictions, and convection in the atmosphere, oceans and within the earth mantle, among many others. Understanding its characteristics is therefore of the utmost importance.

The character of convection depends on the geometry of the flow system and on the externally imposed thermal conditions. Because of a large range of variability of such conditions, the analysis of fundamental aspects of convection have been focused on simple reference cases. One of the best-known reference problems is the natural convection in a horizontal slot subject to a spatially homogeneous heating applied at the lower plate. This problem is referred to as the Rayleigh-Bénard (RB) convection (Bénard 1900; Rayleigh 1916) and has been studied for many decades using both theoretical and experimental approaches (Bodenschatz et al. 2000). Convection results from the transition from a conductive state when the critical conditions are exceeded (Chilla & Schumacher 2012) and it changes the character of the heat flow in qualitative terms. These critical conditions are expressed in terms of the critical Rayleigh number Ra_{cr}

with secondary flow occurring for Ra> Ra_{cr}. A large enough heating intensity leads to turbulent RB convection (Ahlers et al. 2009; Lohse & Xia 2010).

The convection onset conditions can be affected by heating non-uniformities (Freund et al 2012) as well as non-uniformities in the plate geometry (McCoy et al. 2008; Seiden et al 2008; Weiss et al. 2012). Results dealing with the effects of geometry modulation on the RB convection are very limited but demonstrate that the non-uniformities do play a role; the detailed analyses and identification of mechanisms activated by them are yet to be carried out. Two-dimensional convection rolls have been observed for subcritical conditions ($Ra << Ra_{cr}$) in the case of the lower plate being augmented with thin stripes. Amplitude of these rolls grew with Ra until they were destabilized with mechanisms which depended on the ratio of the wave number of the imposed modulation and the critical wave number of the RB convection producing a variety of three-dimensional patterns (McCoy et al. 2008; Seiden et al. 2008). Experiments show that the combined effect of strips parallel to the flow and gravity-induced shear flow leads to the creation of longitudinal and transverse rolls depending on the angle of the corrugation and gravity component (Weiss et al. 2012).

Temperature non-uniformities affect the onset conditions for RB convection (Freund et al. 2012) as well as create their own convection which occurs regardless of the heating intensity (Hossain & Floryan 2013a; 2013b; 2014; 2015a; 2015b). As there are an uncountable number of heating non-uniformities, the recent studies have been focused on the simplest pattern consisting of sinusoidal heating with an arbitrary wavelength (Hossain & Floryan 2013b) and has led to the concept of structured convection. There are numerous examples of such convection in very low wind speed conditions, e.g. circulation in urban environment as local heating rates are determined by the dissimilar thermal properties of roofs, streets and parks, and circulation in rural environments where variations of the heating rates of forests, fields, and lakes drive the local circulation Convection within the Earth mantle is affected by the insulating effect of continents and represents a spatially structured convection with heating from above (Lenardic et al. 2005). A system of fractures, leads and polynyas in sea ice leads to convection in both the

ocean and atmosphere (Marcq & Weiss 2012). Use of mixed insulating and conducting boundary conditions leads to a spatially patterned convection (Ripesi et al. 2014). Human activity resulting in the heat island effect (Rizwam et al. 2008) can be analyzed from the heating pattern point of view. Dynamics of a systems of localized fires and prediction of their propagation represent another challenging problem (Finney et al. 2012) similarly as the thermal patterning in micro-fluidic devices (Beltrame et al. 2011; Krishnan et al. 2002). Applying the same heating either from above or from below results in similar motions (Hossain & Floryan 2014). The flow topology is locked in with the heating pattern but only for small convection intensities. Higher intensities result in the transition to secondary states which might have different patterns (Hossain & Floryan 2013a).

Heating non-uniformities represent a wider class of problems which has been studied on a case by case basis. The non-uniformities create horizontal and vertical temperature gradients which result in the horizontal density variations which create motions frequently referred to as horizontal convection. Maxworthy (1997) has reviewed the numerical and experimental analysis focused on convection in regions with either open or partially-open lateral boundaries. Three typical geometries have been considered in this review, i.e. convection in a channel, convection from a patch or strip into stratified and/or rotating surroundings and convection into a rotating coastal environment. Siggers et al. (2004) have showed numerically that the horizontal convection can be unsteady and turbulent, capable of maintaining overturning circulation within a layer heated and cooled differentially at its surface with a general temperature distribution imposed at the top of the layer and a variety of thermal boundary conditions at the base of the layer. Hughes & Griffiths (2008) used horizontal convection as an idealized model of the ocean overturning circulation where the non-uniformities profiles of heating were imposed at a horizontal boundary. The horizontal convection in oceans was studied by Winters & Young (2009) from the energy balance point of view resulting in the conclusion that the buoyancy force alone is insufficient to account for the observed levels of kinetic energy in oceans, and additional energy sources, e. g. wind, are needed.

There are numerous case studies focused on the applied aspects of convection and involving specialized geometries. Nicolas (2000) reviewed results dealing with the Poiseuille-Rayleigh-Bénard flows in rectangular smooth ducts. Bergles (2001) showed that for single phase flows in tubes, up to a 400% increase in the nominal heat transfer coefficient can be achieved by adjusting surface topography. Siddique et al. (2010) reviewed different heat transfer enhancing techniques based on (a) use of extended surfaces including fins and micro-fins, (b) use of porous media, (c) use of suspensions of large particles, (d) use of suspensions of small particle (nanofluids), (e) use of phase-change devices, (f) use of flexible seals, (g) use of flexible complex seals, (h) use of vortex generators, (i) use of protrusions, and (j) use of composite materials with ultra-high thermal conductivity. Dewan et al. (2004) carried out a review of the passive heat transfer augmentation techniques based on the use of twisted tapes and wire coils; these devices are of interest due to their low cost. Jacobi & shah (1998) discussed the enhancement of heat transfer in a single fin heat exchanger. Ligrani (2003) suggested that all these techniques can either create secondary flows and/or can increase the turbulence level resulting in an increase of fluid mixing.

There is a gap in the literature between the fundamental and applied convection studies, and its elimination would yield practically important information about convection in more complex geometries. One of the areas where the fundamental information is missing is the effect of surface roughness/corrugations on the natural and mixed convection, and on the onset of secondary states in buoyancy driven motions. This issue is prominent in micro-conduits where the roughness size cannot be reduced to a negligible level using currently available manufacturing techniques. Sobhan & Garimella (2001) has reviewed different studies on the flow and heat transfer in micro-channels with surface roughness. They suggested that there is a need for additional systematic studies to examine each parameter influencing heat transport in such channels. Xia et al. (2011) have studied the fluid flow and heat transfer mechanism in micro-channels with aligned fan-shaped re-entrant cavities and identified the increase of the surface area, the redeveloping boundary layers, and the jet and throttling effects as responsible for the increased heat transfer which is accompanied by an increased pressure drop.

The above discussion shows that there is a need for a systematic study of the effects of geometric non-uniformities on convection and for identification of the mechanisms responsible for heat transfer intensification. The second part of this thesis is focused on the analysis of convection in corrugated slots and fills in some of the gaps in the understanding of convection in such systems.

1.4. Overview of the work presented in this thesis

Analysis of the basic features of convection requires the selection of a convenient model problem. The model configuration has the form of a horizontal slot extending to $\pm \infty$ in the horizontal direction with gravity acting in the vertical direction, as shown in Fig.1.5. The geometric non-uniformities have the form of sinusoidal corrugations which represent the leading term of Fourier expansions describing corrugations of arbitrary form. It is expected that corrugations of such form capture most of the physics associated with the corrugations of more complex forms. The plates are assumed to be isothermal, with the lower plate having a higher temperature. The fluid movement is described by a system of equations consisting of the continuity, Navier-Stokes and energy equations. Properties of the fluid are approximated using the so-called Boussinesq approximation. It is assumed that in the case of natural convection there is no mean pressure gradient in the horizontal direction. The heat transfer from the plates and the forces acting on the plates are determined from the solution of the field equations.
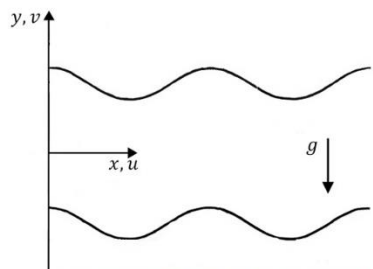
Figure 1.5: Schematic diagram of the flow system. The corrugated slot is subject to a uniform heating from below.

Chapter 2 provides the description of a grid-less, spectrally-accurate algorithm based on the IBC concept suitable for analysis of convection in corrugated conduits. The

algorithm is general in the sense that it can simulate the natural, mixed and forced convections. Sinusoidal grooves and sinusoidal heating non-uniformities have been selected to represent geometric and temperature non-uniformities. Discretization of the field equations, the boundary conditions, and the flow rate constraint are presented. The linear solver which takes advantage of the structure of coefficient matrix is also described. The potential gains associated with the overdetermined formulation of the numerical problem are discussed.

Chapter 3 is devoted to the analysis of natural convection in a slot formed by two horizontal corrugated plates using the algorithm described in Chapter 2. The goal of this Chapter is to develop an understanding of the natural convection arising in response to geometric non-uniformities. The analysis is focused on the reference case involving sinusoidal corrugations whose geometry is characterized in terms of the corrugation wave number and the corrugation amplitude. Placement of corrugations on both plates adds the second amplitude as well as the phase difference describing the relative position of both corrugations systems. The heating intensity is expressed in terms of the Rayleigh number based on the temperature difference between both plates as the temperature scale and the half of the mean slot opening as the length scale. The Chapter ends with the assessment of the effects of the Prandtl number.

Chapter 2

Spectrally Accurate Algorithm

2.1. Introduction

This Chapter is focused on the extension of the Immersed Boundary Condition (IBC) algorithm to non-isothermal conditions. The roughness can have any shape. Since the main goal of the analysis is to develop techniques for the analysis of roughness effects, the reduced geometry model is invoked in which the geometry is projected onto a convenient reference functional space and elements of this space relevant for hydrodynamics are sought (Floryan 2007). This leads to the analysis of sinusoidal grooves which represent the dominant terms in the geometry projection onto Fourier space. It has been demonstrated that this approach provides a general answer to the issue of roughness effects with accuracy sufficient for most applications. Section 2.2 provides a description of the model problems used to illustrate the algorithm. Section 2.3 discusses the discretization, with Section 2.3.1 focused on the discretization of the field equations, Section 2.3.2 describing the discretization of the boundary conditions and Section 2.3.3 discussing the discretization of the flow rate constraint. Section 2.4 describes the solution process, Section 2.5 is focused on the linear solvers and Section 2.6 discusses the evaluation of the pressure field. Section 2.7 discusses the performance of the algorithm while Section 2.8 describes the gains associated with the overdetermined formulation. Section 2.9 provides a short summary of the main conclusions.

2.2. Problem Formulation

Consider channel formed by two horizontal corrugated plates (see Fig.2.1) whose geometries have the form

$$y_L^*(x^*) = -h^* + C_L^* \cos(\alpha^* x^*),$$ (2.2.1a)

$$y_U^*(x^*) = h^* + C_U^* \cos(\alpha^* x^* + \Omega_C^*),$$ (2.2.1b)

where the subscripts L and U refer to the lower and upper plate, respectively, C_L^* and C_U^* are the amplitudes of the corrugations at the lower and upper plates, respectively, Ω_C^* stands for the phase shift between them, α^* is their wave number and stars denote dimensional quantities. The channel is periodic with a wavelength $\lambda^* = 2\pi/\alpha^*$ and extends to $\pm\infty$ in the *x*-direction with the mean distance between the plates $2h^*$. The gravitational acceleration g^* is acting in the negative *y*-direction. The steady, incompressible flow of a Newtonian fluid is driven in the positive *x*-direction by an externally imposed pressure gradient. The fluid has thermal conductivity k^*, specific heat c^*, thermal diffusivity $\kappa^* = k^*/\rho^* c^*$, kinematic viscosity ν^*, dynamic viscosity μ^*, thermal expansion coefficient Γ^* and variations of the density ρ^* follow the Boussinesq approximation. All material properties are evaluated at the reference temperature.

$$\theta_U(x) = 0.5\, Ra_{p,U}\cos(\alpha x + \Omega_C + \Omega_{TU})$$
$$y_U(x) = 1 + y_t \cos(\alpha x + \Omega_C)$$
$$y_L(x) = -1 + y_b \cos(\alpha x)$$
$$\theta_L(x) = Ra_{uni} + 0.5\, Ra_{p,L}\cos(\alpha x + \Omega_{TL})$$
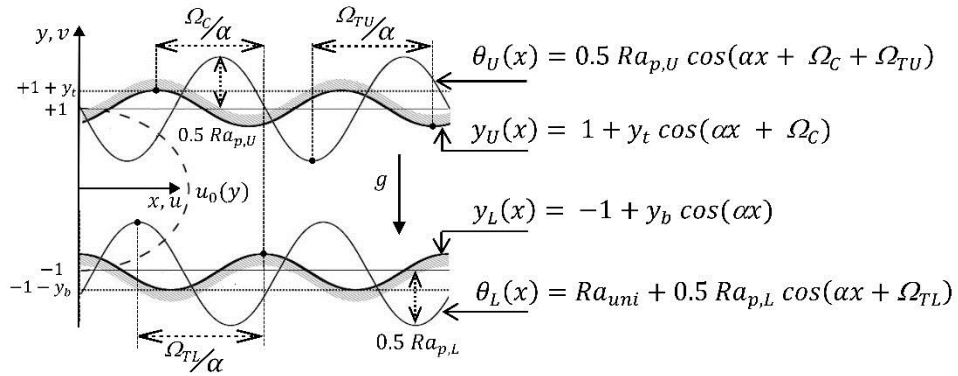
Figure 2.1: Schematic diagram of the flow system**.**

The lower and upper plates are subject to the spatially periodic heating resulting in the temperatures of the lower (T_L^*) and the upper (T_U^*) plates of the form

$$T_L^*(x^*) = T_{mean,L}^* + 0.5\, T_{p,L}^*\cos(\alpha^* x^* + \Omega_{TL}^*), \tag{2.2.2a}$$

$$T_U^*(x^*) = T_{mean,U}^* + 0.5\, T_{p,U}^*\cos(\alpha^* x^* + \Omega_C^* + \Omega_{TU}^*), \tag{2.2.2b}$$

where the subscripts *"mean"* and *"p"* refer to the mean and periodic parts, respectively, $T_{p,L}^*$ and $T_{p,U}^*$ are the peak-to-peak amplitudes of the periodic heating components at the lower and upper plates, respectively, and Ω_{TL}^* and Ω_{TU}^* are the phase shifts of the heating

patterns with respect to the corrugation patterns at the lower and upper plates, respectively.

We select the mean temperature of the upper plate as the reference temperature and define the relative temperature as $\theta^* = T^* - T^*_{U,mean}$. The plates' relative temperatures take the form of

$$\theta^*_L(x) = \theta^*_{uni} + 0.5\,\theta^*_{p,L}\,cos(\alpha^*x^* + \Omega^*_{TL}), \tag{2.2.3a}$$

$$\theta^*_U(x) = 0.5\,\theta^*_{p,U}cos(\alpha^*x^* + \Omega^*_C + \Omega^*_{TU}), \tag{2.2.3b}$$

where $\theta^*_{uni} = T^*_{mean,L} - T^*_{mean,U}$, $\theta^*_{p,U} = T^*_{p,U}$, $\theta^*_{p,L} = T^*_{p,L}$. Use of half of the mean channel opening h^* as the length scale and $\kappa^*\nu^*/(g^*\Gamma^*h^{*3})$ as the temperature scale result in the following dimensionless expressions for the geometry and temperatures

$$y_L(x) = -1 + y_b\,cos(\alpha x), \tag{2.2.4a}$$

$$y_U(x) = 1 + y_t\,cos(\alpha x + \Omega_C), \tag{2.2.4b}$$

$$\theta_L(x) = Ra_{uni} + 0.5\,Ra_{p,L}\,cos(\alpha x + \Omega_{TL}), \tag{2.5a}$$

$$\theta_U(x) = 0.5\,Ra_{p,U}\,cos(\alpha x + \Omega_C + \Omega_{TU}), \tag{2.5b}$$

where y_b and y_t are the amplitudes of the corrugation at the lower and upper plates, respectively, $Ra_{uni} = g^*\Gamma^*h^{*3}T^*_{uni}/(\kappa^*\nu^*)$ is the uniform Rayleigh number measuring the intensity of the uniform heating, $Ra_{p,L} = g^*\Gamma^*h^{*3}T^*_{p,L}/(\kappa^*\nu^*)$ is the lower periodic Rayleigh number measuring the intensity of the lower heating and $Ra_{p,U} = g^*\Gamma^*h^{*3}T^*_{p,U}/(\kappa^*\nu^*)$ is the upper periodic Rayleigh number measuring the intensity of the upper heating.

The field equations take the following form

$$\frac{\partial u}{\partial x} + \frac{\partial v}{\partial y} = 0, \tag{2.2.6a}$$

$$u\frac{\partial u}{\partial x} + v\frac{\partial u}{\partial y} = -\frac{\partial p}{\partial x} + \nabla^2 u, \tag{2.2.6b}$$

$$u\frac{\partial v}{\partial x} + v\frac{\partial v}{\partial y} = -\frac{\partial p}{\partial y} + \nabla^2 v + Pr^{-1}\theta, \tag{2.2.6c}$$

$$u\frac{\partial \theta}{\partial x} + v\frac{\partial \theta}{\partial y} = Pr^{-1}\nabla^2\theta, \tag{2.2.6d}$$

where (u, v) are the velocity components in the (x, y) directions, respectively, scaled with $U_v^* = v^*/h^*$ as the velocity scale, p stands for the pressure scaled with $\rho^* U_v^{*2}$ as the pressure scale and $Pr = v^*/\kappa^*$ is the Prandtl number. These equations are subject to the following boundary conditions

$$u(y_L(x)) = u(y_U(x)) = 0, \tag{2.2.7a}$$
$$v(y_L(x)) = v(y_U(x)) = 0, \tag{2.2.7b}$$
$$\theta(y_L(x)) = \theta_L(x), \tag{2.2.7c}$$
$$\theta(y_U(x)) = \theta_U(x). \tag{2.2.7d}$$

The problem formulation requires specification of one closing condition. We shall use the fixed flow rate constraint, i.e. we shall require that the flow rate through the heated corrugated channel must be the same as the flow rate through the smooth isothermal channel. The reference flow in the latter channel has the form of

$$v_0(x,y) = [u_0(y), 0] = [1 - y^2, 0], \quad p_0(x,y) = -2x/Re, \quad Q_0 = 4/3, \tag{2.2.8}$$

where the subscript 0 identifies the reference flow quantities, velocity has been scaled with its maximum U_{max}^* as the velocity scale, Q_0 stands for the flow rate scaled with the same velocity scale, the pressure has been scaled using $\rho^* U_{max}^{*2}$ and $Re = U_{max}^* h^*/v^* = U_{max}^*/U_v^*$ is the Reynolds number. The flow rate constraint takes the form of

$$Q(x)|_{mean} = \left(\int_{y_L(x)}^{y_U(x)} u(y)\, dy\right)\Big|_{mean} = \frac{4}{3}Re, \tag{2.2.9}$$

where Q is the flow rate carried by the stream and scaled with U_v^* as the velocity scale.

2.3. Discretization

Introduce the stream function ψ defined in the usual manner, i.e.

$$u = \frac{\partial \psi}{\partial y}, \quad v = -\frac{\partial \psi}{\partial x}, \tag{2.3.1}$$

and eliminate pressure from the field equations to arrive at

$$\nabla^4 \psi - Pr^{-1} \frac{\partial \theta}{\partial x} = N_{VV}, \tag{2.3.2a}$$

$$\nabla^2 \theta = Pr\, N_{V\theta}, \tag{2.3.2b}$$

$$Q(x)|_{mean} = \psi(y_U(x))|_{mean} - \psi(y_L(x))|_{mean} = \frac{4}{3} Re, \tag{2.3.2c}$$

where the nonlinear terms N_{VV} and $N_{V\theta}$ have the following forms

$$N_{VV} = \frac{\partial}{\partial y}\left(\frac{\partial}{\partial x}\widehat{uu} + \frac{\partial}{\partial y}\widehat{uv}\right) - \frac{\partial}{\partial x}\left(\frac{\partial}{\partial x}\widehat{uv} + \frac{\partial}{\partial y}\widehat{vv}\right), \tag{2.3.3a}$$

$$N_{V\theta} = \frac{\partial}{\partial x}\widehat{u\theta} + \frac{\partial}{\partial y}\widehat{v\theta}. \tag{2.3.3b}$$

In the above, symbol $\widehat{uu}$ denotes a product of two functions. The boundary conditions assume the form of

$$\frac{\partial \psi}{\partial y}(y_L(x)) = \frac{\partial \psi}{\partial y}(y_U(x)) = 0, \tag{2.3.4a}$$

$$\frac{\partial \psi}{\partial x}(y_L(x)) = \frac{\partial \psi}{\partial x}(y_U(x)) = 0, \tag{2.3.4b}$$

$$\theta(y_L(x)) = \theta_L(x), \tag{2.3.4c}$$

$$\theta(y_U(x)) = \theta_U(x). \tag{2.3.4d}$$

We wish to determine solution of the above problem with spectral accuracy. The difficulties associated with the irregularity of the flow domain will be solved using the Immersed Boundary Conditions (IBC) concept. In this method, we use a fixed rectangular computational domain sufficiently large to contain the flow domain in its

interior. Our computational domain extends over one period in the *x*-direction and over $(-1 - y_b, 1 + y_t)$ in the *y*-direction, where y_t and y_b denote locations of extremities of the upper and lower plates, respectively (see Fig.2.1). The flow boundary conditions cannot be enforced directly and, thus, one needs to develop equivalent constraints.

We shall use the Chebyshev expansions for discretization in the transverse direction and, in order to use their standard definition, the *y*-extent of the computational domain needs to be mapped into $(-1, 1)$. Mapping of the form

$$\hat{y} = 2\left[\frac{y-(1+y_t)}{y_t+y_b+2}\right] + 1, \tag{2.3.5}$$

is used in the present work. The flow problem expressed using $(x, \hat{y})$ coordinates has the form

$$\frac{\partial^4 \psi}{\partial x^4} + 2\Gamma^2 \frac{\partial^4 \psi}{\partial x^2 \partial \hat{y}^2} + \Gamma^4 \frac{\partial^4 \psi}{\partial \hat{y}^4} - Pr^{-1}\frac{\partial \theta}{\partial x} = N_{VV}, \tag{2.3.6a}$$

$$\frac{\partial^2 \theta}{\partial x^2} + \Gamma^2 \frac{\partial^2 \theta}{\partial \hat{y}^2} = Pr\, N_{V\theta}, \tag{2.3.6b}$$

$$Q(x)|_{mean} = \psi(\hat{y}_U(x))|_{mean} - \psi(\hat{y}_L(x))|_{mean} = \frac{4}{3}Re, \tag{2.3.6c}$$

where $\Gamma = \frac{d\hat{y}}{dy} = \frac{2}{y_t+y_b+2}$ and the nonlinear terms change to the following form

$$N_{VV} = \Gamma\frac{\partial}{\partial \hat{y}}\left(\frac{\partial}{\partial x}\widehat{uu} + \Gamma\frac{\partial}{\partial \hat{y}}\widehat{uv}\right) - \frac{\partial}{\partial x}\left(\frac{\partial}{\partial x}\widehat{uv} + \Gamma\frac{\partial}{\partial \hat{y}}\widehat{vv}\right), \tag{2.3.7a}$$

$$N_{V\theta} = \frac{\partial}{\partial x}\widehat{u\theta} + \Gamma\frac{\partial}{\partial \hat{y}}\widehat{v\theta}. \tag{2.3.7b}$$

The boundary conditions have the form of

$$\frac{\partial \psi}{\partial \hat{y}}(\hat{y}_L(x)) = 0, \qquad \frac{\partial \psi}{\partial \hat{y}}(\hat{y}_U(x)) = 0, \tag{2.3.8a}$$

$$\frac{\partial \psi}{\partial x}(\hat{y}_L(x)) = 0, \qquad \frac{\partial \psi}{\partial x}(\hat{y}_U(x)) = 0, \tag{2.3.8b}$$

$$\theta(\hat{y}_L(x)) = \theta_L(x), \qquad \theta(\hat{y}_U(x)) = \theta_U(x), \tag{2.3.8c}$$

where

$$\hat{y}_L(x) = 1 + \Gamma(y_b \cos(\alpha x) - y_t - 2), \tag{2.3.9a}$$

$$\hat{y}_U(x) = 1 + \Gamma y_t(\cos(\alpha x + \Omega_C) - 1). \tag{2.3.9b}$$

One can replace (2.3.8b) with boundary conditions expressing the fact that ψ is constant along each plate. Use of (2.3.8b) is more efficient computationally (see Section 2.4) while specification of ψ along the plates is more convenient for the enforcement of the flow rate constraint (see Eq.2.3.6c).

2.3.1. Discretization of the field equations

We begin discretization by representing the unknowns as well as the nonlinear terms as Fourier expansions of the form

$$\psi(x, \hat{y}) = \sum_{n=-\infty}^{n=+\infty} \varphi^{(n)}(\hat{y}) \, e^{in\alpha x} \approx \sum_{n=-N_M}^{n=N_M} \varphi^{(n)}(\hat{y}) e^{in\alpha x}, \tag{2.3.10a}$$

$$\theta(x, \hat{y}) = \sum_{n=-\infty}^{n=+\infty} \emptyset^{(n)}(\hat{y}) \, e^{in\alpha x} \approx \sum_{n=-N_M}^{n=N_M} \emptyset^{(n)}(\hat{y}) e^{in\alpha x}, \tag{2.3.10b}$$

$$\left[\widehat{uu}, \widehat{uv}, \widehat{vv}, \widehat{u\theta}, \widehat{v\theta}\right](x, \hat{y}) =$$

$$\quad \sum_{n=-\infty}^{n=+\infty} [\widehat{uu}^{(n)}, \widehat{uv}^{(n)}, \widehat{vv}^{(n)}, \widehat{u\theta}^{(n)}, \widehat{v\theta}^{(n)}](\hat{y}) \, e^{in\alpha x} \approx \tag{2.3.10c}$$

$$\quad \sum_{n=-N_M}^{n=N_M} [\widehat{uu}^{(n)}, \widehat{uv}^{(n)}, \widehat{vv}^{(n)}, \widehat{u\theta}^{(n)}, \widehat{v\theta}^{(n)}](\hat{y}) \, e^{in\alpha x},$$

where $\varphi^{(n)} = \varphi^{(-n)*}$, $\emptyset^{(n)} = \emptyset^{(-n)*}$, $\widehat{uu}^{(n)} = \widehat{uu}^{(-n)*}$, $\widehat{uv}^{(n)} = \widehat{uv}^{(-n)*}$, $\widehat{vv}^{(n)} = \widehat{vv}^{(-n)*}$, $\widehat{u\theta}^{(n)} = \widehat{u\theta}^{(-n)*}$, $\widehat{v\theta}^{(n)} = \widehat{v\theta}^{(-n)*}$ represent the reality conditions with * denoting the complex conjugates. Substituting (2.3.10) into (2.3.6) and separating Fourier modes lead to the modal equations of the form

$$D_n^2 \varphi^{(n)} - in\alpha Pr^{-1} \emptyset^{(n)} = N_{VV}^{(n)}, \tag{2.3.11a}$$

$$D_n \emptyset^{(n)} = Pr \, N_{V\theta}^{(n)}, \tag{2.3.11b}$$

for $-N_M < n < N_M$ where $D = d/d\hat{y}$, $D_n = \Gamma^2 D^2 - n^2\alpha^2$, $D_n^2 = \Gamma^4 D^4 - 2n^2\alpha^2\Gamma^2 D^2 + n^4\alpha^4$, $N_{VV}^{(n)} = in\alpha\Gamma D\widehat{uu}^{(n)} + (\Gamma^2 D^2 + n^2\alpha^2)\widehat{uv}^{(n)} - in\alpha\Gamma D\widehat{vv}^{(n)}$, $N_{V\theta}^{(n)} = in\alpha\,\widehat{u\theta}^{(n)} + \Gamma D\,\widehat{v\theta}^{(n)}$. The modal functions are represented in terms of Chebyshev expansions of the form

$$\varphi^{(n)}(\hat{y}) = \sum_{k=0}^{k=\infty} \widehat{G\varphi}_k^{(n)} T_k(\hat{y}) \approx \sum_{k=0}^{k=N_T-1} \widehat{G\varphi}_k^{(n)} T_k(\hat{y}), \tag{2.3.12a}$$

$$\emptyset^{(n)}(\hat{y}) = \sum_{k=0}^{k=\infty} \widehat{G\emptyset}_k^{(n)} T_k(\hat{y}) \approx \sum_{k=0}^{k=N_T-1} \widehat{G\emptyset}_k^{(n)} T_k(\hat{y}), \tag{2.3.12b}$$

$$[\widehat{uu}^{(n)}, \widehat{uv}^{(n)}, \widehat{vv}^{(n)}, \widehat{u\theta}^{(n)}, \widehat{v\theta}^{(n)}](\hat{y}) =$$

$$\sum_{k=0}^{k=\infty}[\widehat{Guu}_k^{(n)}, \widehat{Guv}_k^{(n)}, \widehat{Gvv}_k^{(n)}, \widehat{Gu\theta}_k^{(n)}, \widehat{Gv\theta}_k^{(n)}] T_k(\hat{y}) \approx$$

$$\sum_{k=0}^{k=N_T-1}[\widehat{Guu}_k^{(n)}, \widehat{Guv}_k^{(n)}, \widehat{Gvv}_k^{(n)}, \widehat{Gu\theta}_k^{(n)}, \widehat{Gv\theta}_k^{(n)}] T_k(\hat{y}), \tag{2.3.12c}$$

where T_k denotes the Chebyshev polynomial of the first kind of order k and $\widehat{Gxx}_k^{(n)}$ denotes the unknown expansion coefficients. Substitution of (2.3.12) into (2.3.11) gives the following expressions

$$\sum_{k=0}^{k=N_T-1}\Big[\big(\Gamma^4 D^4 T_k(\hat{y}) - 2n^2\alpha^2\Gamma^2 D^2 T_k(\hat{y}) + n^4\alpha^4 T_k(\hat{y})\big)\widehat{G\varphi}_k^{(n)} -$$

$$in\alpha Pr^{-1} T_k(\hat{y})\widehat{G\emptyset}_k^{(n)}\Big] - N_{VV}^{(n,k)} = Res_1(\hat{y}), \tag{2.3.13a}$$

$$\sum_{k=0}^{k=N_T-1}\Big[\big(\Gamma^2 D^2 T_k(\hat{y}) - n^2\alpha^2 T_k(\hat{y})\big)\widehat{G\emptyset}_k^{(n)}\Big] - Pr\, N_{V\theta}^{(n,k)} = Res_2(\hat{y}), \tag{2.3.13b}$$

where the modal functions for the nonlinear terms have been represented as Chebyshev expansions of the form

$$N_{VV}^{(n,k)} = \sum_{k=0}^{k=N_T-1}\Big[in\alpha\Gamma D T_k(\hat{y})\widehat{Guu}_k^{(n)} +$$

$$(\Gamma^2 D^2 T_k(\hat{y}) + n^2\alpha^2 T_k(\hat{y}))\widehat{Guv}_k^{(n)} - in\alpha\Gamma D T_k(\hat{y})\widehat{Gvv}_k^{(n)}\Big], \tag{2.3.14a}$$

$$N_{V\theta}^{(n,k)} = \sum_{k=0}^{k=N_T-1}\Big[in\alpha T_k(\hat{y})\widehat{Gu\theta}_k^{(n)} + \Gamma D T_k(\hat{y})\widehat{Gv\theta}_k^{(n)}\Big], \tag{2.3.14b}$$

and Res_1 and Res_2 denote residua. The nonlinear terms are considered to be known during iterative solution. Evaluation of the relevant modal functions and their representation in terms of Chebyshev expansions will be discussed later in this presentation.

The algebraic equations for the expansion coefficients are constructed using the Galerkin projection method by setting projections of the residua onto the base functions of the Chebyshev expansions to zero. This leads to N_T equations for each Fourier mode. The projections are evaluated using the inner product defined as $\langle Res(\hat{y}), T_k(\hat{y}) \rangle = \int_{-1}^{1} Res(\hat{y}) T_k(\hat{y}) \, \omega(\hat{y}) d\hat{y}$ where the weight function has the form $\omega = (1 - \hat{y}^2)^{-1/2}$. The projection equations can be brought to the following form

$$
\begin{aligned}
\sum_{k=0}^{k=N_T-1} & \Big[\big(\Gamma^4 < T_j, D^4 T_k > -2n^2\alpha^2\Gamma^2 < T_j, D^2 T_k > \\
& + n^4\alpha^4 < T_j, T_k > \big) \widehat{G\varphi}_k^{(n)} - in\alpha Pr^{-1} < T_j, T_k > \widehat{G\phi}_k^{(n)} \Big] = \\
& \sum_{k=0}^{k=N_T-1} \Big[in\alpha\Gamma < T_j, DT_k > \widehat{Guu}_k^{(n)} + \big(\Gamma^2 < T_j, D^2 T_k > \\
& + n^2\alpha^2 < T_j, T_k > \big) \widehat{Guv}_k^{(n)} - in\alpha\Gamma < T_j, DT_k > \widehat{Gvv}_k^{(n)} \Big], \quad 0 \leq j \leq N_T - 5,
\end{aligned}
\tag{2.3.15a}
$$

$$
\begin{aligned}
\sum_{k=0}^{k=N_T-1} & \Big[\big(\Gamma^2 < T_j, D^2 T_k > -n^2\alpha^2 < T_j, T_k > \big) \widehat{G\phi}_k^{(n)} \Big] = \\
& Pr \sum_{k=0}^{k=N_T-1} \Big[in\alpha < T_j, T_k > \widehat{Gu\theta}_k^{(n)} + \Gamma < T_j, DT_k > \widehat{Gv\theta}_k^{(n)} \Big], \\
& 0 \leq j \leq N_T - 3,
\end{aligned}
\tag{2.3.15b}
$$

where only the leading $N_T - 4$ equations resulting from the momentum equations and $N_T - 2$ of the leading equations resulting from the energy equations are retained in order to provide space for the boundary conditions (Tau method). The inner products appearing in (2.3.15) can be evaluated analytically as explained in Appendix A.

2.3.2. Discretization of the boundary conditions

The temperature and flow boundary conditions are to be implemented along the plates located inside the computational domain. While the problem formulation given in Section 2.2.2 assumes that the boundary shapes are represented by a single Fourier mode, the

description of the discretization is generalized to include boundaries described by arbitrary Fourier expansions. Construction of constraints equivalent to these conditions at the upper plate is described below while construction for the lower plate can be developed following a similar process. Substituting (2.3.10a,b) into (2.3.8) results in the boundary conditions of the form

$$\sum_{n=-N_M}^{n=+N_M} \frac{\partial \varphi^{(n)}(\hat{y}_U(x))}{\partial \hat{y}} e^{in\alpha x} = 0, \tag{2.3.16a}$$

$$\sum_{n=-N_M}^{n=+N_M} n \, \varphi^{(n)}(\hat{y}_U(x)) e^{in\alpha x} = 0, \tag{2.3.16b}$$

$$\sum_{n=-N_M}^{n=+N_M} \emptyset^{(n)}(\hat{y}_U(x)) e^{in\alpha x} = \theta_U(x). \tag{2.3.16c}$$

The reader may note that (2.3.16b) does not provide conditions for $n = 0$. Substitution of the Chebyshev expansions for the modal functions leads to

$$\sum_{n=-N_M}^{n=+N_M} \sum_{k=0}^{k=N_T-1} \widehat{G\varphi}_k^{(n)} DT_k(\hat{y}_U(x)) e^{in\alpha x} = 0, \tag{2.3.17a}$$

$$\sum_{n=-N_M}^{n=+N_M} \sum_{k=0}^{k=N_T-1} n\widehat{G\varphi}_k^{(n)} T_k(\hat{y}_U(x)) e^{in\alpha x} = 0, \tag{2.3.17b}$$

$$\sum_{n=-N_M}^{n=+N_M} \sum_{k=0}^{k=N_T-1} \widehat{G\emptyset}_k^{(n)} T_k(\hat{y}_U(x)) e^{in\alpha x} = \theta_U(x). \tag{2.3.17c}$$

It is convenient to express shapes of the plates using exponential notation in the form of

$$\hat{y}_L(x) = \sum_{n=-N_A}^{n=N_A} A_L^{(n)} e^{in\alpha x}, \tag{2.3.18a}$$

$$\hat{y}_U(x) = \sum_{n=-N_A}^{n=N_A} A_U^{(n)} e^{in\alpha x}, \tag{2.3.18b}$$

where N_A modes are used in order to capture more complex shapes, $A_L^{(n)}$ and $A_U^{(n)}$ are the known expansions coefficients and, in the case of geometry of interest in this analysis (see Eq. (2.3.9)), all coefficients are zero except $A_L^{(0)} = 1 + \Gamma(-2 - y_t), A_U^{(0)} = 1 - \Gamma y_t, \ A_L^{(1)} = 0.5\Gamma, A_U^{(1)} = 0.5\Gamma * e^{i\Omega_c}$.

Values of the Chebyshev polynomials and their derivatives evaluated along the boundary represent periodic functions of x and, thus, can be expressed as Fourier expansions of the form

$$T_k(\hat{y}_U(x)) = \sum_{m=-N_S}^{m=+N_S} \widehat{WU}_k^{(m)} e^{im\alpha x}, \tag{2.3.19a}$$

$$DT_k(\hat{y}_U(x)) = \sum_{m=-N_S}^{m=+N_S} \widehat{DU}_k^{(m)} e^{im\alpha x}, \tag{2.3.19b}$$

where $\widehat{WU}_k^{(m)}$ and $\widehat{DU}_k^{(m)}$ are the expansion coefficients of the Chebyshev polynomials and their derivatives evaluated along the upper plate. These expansions involve $N_S = (N_T - 1) * N_A$ terms as the highest order polynomials is of the order $N_T - 1$. Their evaluation relies on the recurrence relations presented in Appendix A which leads to expressions of the form

$$\widehat{WU}_{k+1}^{(m)} = 2 \sum_{n=-N_A}^{n=+N_A} A_U^{(n)} \widehat{WU}_k^{(m-n)} - \widehat{WU}_{k-1}^{(m)} \qquad for\ k > 1, \tag{2.3.20a}$$

$$\widehat{DU}_{k+1}^{(m)} = 2 \sum_{n=-N_A}^{n=+N_A} A_U^{(n)} \widehat{DU}_k^{(m-n)} - \widehat{DU}_{k-1}^{(m)} + 2\widehat{WU}_k^{(m)}. \tag{2.3.20b}$$

The evaluation process begins with $k = 0$ and results in

$$\widehat{WU}_0^{(0)} = 1, \qquad \widehat{WU}_0^{(m)} = 0\ for\ |m| \geq 1, \qquad \widehat{WU}_1^{(m)} = A_U^{(m)}\ for\ |m| \geq 0, \tag{2.3.21a}$$

$$\widehat{DU}_0^{(m)} = 0 \quad for\ |m| \geq 0, \qquad\qquad \widehat{DU}_1^{(0)} = 1,$$

$$\widehat{DU}_1^{(m)} = 0 \quad for\ |m| \geq 1, \qquad\qquad \widehat{DU}_2^{(m)} = 4A_U^{(m)}\ for\ |m| \geq 0. \tag{2.3.21b}$$

Substituting (3.19) into (3.17) and separating Fourier modes leads to boundary relations of the form

$$\sum_{n=-N_M}^{n=+N_M} \sum_{k=0}^{k=N_T-1} \sum_{m=-N_S}^{m=+N_S} \widehat{G\varphi}_k^{(n)} \widehat{DU}_k^{(m)} e^{i(n+m)\alpha x} =$$

$$\sum_{s=-N_M-N_S}^{s=+N_M+N_S} \sum_{n=-N_M}^{n=N_M} \sum_{k=0}^{k=N_T-1} \widehat{G\varphi}_k^{(n)} \widehat{DU}_k^{(s-n)} e^{is\alpha x} = 0, \tag{2.3.22a}$$

$$\sum_{n=-N_M}^{n=+N_M} \sum_{k=0}^{k=N_T-1} \sum_{m=-N_S}^{m=+N_S} n\widehat{G\varphi}_k^{(n)} \widehat{WU}_k^{(m)} e^{i(n+m)\alpha x} =$$

$$\sum_{s=-N_M-N_S}^{s=+N_M+N_S} \sum_{n=-N_M}^{n=N_M} \sum_{k=0}^{k=N_T-1} n\widehat{G\varphi}_k^{(n)} \widehat{WU}_k^{(s-n)} e^{is\alpha x} = 0, \tag{2.3.22b}$$

$$\sum_{n=-N_M}^{n=+N_M} \sum_{k=0}^{k=N_T-1} \sum_{m=-N_S}^{m=+N_S} \widehat{G\emptyset}_k^{(n)} \, \widehat{WU}_k^{(m)} \, e^{i(n+m)\alpha x} =$$

$$\sum_{s=-N_M-N_S}^{s=+N_M+N_S} \sum_{n=-N_M}^{n=N_M} \sum_{k=0}^{k=N_T-1} \widehat{G\emptyset}_k^{(n)} \, \widehat{WU}_k^{(s-n)} \, e^{is\alpha x} = \theta_U(x),$$

(2.3.22c)

where $s = n + m$. Re-arrangement of indices $n \rightarrow m$ and $s \rightarrow n$ eventually leads to boundary relations for lower and upper plates of the form

$$\sum_{m=-N_M}^{m=N_M} \sum_{k=0}^{k=N_T-1} \widehat{G\varphi}_k^{(m)} \, \widehat{DL}_k^{(n-m)} = 0,$$

(2.3.23a)

$$\sum_{m=-N_M}^{m=N_M} \sum_{k=0}^{k=N_T-1} \widehat{G\varphi}_k^{(m)} \, \widehat{DU}_k^{(n-m)} = 0,$$

(2.3.23b)

$$\sum_{m=-N_M}^{m=N_M} \sum_{k=0}^{k=N_T-1} n \widehat{G\varphi}_k^{(m)} \, \widehat{WL}_k^{(n-m)} = 0,$$

(2.3.23c)

$$\sum_{m=-N_M}^{m=N_M} \sum_{k=0}^{k=N_T-1} n \widehat{G\varphi}_k^{(m)} \, \widehat{WU}_k^{(n-m)} = 0,$$

(2.3.23d)

$$\sum_{m=-N_M}^{m=N_M} \sum_{k=0}^{k=N_T-1} \widehat{G\emptyset}_k^{(m)} \, \widehat{WL}_k^{(n-m)} = \theta_L^{(n)},$$

(2.3.23e)

$$\sum_{m=-N_M}^{m=N_M} \sum_{k=0}^{k=N_T-1} \widehat{G\emptyset}_k^{(m)} \, \widehat{WU}_k^{(n-m)} = \theta_U^{(n)},$$

(2.3.23f)

where $-N_f \leq n \leq N_f$ with $N_f = N_S + N_M$. In the particular case studied in this work, all $\theta_L^{(n)}$ and $\theta_U^{(n)}$ are zero except for $\theta_L^{(0)} = Ra_{uni}$, $\theta_L^{(1)} = 0.25 \, Ra_{p,L} \, e^{i\Omega_{TL}}$, $\theta_U^{(1)} = 0.25 \, Ra_{p,U} \, e^{i(\Omega_C + \Omega_{TU})}$ in view of (2.2.5).

Since the number of the modal equations for each unknown is $(2N_M + 1)$ and each boundary condition leads to $2N_f + 1$ boundary relations, only the leading $2N_M + 1$ of these relations can be enforced directly. The remaining relations can be used for testing the consistency of the algorithm. It is possible to use the additional relations which lead to the overdetermined formulation of the same problem [63]. We shall come back to this issue in Section 2.7.

2.3.3. Discretization of the flow rate constraint

Substitution of (2.3.10a) and (2.3.12a) into (2.3.2c) results in

$$Q(x) = \sum_{n=-N_M}^{n=N_M} \sum_{k=0}^{k=N_T-1} \widehat{G\varphi}_k^{(n)} \left[T_k\big(\hat{y}_U(x)\big) - T_k\big(\hat{y}_L(x)\big) \right] e^{in\alpha x} = \frac{4}{3} Re.$$

(2.3.24)

Substitution of (2.3.19) into (2.3.24) results in

$$Q(x) = \sum_{n=-N_M}^{n=N_M} \sum_{k=0}^{k=N_T-1} \sum_{m=-N_S}^{m=N_S} \widehat{G\varphi}_k^{(n)} (\widehat{WU}_k^{(m)} - \widehat{WL}_k^{(m)}) e^{i(n+m)\alpha x} =$$

$$\sum_{s=-N_S-N_m}^{s=N_S+N_m} \sum_{n=-N_M}^{n=N_M} \sum_{k=0}^{k=N_T-1} \widehat{G\varphi}_k^{(n)} (\widehat{WU}_k^{(s-n)} - \widehat{WL}_k^{(s-n)}) e^{is\alpha x} = \frac{4}{3} Re, \qquad (2.3.25)$$

where $s = n + m$. Re-arranging the indices $n \to m$ and $s \to n$ eventually leads to

$$Q(x) = \sum_{n=-N_S-N_M}^{n=N_S+N_M} \sum_{m=-N_M}^{m=N_M} \sum_{k=0}^{k=N_T-1} \widehat{G\varphi}_k^{(m)} (\widehat{WU}_k^{(n-m)} - \widehat{WL}_k^{(n-m)}) e^{in\alpha x}. \qquad (2.3.26)$$

Since mode zero from the above expansion represents the mean flow, prescribing its value is equivalent to the imposition of the flow rate constraint, i.e.

$$Q(x)|_{mean} = \sum_{m=-N_M}^{m=N_M} \sum_{k=0}^{k=N_T-1} \widehat{G\varphi}_k^{(m)} (\widehat{WU}_k^{(m)*} - \widehat{WL}_k^{(m)*}) = \frac{4}{3} Re. \qquad (2.3.27)$$

2.4. Solution Process

The solution process relies on iterations and yields new approximations of $\widehat{G\varphi}_k^{(n)}$ and $\widehat{G\emptyset}_k^{(n)}$, denoted as $\left[\widehat{G\varphi}_k^{(n)}\right]^{(l+1)}$ and $\left[\widehat{G\emptyset}_k^{(n)}\right]^{(l+1)}$, at each iteration where the superscript l denotes the iteration number. The nonlinear terms on the right hand side of (2.3.15) are taken from the previous iteration (these terms are ignored during the first iteration) resulting in the first order fixed point method. The iteration process can be summarized as

$$\left[\widehat{G\varphi}_k^{(n)}\right]^{(l+1)} = \left[\widehat{G\varphi}_k^{(n)}\right]^{(l)} + RF_\varphi \left\{\left[\widehat{G\varphi}_k^{(n)}\right]^{(comp)} - \left[\widehat{G\varphi}_k^{(n)}\right]^{(l)}\right\}, \tag{2.4.1a}$$

$$\left[\widehat{G\emptyset}_k^{(n)}\right]^{(l+1)} = \left[\widehat{G\emptyset}_k^{(n)}\right]^{(l)} + RF_\emptyset \left\{\left[\widehat{G\emptyset}_k^{(n)}\right]^{(comp)} - \left[\widehat{G\emptyset}_k^{(n)}\right]^{(l)}\right\}, \tag{2.4.1b}$$

where the superscript $comp$ identifies the solution computed at the new iteration, and the process is controlled using the under-relaxation parameters RF_φ and $RF_\emptyset$. Typically, $RF_\varphi < 0.1$ and $RF_\emptyset < 0.1$ were used with their values decreasing with an increase of the corrugation amplitude and wave number, and the Reynolds and Rayleigh numbers. Iterations are stopped when the convergence criterion of the form

$$\frac{\left\|\left[\widehat{G\varphi}_k^{(n)},\right]^{(l+1)} - \left[\widehat{G\varphi}_k^{(n)},\right]^{(l)}\right\|_2}{\left\|\left[\widehat{G\varphi}_k^{(n)}\right]^{(l+1)}\right\|_2} < CONV, \quad \frac{\left\|\left[\widehat{G\emptyset}_k^{(n)}\right]^{(l+1)} - \left[\widehat{G\emptyset}_k^{(n)}\right]^{(l)}\right\|_2}{\left\|\left[\widehat{G\emptyset}_k^{(n)}\right]^{(l+1)}\right\|_2} < CONV, \tag{2.4.2a-b}$$

is satisfied with $CONV = 10^{-14}$ used in all tests reported in this thesis. In the above, the L^2 norm of the difference between the solution vectors computed at two consecutive iterations is placed at the numerator and the L^2 norm of the current solution vector is placed in the denominator. The L^2 norm of a vector V with size n is defined as $\|V\|^2 = \sqrt{(\sum_{i=1}^n |V_i|^2)}$.

The nonlinear terms on the right hand side of (2.3.15) need to be updated at the end of each iteration step. It is more efficient to evaluate the required products by transferring data to the physical space, carrying out the multiplications there and transferring the

results back into the Fourier space (Canuto et al. 2006). Velocity components and temperature are expressed as

$$u(x, \hat{y}) = \Gamma \sum_{n=-N_M}^{n=+N_M} \sum_{k=0}^{k=N_T-1} \widehat{G\varphi}_k^{(n)} DT_k(\hat{y}) e^{in\alpha x}, \tag{2.4.3a}$$

$$v(x, \hat{y}) = -i\alpha \sum_{n=-N_M}^{n=+N_M} \sum_{k=0}^{k=N_T-1} n\widehat{G\varphi}_k^{(n)} T_k(\hat{y}_U(\hat{y})) e^{in\alpha x}, \tag{2.4.3b}$$

$$\theta(x, \hat{y}) = \sum_{n=-N_M}^{n=+N_M} \sum_{k=0}^{k=N_T-1} \widehat{G\emptyset}_k^{(n)} T_k(\hat{y}) e^{in\alpha x}, \tag{2.4.3c}$$

and are evaluated on a suitable grid in the $(x, \hat{y})$ plane. $2N_x + 2$ equidistant points, where $N_x = \frac{3}{2} N_M$, are used along the x-direction in order to remove the aliasing error with the last point removed due to periodicity, and N_T points are used in the $\hat{y}$-direction with the first and last points overlapping with the borders of the computational domain. Chebyshev points defined as $\hat{y}_j = \cos(\frac{j\pi}{N_T-1})$, where $j = 1, 2, \ldots, N_T - 2$, are used in the interior of the domain. This process results in the formation of three matrices containing u, v, θ and their multiplications yield the desired products $\widehat{uu}, \widehat{uv}, \widehat{vv}, \widehat{u\theta}, \widehat{v\theta}$. These products need to be expressed using Fourier expansions (3.10c) which necessitates the determination of the modal functions $\widehat{uu}^{(n)}, \widehat{uv}^{(n)}, \widehat{vv}^{(n)}, \widehat{v\theta}^{(n)}, \widehat{u\theta}^{(n)}$. This is accomplished using the Fast Fourier Transform (FFT) at each $\hat{y}$-location; $2N_x + 1$ data points are used in the x-direction resulting in values of $2N_x + 1$ modal functions. Modal functions with indices in the range $\left[-N_M, N_M\right]$ are retained and the remaining functions are discarded as a part of the aliasing error control process [64]. The last step involves expressing each modal function known on the set of grid points $\hat{y}_j$ in terms of a Chebyshev expansion and this requires evaluation of coefficients $\widehat{Guu}_k^{(n)}, \widehat{Guv}_k^{(n)}, \widehat{Gvv}_k^{(n)}, \widehat{Gu\theta}_k^{(n)}, \widehat{Gv\theta}_k^{(n)}$. This is done by writing equation of type (3.12c) for each grid point resulting in a system of linear equation for the unknown coefficients which is solved numerically. The number of grid points determines the maximum length of the Chebyshev expansion. No de-aliasing is required in the Chebyshev direction if a sufficient number of polynomials are used.

2.5. The Linear Solver

The linear system for $\widehat{G\varphi}_k^{(n)}$ and $\widehat{G\emptyset}_k^{(n)}$ has to be solved at each iteration step. The problem has three types of intermodal couplings, i.e. coupling due to nonlinear terms, coupling between the momentum and energy equations in the linear terms and coupling due to the boundary relations. The former has been eliminated by the use of nonlinear terms from the previous iteration. The remaining two remain and, as result, one needs to solve a very large linear system involving all modal functions at each iterations step. This system can be written in a matrix notation as

$$\begin{bmatrix} L_1 & L_2 \\ 0 & L_3 \end{bmatrix} \begin{bmatrix} V \\ T \end{bmatrix} = \begin{bmatrix} R_1(V,T) \\ R_2(V,T) \end{bmatrix}, \tag{2.5.1}$$

where L_1 denotes the coefficient matrix of size size $p \times p$ with $p = (2N_M + 1)N_T$ arising from the terms in the momentum equation involving stream function and the relevant boundary relations, L_2 denotes the coefficient matrix of size $p \times p$ resulting from the terms in the momentum equation involving temperature and the relevant boundary relations, L_3 denotes the coefficient matrix of size $p \times p$ resulting from the energy equation and the relevant boundary relations, V is the p-dimensional vector of the unknown expansions coefficient $\widehat{G\varphi}_k^{(n)}$, T is the p-dimensional vector of the unknown expansion coefficients $\widehat{G\emptyset}_k^{(n)}$, R_1 stands for the p-dimensional right-hand side vector containing nonlinearities associated with the momentum equation and R_2 stands for the p-dimensional vector containing nonlinearities associated with the energy equation. The structure of (2.5.1) shows that the energy equation is decoupled from the momentum equation resulting in two independent systems of the form

$$L_1 V = -L_2 T + R_1(V,T), \tag{2.5.2a}$$
$$L_3 T = R_2(V,T), \tag{2.5.2b}$$

which permits solution of (2.5.2B) for T to be followed by solution of (2.5.2A) for V.

We shall begin discussion of linear solvers starting with (2.5.2B). The structure of the coefficient matrix L_3 is displayed in Fig. 2.2. The upper triangular blocks correspond to the modal equations and are uncoupled, and the black horizontal lines correspond to the two boundary relations per block which provide coupling. The system can be solved in this form but significant computational savings can be realized by taking advantage of the structure of L_3 following ideas presented in (Husain & Floryan 2013).

(A)   **(B)**
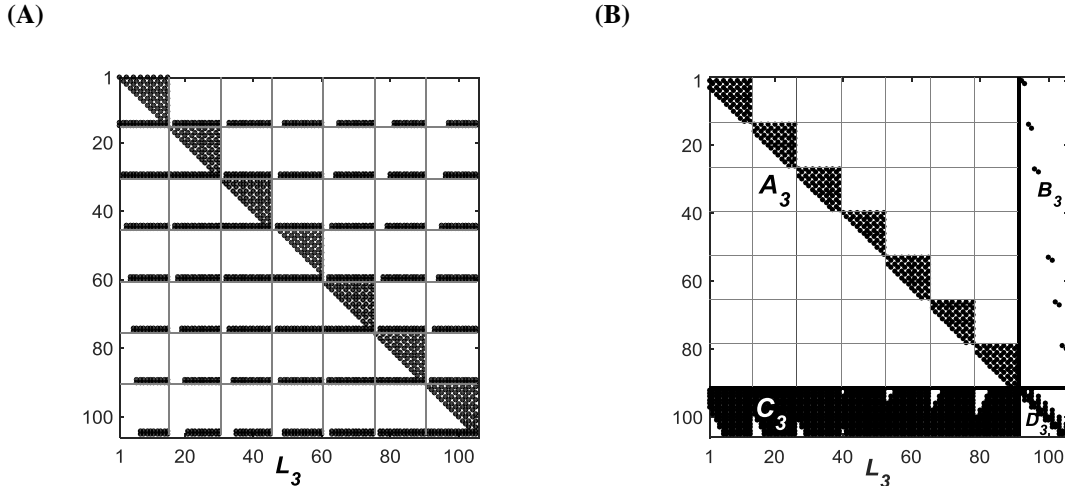
Figure 2.2: Structure of the coefficient matrix L_3 before (Fig. 2.2A) and after (Fig. 2.2B) re-arrangement for $N_M = 3$ and $N_T = 15$. Black dotes identify the non-zero elements and lines indicate borders between blocks associated with different Fourier modes organized according to the mode number $-N_M, \ldots, 0, \ldots, N_M$.

The solution process begins with re-organization of L_3. In the first step all boundary relations are moved to the bottom of L_3 forming a block diagonal matrix L_{31} of size $q \times p$, where $q = (2N_M + 1)(N_T - 2)$ and a full matrix L_{32} of size $r \times p$, where $r = 2(2N_M + 1)$. Extraction of the largest possible square matrix A_3 from L_{31} is carried out in the second step. This is done by moving the unknown Chebyshev coefficients corresponding to the two lowest polynomials in each modal equation to the end of the vector of unknowns. The resulting matrix structure is illustrated in Fig.2.3. The square matrix A_3 of size $q \times q$ has a block diagonal structure with each block of size $(N_T - 2) \times (N_T - 2)$. The rectangular matrix B_3 of size $q \times r$ also has a block diagonal form with blocks of size $(N_T - 2) \times 2$ whereas the full rectangular matrix C_3 has size $r \times q$ and the full square matrix D_3 has size $r \times r$. Matrices B_3 and D_3 contain coefficients

corresponding to $\widehat{G\emptyset}_0^{(n)}$, $\widehat{G\emptyset}_1^{(n)}$ while information associated with the remaining coefficients is stored in matrices A_3 and C_3. The vector of unknowns consists of two parts with T_1 containing unknowns $\widehat{G\emptyset}_k^{(n)}$ for $n \in \langle -N_M, N_M \rangle, k \in \langle 2, N_T - 1 \rangle$, and T_2 containing $\widehat{G\emptyset}_k^{(n)}$ for $n \in \langle -N_M, N_M \rangle, k \in \langle 0,1 \rangle$. Equation (2.5.2b) can now be written as

$$A_3 T_1 + B_3 T_2 = R_{21}, \qquad C_3 T_1 + D_3 T_2 = R_{22} \qquad (2.5.3)$$

where R_{21} contains elements of R_2 corresponding to $n \in \langle -N_M, N_M \rangle, k \in \langle 2, N_T - 1 \rangle$ and R_{22} contains elements of R_2 corresponding to $n \in \langle -N_M, N_M \rangle, k \in \langle 0,1 \rangle$. The solution of (2.5.3) can be written as

$$T_2 = [D_3 - C_3 A_3^{-1} B_3]^{-1}(R_{22} - C_3 A_3^{-1} R_{21}), \qquad T_1 = A_3^{-1}[R_{21} - B_3 T_2]. \qquad (2.5.4)$$

The memory requirements are significantly reduced as one needs to store only the diagonal blocks of matrices A_3 and B_3. Computational savings result from the construction of $A_3^{-1}, C_3 A_3^{-1}, C_3 A_3^{-1} B_3, A_3^{-1} R_{21}, A_3^{-1} B_3$ block by block rather than working with complete matrices. Further efficiencies can be obtained by taking advantage of the complex conjugate properties of the modal functions.

Solver for (2.5.2a) is developed following the same arguments. The re-organization of L_1 involves moving all boundary relations to its bottom forming a block diagonal matrix L_{11} of size $q \times p$, where $q = (2N_M + 1)(N_T - 4)$ and a full matrix L_{12} of size $r \times p$, where $r = 4(2N_M + 1)$. Extraction of the largest possible square matrix A_1 from L_{11} is carried out in the second step. This is done by moving the unknown Chebyshev coefficients corresponding to the four lowest polynomials in each modal equation to the end of the vector of unknowns. The resulting matrix structure is similar to that shown in Fig.2.3. The square matrix A_1 of size $q \times q$ has a block diagonal structure with each block of size $(N_T - 4) \times (N_T - 4)$. The rectangular matrix B_1 of size $q \times r$ also has a block diagonal form with blocks of size $(N_T - 4) \times 4$ whereas the full rectangular matrix C_1 has size $r \times q$ and the full square matrix D_1 has size $r \times r$. Matrices B_1 and D_1

contain coefficients corresponding to $\widehat{G\varphi}_0^{(n)}$, $\widehat{G\varphi}_1^{(n)}$, $\widehat{G\varphi}_2^{(n)}$, $\widehat{G\varphi}_3^{(n)}$ while information associated with the remaining coefficients is stored in matrices A_1 and C_1. The vector of unknowns consists of two parts with V_1 containing unknowns $\widehat{G\varphi}_k^{(n)}$ for $n \in \langle -N_M, N_M \rangle, k \in \langle 4, N_T - 1 \rangle$, and V_2 containing $\widehat{G\varphi}_k^{(n)}$ for $n \in \langle -N_M, N_M \rangle, k \in \langle 0,3 \rangle$. Equation (2.5.2a) can now be written as

$$A_1 V_1 + B_1 V_2 = R_{11}, \qquad C_1 V_1 + D_1 V_2 = R_{12} \qquad (2.5.3)$$

where R_{11} contains elements of $-L_2 T + R_1(V, T)$ corresponding to $n \in \langle -N_M, N_M \rangle, k \in \langle 4, N_T - 1 \rangle$ and R_{12} contains elements of $-L_2 T + R_1(V, T)$, corresponding to $n \in \langle -N_M, N_M \rangle, k \in \langle 0,3 \rangle$.
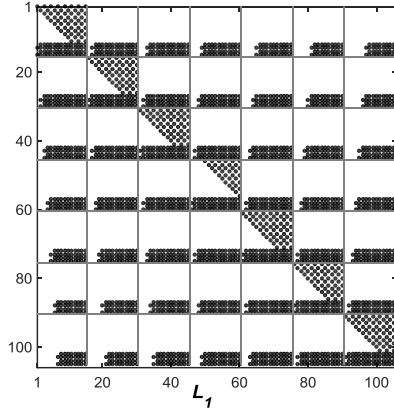
(A)   **(B)**
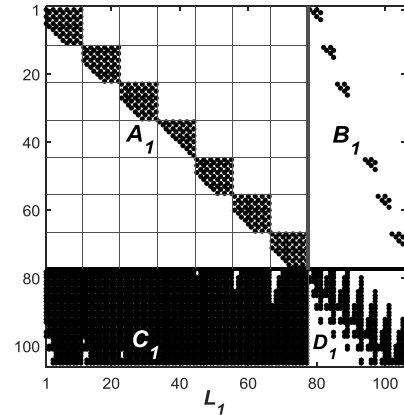
Figure 2.3: Structure of the coefficient matrix L_1 before (Fig. 2.3A) and after (Fig. 2.3B) re-arrangement for $N_M = 3$ and $N_T = 15$. Black dotes identify the non-zero elements and lines indicate borders between blocks associated with different Fourier modes organized according to the mode number $-N_M, \dots, 0, \dots, N_M$.

2.6. Evaluation of the pressure field

The pressure field can be determined from the known velocity field. The x-component of the momentum equation (2.2.6b) is expressed using the stream functions defined by Eq.(2.3.1) and re-arranged to the following form

$$\frac{\partial p}{\partial x} = \Gamma \frac{\partial^3 \psi}{\partial x^2 \partial \hat{y}} + \Gamma^3 \frac{\partial^3 \psi}{\partial \hat{y}^3} - \frac{\partial}{\partial x} \widehat{uu} - \Gamma \frac{\partial}{\partial \hat{y}} \widehat{uv}. \qquad (2.6.1)$$

The pressure field is represented in terms of a Fourier expansion of the form

$$p(x, \hat{y}) = Ax + \sum_{n=-\infty}^{n=+\infty} p^{(n)}(\hat{y}) e^{in\alpha x} \approx Ax + \sum_{n=-N_M}^{n=N_M} p^{(n)}(\hat{y}) e^{in\alpha x}, \qquad (2.6.2)$$

where A has been added for generality purposes. It can be shown that A represents the mean pressure gradient. Substitution of (2.3.10) and (2.6.2) into (2.6.1) and separation of Fourier modes lead to equations for the pressure modal functions of the form

$$A + in\alpha p^{(n)} = (\Gamma^3 D^3 - n^2 \alpha^2 \Gamma D) \varphi^{(n)} - in\alpha \widehat{uu}^{(n)} - \Gamma D \widehat{uv}^{(n)}. \qquad (2.6.3)$$

The mean pressure gradient can be determined form the modal equation for mode 0 which has the following form

$$A = \Gamma^3 D^3 \varphi^{(0)} - \Gamma D \widehat{uv}^{(0)}. \qquad (2.6.4)$$

Substitution of (2.3.12a) and (2.3.12c) into (2.6.4) leads to an expression of the form

$$A = \sum_{k=0}^{k=N_T-1} \left[\Gamma^3 \widehat{G\varphi}_k^{(0)} D^3 T_k(\hat{y}) - \Gamma \widehat{Guv}_k^{(0)} D T_k(\hat{y}) \right], \qquad (2.6.5)$$

which can be used for evaluation of A. It is convenient for interpretation purposes to extract the pressure gradient correction A_C induced by the heating and the grooves by subtracting the pressure gradient associated with the flow in a smooth isothermal channel from the total pressure gradient, i.e.

$$A = -2Re + A_C. \tag{2.6.6}$$

This correction can be obtained directly from the following relation

$$A_c = \sum_{k=0}^{k=N_T-1} \left[\Gamma^3 \, \widehat{G\varphi}_k^{(0)} D^3 T_k(\hat{y}) - \Gamma \widehat{Guv}_k^{(0)} DT_k(\hat{y}) \right] + 2Re, \tag{2.6.7}$$

which can be evaluated at any $\hat{y}$. It has been verified that A_c computed using (2.6.7) does not depend on $\hat{y}$ which verifies the integrity of the algorithm.

The other pressure modal functions can be evaluated from (2.6.3) written in the following form

$$p^{(n)}(\hat{y}) = \frac{1}{in\alpha} \left[(\Gamma^3 D^3 - n^2\alpha^2 \Gamma D) \, \varphi^{(n)} - in\alpha \, \widehat{uu}^{(n)} - \Gamma D \, \widehat{uv}^{(n)} \right]. \tag{2.6.8}$$

It is obvious that the above equation cannot be used for $n = 0$. Substitution of (2.3.12) into (2.6.8) results in

$$p^{(n)}(\hat{y}) = \frac{1}{in\alpha} \sum_{k=0}^{k=N_T-1} \left[\Gamma^3 \widehat{G\varphi}_k^{(n)} D^3 T_k(\hat{y}) - n^2\alpha^2 \Gamma \widehat{G\varphi}_k^{(n)} DT_k(\hat{y}) - \right.$$
$$\left. in\alpha \widehat{Guu}_k^{(n)} T_k(\hat{y}) - \Gamma \widehat{Guv}_k^{(n)} DT_k(\hat{y}) \right], \tag{2.6.9}$$

which is used for evaluation of $p^{(n)}$. The modal function $p^{(0)}$ needs to be evaluated from the *y*-momentum equation. This equation can be re-arranged to the following form

$$\Gamma \frac{\partial p}{\partial \hat{y}} = -\frac{\partial^3 \psi}{\partial x^3} + \Gamma^2 \frac{\partial^3 \psi}{\partial x \partial \hat{y}^2} + Pr^{-1} \theta - \frac{\partial}{\partial x} \widehat{uu} - \Gamma \frac{\partial}{\partial \hat{y}} \widehat{vv}. \tag{2.6.10}$$

Extraction of mode 0 results in the following relation

$$\Gamma Dp^{(0)} = Pr^{-1} \emptyset^{(0)} - \Gamma D\widehat{vv}^{(0)}. \tag{2.6.11}$$

Substitution of (2.3.12) and integration of the resulting relation lead to

$$p^{(0)}(\hat{y}) = \Gamma^{-1}Pr^{-1}\int_{-1}^{\hat{y}}\emptyset^{(0)}d\hat{y} - \widehat{vv}^{(0)}.$$ (2.6.12)

Use of Chebyshev expansions (2.3.12) in (2.6.12) results in an expression used for evaluation of $p^{(0)}(\hat{y})$, i.e.

$$p^{(0)}(\hat{y}) = \sum_{k=0}^{k=N_T-1}\left[\Gamma^{-1}Pr^{-1}\widehat{G\emptyset}_k^{(0)}I_k(\hat{y}) - \widehat{Gvv}_k^{(0)}T_k(\hat{y})\right],$$ (2.6.13)

where $I_k(\hat{y}) = \int_{-1}^{\hat{y}}T_k(\hat{y})$ can be expressed analytically in terms of Chebyshev polynomials (see Appendix A for details).

2.7. Performance of the Algorithm

The main advantage of the present algorithm is the spectral accuracy achieved for the geometrically complex flow domain. We shall describe various tests carried out in order to demonstrate that the algorithm does indeed deliver the predicted accuracy.

In a spectrally accurate algorithm, the solution converges exponentially as the number of Chebyshev polynomials N_T and the number of Fourier modes N_M used in the computations increase. To demonstrate the character of convergence as the number of Chebyshev polynomials N_T increases, we define the errors of the field quantities in the form of

$$Er_1 = \frac{||u_{ref}(x,y)-u(x,y)||_2}{\left\|u_{ref}(x,y)\right\|_2}, \qquad Er_2 = \frac{||\theta_{ref}(x,y)-\theta(x,y)||_2}{||\theta_{ref}(x,y)||_2}.$$ (2.7.1a-b)

Here $||X_{ref} - X||^2$ is the L^2 norm of the difference between the reference solution and the solution obtained with the prescribed N_T and N_M , and $||X_{ref}||^2$ is the L^2 norm of the reference solution. The solutions have been evaluated on the same grid points as used for FFT in Section 2.4. The L^2 norm of a matrix A with size $m \times n$ is equal to its largest

singular value, i.e. $||A||_2 = max(SVD(A))$. The evaluation of SVD is discussed later in this presentation. Er_1 measures the accuracy of determination of the velocity field and is based on the x-velocity component as this is a stricter error measure. This is so because the numerical solution is carried out for the stream function and the x-velocity component is defined as the derivative of the stream function which results in a larger absolute error. Er_2 measures the accuracy of determination of the temperature field. As the exact reference solution is not available, the reference solution has been determined numerically using using $N_T = 80$ Chebyshev polynomials and $N_M = 40$ Fourier modes. The errors of such solutions are below machine level and, thus, the exact solutions and the numerical constructed reference solutions are the same within the double precision accuracy used in the tests. To test error variation as a function of N_T, a large number of Fourier modes ($N_M = 30$) is used in order to eliminate the error associated with the x-discretization. Results displayed in Fig.2.4 clearly demonstrate the exponential reduction of the error when the number of Chebyshev polynomials N_T increases which confirms the spectral convergence of the y-discretization. To test error variations as a function of N_M, a large number of Chebyshev polynomials ($N_T = 80$) has been used in order to eliminate error associated with the y-discretization. Results displayed in Fig.2.5 clearly demonstrate the exponential reduction of the error when the number of Fourier modes N_M increases which confirms the spectral convergence of the x-discretization.

(A) (B)
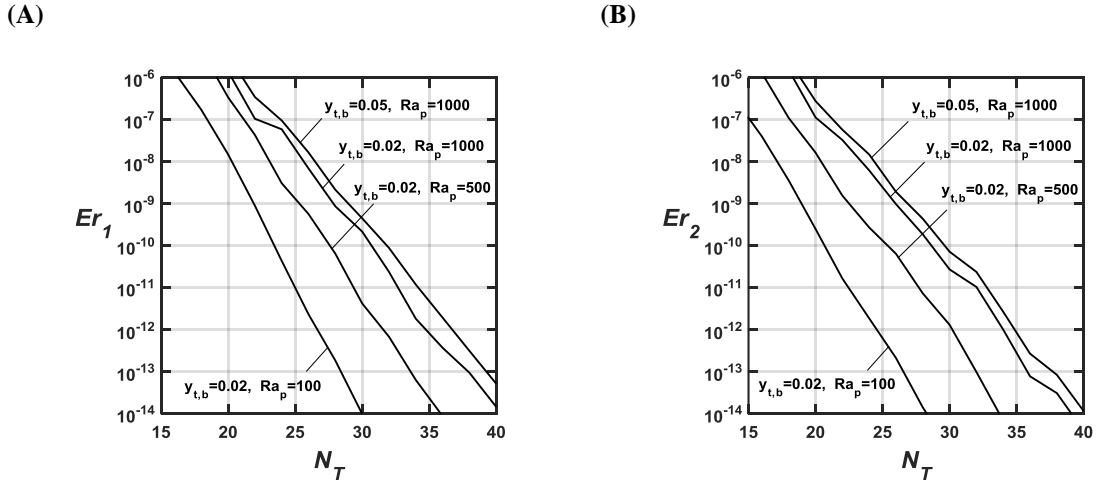
Figure 2.4: Variations of the errors Er_1 (Fig. 2.4A) and Er_2 (Fig. 2.4B) as functions of the number of Chebyshev polynomials N_T used in the computations for $\alpha = 2$, $Re = 1$, $Ra_{uni} = 0$, $Pr = 0.71$, $\Omega_{TL} = \pi/2$, $\Omega_{TU} = \pi/2$, $\Omega_C = 0$, $y_t = y_b = y_{t,b}$, $Ra_{p,U} = Ra_{p,L} = Ra_p$.

(A)
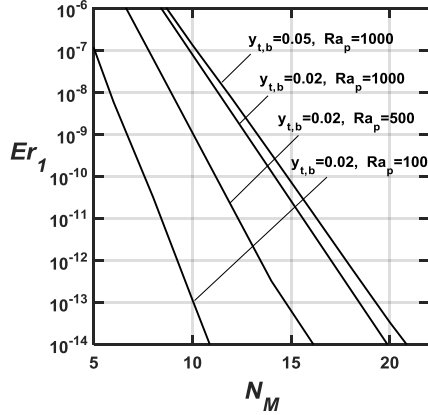
(B)
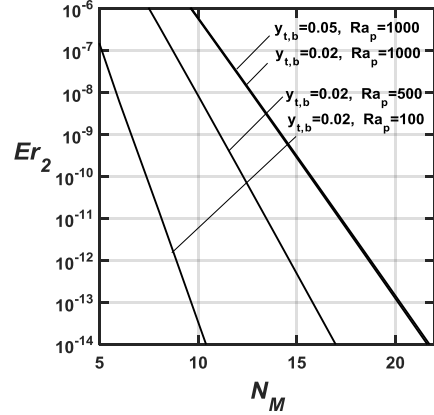
Figure 2.5: Variations of the errors Er_1 (Fig. 2.5A) and Er_2 (Fig. 2.5B) as functions of the number of Fourier modes N_M used in the computations for $\alpha = 2$, $Re = 1$, $Ra_{uni} = 0$, $Pr = 0.71$, $\Omega_{TL} = \pi/2$, $\Omega_{TU} = \pi/2$, $\Omega_C = 0$, $y_{t,b} = y_b = y_t$, $Ra_p = Ra_{p,U} = Ra_{p,L}$.

The convergence of the Fourier expansions can be assessed by looking at the magnitudes of the modal functions $D\Phi^{(n)}$ and $\emptyset^{(n)}$ which can be measured using Chebyshev norms defined as

$$\left\|D\varphi^{(n)}\right\|_\omega = \left\{\int_{-1}^{1} D\varphi^{(n)}(\hat{y}) \cdot D\varphi^{(n)*}(\hat{y}) \cdot \omega(\hat{y}) \cdot d\hat{y}\right\}^{1/2}, \tag{2.7.2a}$$

$$\left\|\emptyset^{(n)}\right\|_\omega = \left\{\int_{-1}^{1} \emptyset^{(n)}(\hat{y}) \cdot \emptyset^{(n)*}(\hat{y}) \cdot \omega(\hat{y}) \cdot d\hat{y}\right\}^{1/2}, \tag{2.7.2b}$$

where $\omega = 1/\sqrt{1 - \hat{y}^2}$ and the superscript n corresponds to the mode number. All tests have been carried out using a large number of Chebyshev polynomials ($N_T = 80$) in order to reduce error associated with the y-discretization below the machine level. Results displayed in Fig. 2.6 demonstrate the exponential decrease of both norms with the Fourier mode number n which confirms the spectral convergence of the x-discretization.
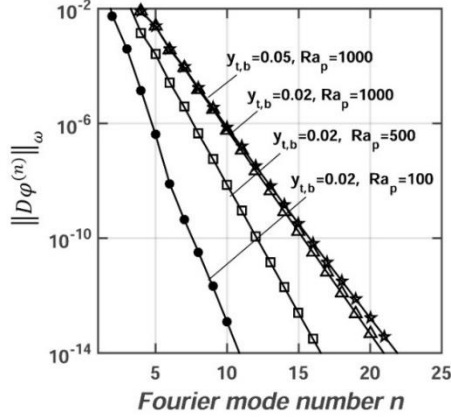
(A)   **(B)**
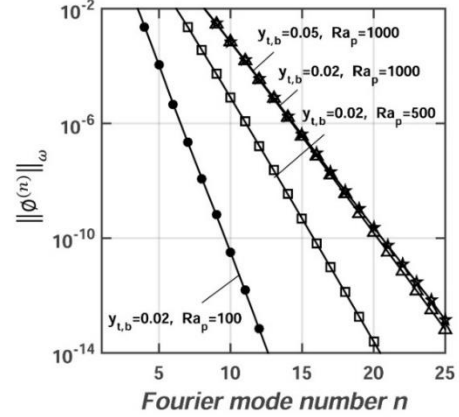
Figure 2.6: Variations of the Chebyshev norms of $D\varphi^{(n)}$ (Fig.2.6A) and $\emptyset^{(n)}$ (Fig.2.6B) as functions of the Fourier mode number n for $\alpha = 2$, $Re = 1$, $Ra_{uni} = 0$, $Pr = 0.71$, $\Omega_{TL} = \pi/2$, $\Omega_{TU} = \pi/2$, $\Omega_C = 0$, $N_T = 80$, $N_M = 25$.

The overall accuracy of the IBC method is dominated by the accuracy in the enforcement of boundary conditions. Conditions (2.2.7) state that $u(y_L(x))$, $u(y_U(x))$, $v(y_L(x))$, $v(y_U(x))$, $\theta(y_L(x)) - \theta_L(x)$, $\theta(y_U(x)) - \theta_U(x)$ are to be zero along the plates. Accordingly, their values define boundary errors of the form $u_{Le} = u(y_L(x))$, $u_{Ue} = u(y_U(x))$, $v_{Le} = v(y_L(x))$, $v_{Ue} = v(y_U(x))$, $\theta_{Le} = \theta(y_L(x)) - \theta_L(x)$, $\theta_{Ue} = \theta(y_U(x)) - \theta_U(x)$ which provide a means for assessing the error of the whole method. It is convenient to use the L^∞ norms defined for the lower plate

$$\|u_{Le}\|_\infty = sup\ |u(x, y_L)|, \qquad\qquad 0 \le x \le \lambda, \qquad\qquad\qquad (2.7.3a)$$
$$\|\theta_{Le}\|_\infty = sup|\theta(x, y_L) - \theta_L(x)|, \qquad 0 \le x \le \lambda, \qquad\qquad\qquad (2.7.3b)$$

as an explicit measure of this error. Similar norms for the upper plate can be easily introduced. Results displayed in Fig.2.7 demonstrate that both norms decrease exponentially as the number of Fourier modes N_M used in the computations increase and this further demonstrates the spectral convergence of the algorithm.
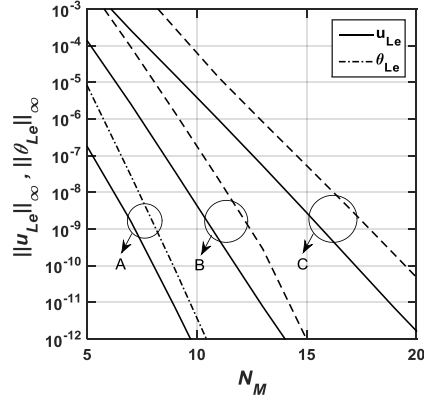
Figure 2.7: Variations of $\|u_{Le}\|_\infty$ and $\|\theta_{Le}\|_\infty$ as functions of the number of Fourier modes N_M used in the computations for $\alpha = 2$, $Re = 1$, $Ra_{uni} = 0$, $Pr = 0.71$, $\Omega_{TL} = \pi/2$, $\Omega_{TU} = \pi/2$, $\Omega_C = 0$, $N_T = 80$. Case A: $Ra_{p,U} = Ra_{p,L} = 100$, $y_t = y_b = 0.02$; Case B: $Ra_{p,U} = Ra_{p,L} = 500$, $y_t = y_b = 0.02$; Case C: $Ra_{p,U} = Ra_{p,L} = 1000$, $y_t = y_b = 0.05$.

Distributions of $u_{Le}(x)$ and $\theta_{Le}(x)$ along the heated plate provide further information about the properties of the method. Typical distributions shown in Fig.2.8 demonstrate that the locations of the maximum errors coincide with the largest channel opening. These errors are generated by truncating the Fourier expansions and, thus, they consist of higher Fourier modes. As the modal functions for the higher Fourier modes have large amplitudes close to the edge of the computational domain, the truncations of the Fourier expansions have a greater effect in the valley position than in the crest position. The Fourier spectra of $u_{Le}(x)$ and $\theta_{Le}(x)$ are defined as

$$u_{Le}(x) = \sum_{n=-\infty}^{\infty} U_{Le}^{(n)} e^{in\alpha x}, \tag{2.7.5a}$$

$$\theta_{Le}(x) = \sum_{n=-\infty}^{\infty} \theta_{Le}^{(n)} e^{in\alpha x}, \tag{2.7.5b}$$

and their distributions are shown in Fig.2.9. These spectra have no components for $n < N_M$ which is consistent with the construction of boundary relations described in Section 2.3.2. They consist entirely of higher modes discarded in the solution process.
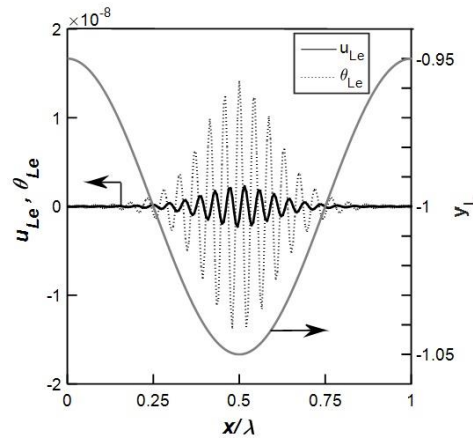
Figure 2.8: Distributions of the boundary errors $u_{Le}(x)$ and $\theta_{Le}(x)$ along the lower plate for $\alpha = 5$, $Re = 5$, $y_t = y_b = 0.05$, $Pr = 0.71$, $Ra_{p,U} = Ra_{p,L} = 500$, $Ra_{uni} = 0$, $\Omega_{TL} = 0$, $\Omega_{TU} = 0$, $\Omega_C = 0$, $N_T = 50$, $N_M = 20$. Thick solid line illustrates the geometry of the plate.
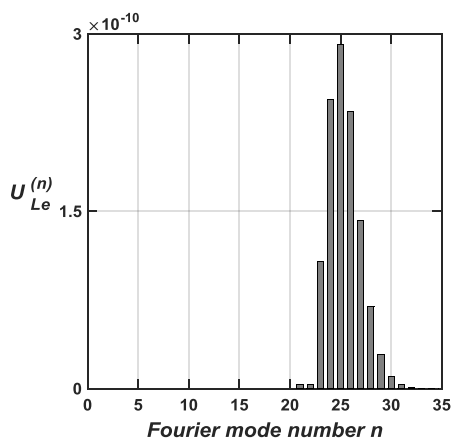
(A)   **(B)**
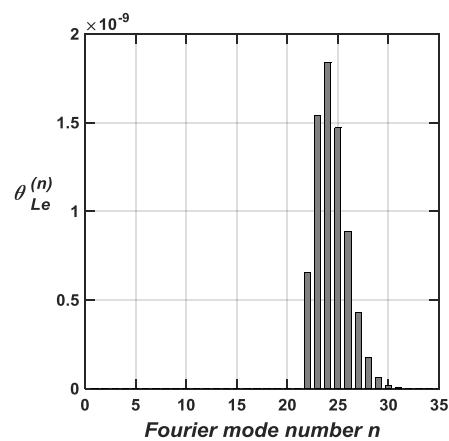
Figure 2.9: Fourier spectra of the error in the enforcement of the boundary conditions for u and θ along the lower plate for $\alpha = 5$, $y_t = y_b = 0.05$, $Ra_{p,U} = Ra_{p,L} = 500$, $Ra_{uni} = 0$, $Pr = 0.71$, $Re = 5$, $Pr = 0.71$, $\Omega_{TL} = 0$, $\Omega_{TU} = 0$, $\Omega_C = 0$, $N_M = 20$, $N_T = 50$. The reader may note the absence of the first 20 modes.

We shall now start discussing effects of various physical parameters present in the problem on the absolute accuracy of the numerical solution. Variations of the boundary errors as functions of the groove geometry are illustrated in Fig.2.10. The errors remain at the machine level as long as $y_{t,b}$ and α remain below certain critical thresholds. When either $y_{t,b}$ or α increases beyond any of these thresholds, the error starts to increase rapidly. While the error increase associated with an increase of the groove amplitude is rather obvious and does not require further discussion, error changes associated with variations of the groove wave number require explanation. The velocity and temperature

field displayed in Fig.2.11 demonstrate that a large change in the flow topology takes place as α increases. The convective motion occurs over the whole domain for $\alpha = 2$ (see Fig.2.11A) while it is confined to a thin boundary layer attached to the corrugated plate for $\alpha = 15$ (see Fig.2.11B). The thickness of this layer is of the same order as the groove amplitude and this leads to the error increase. The error increase for small α is related to the fact that a large number of Fourier modes is required in order to resolve fields with long wavelength (Asgarian et al.). The geometrical thresholds leading to the error increase can be expanded by increasing the number of Fourier modes and Chebyshev polynomials used in the computations. One may need to use an excessively large N_M and N_T in order to significantly increase these thresholds and this places limitations on use of the algorithm for grooves of large amplitudes and short wavelengths. An over-determined formulation discussed in Section 2.8 provides a more efficient alternative.

(A) (B)
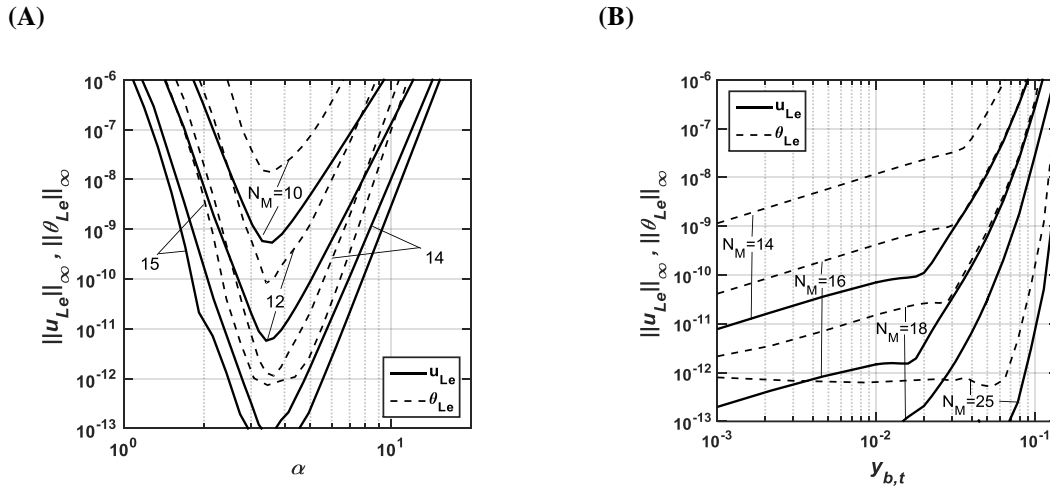
Figure 2.10: Variations of $\|u_{Le}\|_\infty$ and $\|\theta_{Le}\|_\infty$ as functions of the groove wave number α for $y_t = y_b = 0.02$ (Fig. 2.10A) and as functions of the corrugation amplitude $y_{b,t} = y_b = y_t$ for $\alpha = 2$ (Fig. 2.10B) for $Ra_{p,U} = Ra_{p,L} = 1000, Ra_{uni} = 0,\ Re = 1,\ Pr = 0.71,\ \Omega_{TL} = \pi/2,$ $\Omega_{TU} = \pi/2, \Omega_C = 0, N_T = 80$.

(A)   **(B)**
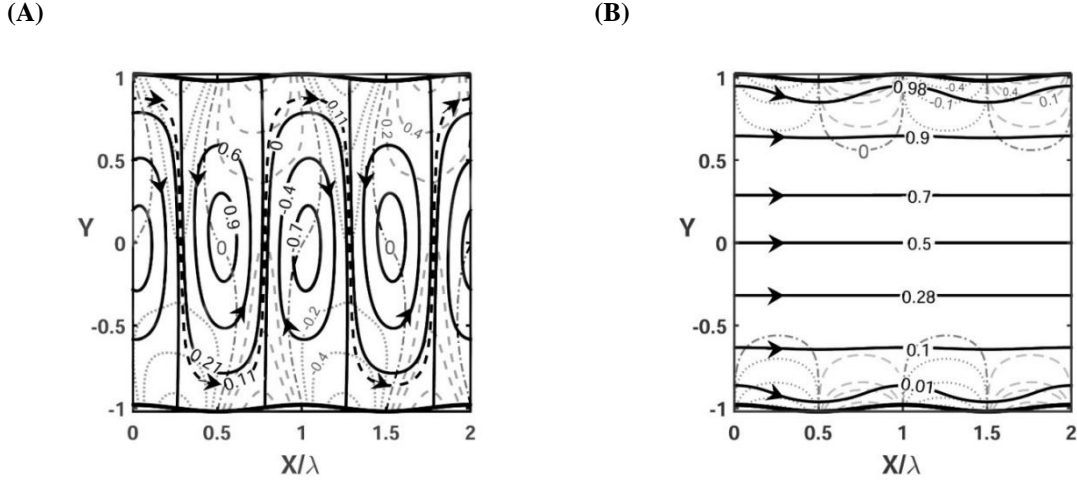
Figure 2.11: Flow and temperature fields for $Re = 1$, $Pr = 0.71$, $\Omega_{TL} = \pi/2$, $\Omega_{TU} = \pi/2$, $\Omega_C = 0$, $y_t = y_b = 0.02$, $Ra_{uni} = 0$, $Ra_{p,U} = Ra_{p,L} = 1000$ for $\alpha = 2$ (Fig.2.11A) and $\alpha = 15$ (Fig.2.11B). The solid lines identify streamlines and the dashed (dashed-dotted) lines identify the positive (negative) isotherms. Stream function has been normalized with its maximum values, i.e. $|\psi|_{max} = 6.45$ for $\alpha = 2$ and $|\psi|_{max} = 1.33$ for $\alpha = 15$. Temperature has been normalized with $\theta_{max} = 500$.

The changes of the boundary errors as functions of the Reynolds number are illustrated in Fig.2.12. The errors are insensitive to variations of Re as along as Re remains small enough, i.e. $Re < 5$. An increase of Re beyond this threshold leads to a significant error reduction but further increase to $Re > 100$ results in a slow increase of this error. The changes in the magnitude of the error are related to changes in the flow topology and the role of nonlinear terms in the momentum equation. The topology is quite complex for small Re (see Fig.2.13A) and this causes large absolute error. Increase of Re results in a simplified topology (see Fig.2.13B) and reduction of the absolute error. Further increase of Re leads to a still simpler topology (see Fig.2.13C) but increases the role of nonlinear terms resulting in an increase of the errors. The magnitude of these errors can be controlled by increasing the number of Fourier modes used in the computations, as demonstrated in Fig.2.12.
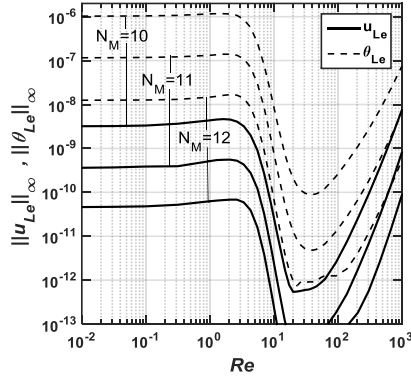
Figure 2.12: Variations of $\|u_{Le}\|_\infty$ and $\|\theta_{Le}\|_\infty$ as functions of the Reynolds number Re for $\alpha = 2$, $y_t = y_b = 0.02$, $Ra_{p,U} = Ra_{p,L} = 500$, $Ra_{uni} = 0$, $Pr = 0.71$, $\Omega_{TL} = \pi/2$, $\Omega_{TU} = \pi/2$, $\Omega_C = 0$, $N_T = 80$. Calculations have been carried out using different number of Fourier modes N_M.

(A)   **(B)**   **(C)**
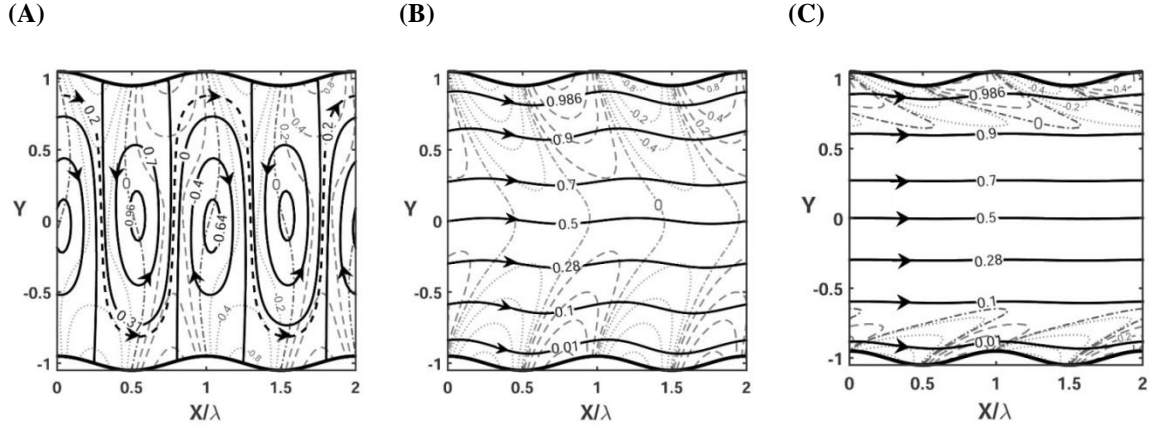
Figure 2.13: Flow and temperature fields for $\alpha = 2$, $Pr = 0.71$, $\Omega_{TL} = \pi/2$, $\Omega_{TU} = \pi/2$, $\Omega_C = 0$, $y_t = y_b = 0.05$, $Ra_{uni} = 0$, $Ra_{p,U} = Ra_{p,L} = 500$ for $Re = 1$ (Fig. 2.13A), $Re = 20$ (Fig. 2.13B) and $Re = 1000$ (Fig. 2.13C). Dashed (dashed-dotted) lines correspond to positive (negative) isotherms. The stream function has been normalized with $|\psi|_{max} = 4.24$ for $Re = 1$, with $|\psi|_{max} = 26.67$ for $Re = 20$, and with $|\psi|_{max} = 1333.33$ for $Re = 1000$. Temperature has been normalized with $\theta_{max} = 250$.

Variations of the boundary errors as functions of Rayleigh numbers are illustrated in Fig.2.14. The errors remain at the machine level for small enough $Ra_{p,U}$ and $Ra_{p,L}$ but begin to increase exponentially when the Rayleigh numbers becomes larger than ~300. This increase is associated with an increase of the strength of the nonlinear terms in the energy equation and increase of the complexity of the resulting flow and temperature fields as illustrated in Fig.2.15. The magnitude of the error can be reduced through the use of more Fourier modes as shown in Fig.2.14. The role of Ra_{uni} is illustrated in

Fig.2.16. An increase of Ra_{uni} increases the intensity of the natural convection component and, thus, increases the importance of the nonlinear terms in the energy equation and increases the complexity of the velocity and temperature fields as illustrated in Fig.2.17. Negative values of Ra_{uni} reduce the intensity of convection and reduce the complexity of the velocity and temperature fields and, as a result, the magnitude of the error decreases.
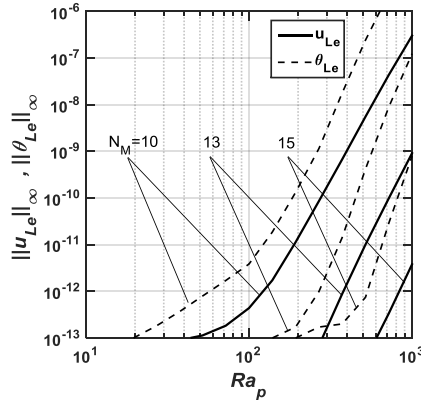
Figure 2.14: Variations of $\|u_{Le}\|_\infty$ and $\|\theta_{Le}\|_\infty$ as a function of the Rayleigh number $Ra_{p,U} = Ra_{p,L} = Ra_p$ for $\alpha = 2$, $y_t = y_b = 0.02$, $Ra_{uni} = 0$, $Re = 1$, $Pr = 0.71$, $\Omega_{TL} = \pi/2$, $\Omega_{TU} = \pi/2$, $\Omega_C = 0$, $N_T = 80$. Calculations have been carried out using different number of Fourier modes N_M.
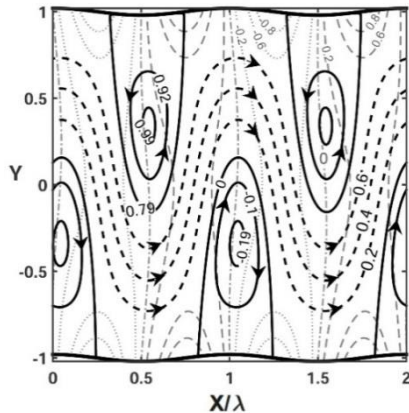
(A)   **(B)**
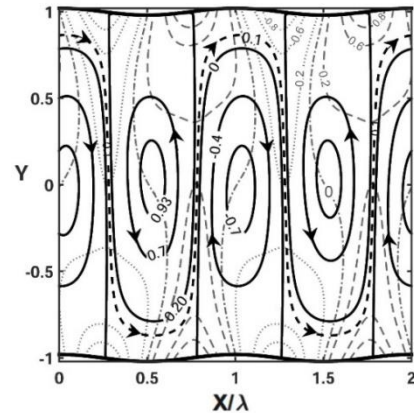
Figure 2.15: Flow and temperature fields for $\alpha = 2$, Re =1, $Pr = 0.71$, $\Omega_{TL} = \pi/2$, $\Omega_{TU} = \pi/2$, $\Omega_C = 0$, $y_t = y_b = 0.02$, $Ra_{uni} = 0$ for $Ra_{p,U} = Ra_{p,L} = 100$ (Fig. 2.15A) for $Ra_{p,U} = Ra_{p,L} = 1000$ (Fig. 2.15B). The stream function and temperature have been normalized with $|\psi|_{max} = 1.68$ and $\theta_{max} = 50$ for $Ra_{p,U} = Ra_{p,L} = 100$, and with $|\psi|_{max} = 6.45$, and $\theta_{max} = 500$ for $Ra_{p,U} = Ra_{p,L} = 1000$. The dashed (dashed-dotted) lines correspond to the positive (negative) isotherms.
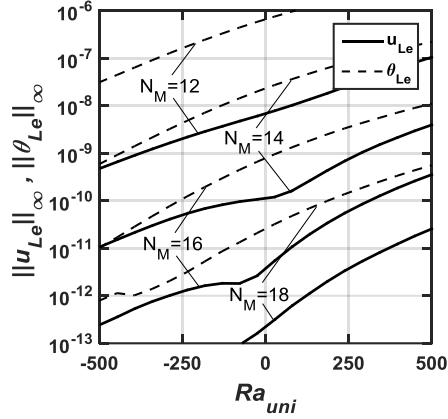
Figure 2.16: Variations of $\|u_{Le}\|_\infty$ and $\|\theta_{Le}\|_\infty$ as functions of the uniform Rayleigh number Ra_{uni} for $\alpha = 2$, $Ra_{p,U} = Ra_{p,L} = 1000$, $y_t = y_b = 0.02$, $Re = 1$, $Pr = 0.71$, $\Omega_{TL} = \pi/2, \Omega_{TU} = \pi/2, \Omega_C = 0, N_T = 80$.

(A)   **(B)**   **(C)**
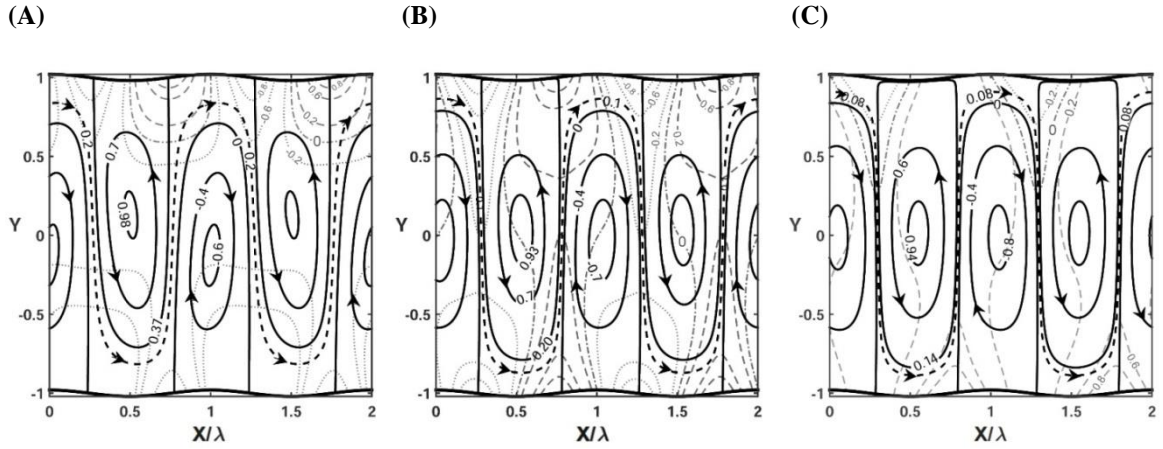
Figure 2.17: Flow and temperature fields for $\alpha = 2$, $Re = 1$, $Pr = 0.71$, $\Omega_{TL} = \pi/2$, $\Omega_{TU} = \pi/2$, $\Omega_C = 0$, $y_t = y_b = 0.02$, $Ra_{p,U} = Ra_{p,L} = 1000$ for $Ra_{uni} = -500$ (Fig.2.17A), $Ra_{uni} = 0$ (Fig.2.17B) and $Ra_{uni} = 500$ (Fig.2.17C). The stream function and temperature have been normalized with $|\psi|_{max} = 3.64$ and $\theta_{max} = 500$ for $Ra_{uni} = -500$, with $|\psi|_{max} = 6.45$ and $\theta_{max} = 500$ for $Ra_{uni} = 0$, and with $/\psi|_{max} = 9.59$ and $\theta_{max} = 750$ for $Ra_{uni} = 500$. The dashed (dashed-dotted) lines correspond to the positive (negative) isotherms.

2.8. Over-determined formulation

The formulation described in Section 2.3 uses the same number of Fourier modes for the field equations and for the boundary relations. We shall refer to this formulation as the "classical" formulation. Results presented in Section 2.7 demonstrate that increase of the complexity of the geometry results in an increase of the boundary errors. The reader may note that the algorithm relies on two types of Fourier expansions, one for the field variables and one for the boundary relations. The field equations are always the same regardless of the channel geometry and, thus, the convergence rates of the relevant Fourier expansions do not pose problems. On the other hand, the boundary relations directly account for the plate geometry and the rate of convergence of the relevant Fourier expansions decreases as the geometry becomes more extreme. This suggests the use of more Fourier terms for the boundary relations and, as a result, one ends up with an over-determined problem formulation (Husain et al. 2009).

We shall describe the over-determined formulation starting with the energy equation. As shown in Section 2.3 (see Eq.2.3.23), discretization of each boundary condition results in the construction of $2N_f + 1$ boundary relations. Formulation described in Section 2.3.1 uses the leading $2N_M + 1$ of these relations for each boundary condition. The overdetermined formulation uses $2N_{M,B} + 1$ of such relations, where $N_M \leq N_{M,B} \leq N_f$, resulting in $2(2N_{M,B} + 1)$ boundary relations for each modal function. The system reduces to the classical form for $N_{M,B} = N_M$.

The over-determined system can be written as

$$L_{3,0}T = R_{2,0}(V,T).$$ (2.8.1)

In the above, $L_{3,0}$ is the coefficient matrix of dimension $q \times p$ where $q = (N_T - 2)(2N_M + 1) + 2(2N_{M,B} + 1)$, $p = N_T(2N_M + 1)$, T is the vector of unknowns of dimension p and $R_{2,0}$ is the right hand side vector of dimension q. Figure 2.16a illustrates the structure of $L_{3,0}$ where all boundary relations have been placed at the

bottom of the matrix. Entries corresponding to the field equations are contained in $H_{3,O}$ which has a block-diagonal structure with each block of the size $(N_T - 2) \times N_T$. The boundary relations are contained in $K_{3,0}$ which has the size $r \times p$ where $r = 2\left(2N_{M,B} + 1\right)$, and has to be treated as a full matrix. System (2.8.1) can be solved only in the least square sense. The Singular Value Decomposition (SVD) method has been used in the present work. The solution can be written as

$$T = L_{3,O}^{+} R_{2,O}, \tag{2.8.2}$$

where $L_{3,O}^{+}$ represents the pseudoinverse of $L_{3,O}$ to be evaluated using the Singular Value Decomposition (SVD). If $L_{3,O}$ is a $m \times n$ matrix, the singular value theorem states that there exists a factorization of $L_{3,O}$, called SVD, of the form

$$L_{3,O} = UZW^{*}, \tag{2.8.3}$$

where U is a $m \times m$ unitary matrix, W is a $n \times n$ unitary matrix, W^{*} is the conjugate transpose of W and Z is a $m \times n$ matrix containing singular values of $L_{3,O}$ placed on the diagonal. Z and its pseudo-inverse Z^{+} have the form of

$$Z = \begin{pmatrix} Z_1 & 0 \\ 0 & 0 \end{pmatrix}, \quad Z^{+} = \begin{pmatrix} Z_1^{-1} & 0 \\ 0 & 0 \end{pmatrix}, \tag{2.8.4}$$

where $Z_1 = diag(\sigma_1, \sigma_2, \sigma_3, \dots, \sigma_h)$ are singular values of $L_{3,O}$ ordered in a descending order. The pseudo inverse of $L_{3,O}$ is of the form

$$L_{3,O}^{+} = WZ^{+}U^{*}, \tag{2.8.5}$$

A more accurate and more efficient solution is obtained by solving part of the system associated with the field equations exactly and part associated with the boundary relations in the least square sense (Husain & Floryan 2014). Construction of this solver begins with the extraction of the largest possible square matrix $A_{3,O}$ from $H_{3,O}$. This is done by

moving the unknown Chebyshev coefficients corresponding to the two lowest polynomials in each modal equation to the end of the vector of unknowns. The resulting matrix structure is illustrated in Fig.2.16B. The square matrix $\boldsymbol{A_{3,O}}$ of size $(q - r) \times (q - r)$ has a block diagonal structure with each block of size $(N_T - 2) \times (N_T - 2)$. The rectangular matrix $\boldsymbol{B_{3,O}}$ of size $(q - r) \times r$ also has a block diagonal form with blocks of size $(N_T - 2) \times 2$ whereas the full rectangular matrix $\boldsymbol{C_{3,O}}$ has size $r \times (q - r)$ and the full square matrix $\boldsymbol{D_{3,O}}$ has size $r \times r$. Matrices $\boldsymbol{B_{3,O}}$ and $\boldsymbol{D_{3,O}}$ contain coefficients corresponding to $\widehat{G\emptyset}_0^{(n)}$, $\widehat{G\emptyset}_1^{(n)}$ while information associated with the remaining coefficients is stored in matrices $\boldsymbol{A_{3,O}}$ and $\boldsymbol{C_{3,O}}$. The vector of unknowns consists of two parts with $\boldsymbol{T_1}$ containing $\widehat{G\emptyset}_k^{(n)}$ for $n \in \langle -N_M, N_M \rangle, k \in \langle 2, N_T - 1 \rangle$, and $\boldsymbol{T_2}$ containing $\widehat{G\emptyset}_k^{(n)}$ for $n \in \langle -N_M, N_M \rangle, k \in \langle 0,1 \rangle$. Equation (2.8.1) can now be written as

$$A_{3,O}T_1 + B_{3,O}T_2 = R_{21,O}, \quad C_{3,O}T_1 + D_{3,O}T_2 = R_{22,O}, \tag{2.8.6}$$

where $\boldsymbol{R_{21,O}}$ contains elements of $\boldsymbol{R_{2,O}}$ corresponding to $n \in \langle -N_M, N_M \rangle, k \in \langle 2, N_T - 1 \rangle$ and $\boldsymbol{R_{22,O}}$ contains elements of $\boldsymbol{R_{2,O}}$ corresponding to $n \in \langle -N_M, N_M \rangle, k \in \langle 0,1 \rangle$. The solution of (8.6) can be written in the form

$$T_2 = \left(D_{3,O} - C_{3,O}A_{3,O}^{-1}B_{3,O} \right)^+ \left[R_{22,O} - C_{3,O}A_{3,O}^{-1}R_{21,O} \right],$$
$$T_1 = A_{3,O}^{-1}\left[R_{21,O} - B_{3,O}T_2 \right], \tag{2.8.7}$$

One needs to store only the diagonal blocks of $\boldsymbol{A_{3,O}}$ and $\boldsymbol{B_{3,O}}$. Computational savings result from the construction of $\boldsymbol{A_{3,O}^{-1}}, \boldsymbol{C_{3,O}A_{3,O}^{-1}}, \boldsymbol{C_{3,O}A_{3,O}^{-1}B_{3,O}}, \boldsymbol{A_{3,O}^{-1}R_{21,O}}, \boldsymbol{A_{3,O}^{-1}B_{3,O}}$ block by block rather than working with the complete matrices.

(A)

(B)
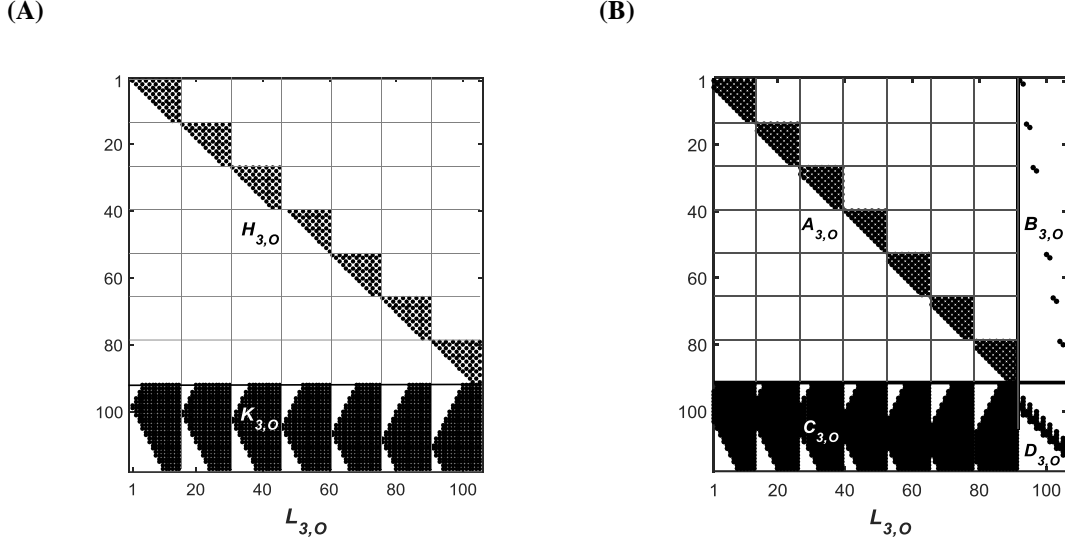
Figure 2.18: Structure of the coefficient matrix $L_{3,O}$ for the over-determined formulation for the energy equation with $N_T = 15$, $N_M = 3$, $N_{M,B} = 6$. Black dotes identifies the non-zero elements. Fig.2.18A displays the initial form of the matrix with all boundary relations placed at its bottom while Fig.2.18B shows the form after extractions of the largest diagonal matrix $A_{3,O}$ from $L_{3,O}$.

The solver for the momentum equation is constructed in a manner similar to the energy equation. The momentum equation can be written as

$$L_{1,O}V = -L_{2,O}T + R_{1,O}(V,T). \tag{2.8.8}$$

In the above, $L_{1,O}$ is the coefficient matrix of dimension $\acute{q} \times \acute{p}$ where $\acute{q} = (N_T - 4)(2N_M + 1) + 4(2N_{M,B} + 1)$, $\acute{p} = N_T(2N_M + 1)$, V is the vector of unknowns of dimension $\acute{p}$ and $[-L_{2,O}T + R_{1,O}]$ is the right-hand-side vector of dimension $\acute{q}$. Figure 2.17a illustrates the structure of $L_{1,O}$. Entries corresponding to the field equations are contained in $H_{1,O}$ which has a block-diagonal structure with each block of the size $(N_T - 4) \times N_T$. The boundary relations are contained in $K_{1,0}$ which has the size $\acute{r} \times \acute{p}$ where $r = 4(2N_{M,B} + 1)$, and has to be treated as the full matrix. System (2.8.8) can be solved similar to system (2.8.1), i.e.

$$V = L_{1,O}^+ (-L_{2,O}T + R_{1,O}), \tag{2.8.9}$$

where $L_{1,O}^+$ represents the pseudoinverse of $L_{1,O}$. Construction of the efficient solver begins with the extraction of the largest possible square matrix $A_{1,O}$ from $H_{1,O}$. This is

done by moving the unknown Chebyshev coefficients corresponding to the four lowest polynomials in each modal equation to the end of the vector of unknowns. The resulting matrix structure is shown in Fig.2.17b. The square matrix $\boldsymbol{A_{1,o}}$ of size $(\acute{q} - \acute{r}) \times (\acute{q} - \acute{r})$ has a block diagonal structure with each block of size $(N_T - 4) \times (N_T - 4)$. The rectangular matrix $\boldsymbol{B_{1,o}}$ of size $(\acute{q} - \acute{r}) \times \acute{r}$ also has a block diagonal form with blocks of size $(N_T - 4) \times 4$ whereas the full rectangular matrix $\boldsymbol{C_{1,o}}$ has size $\acute{r} \times (\acute{q} - \acute{r})$ and the full square matrix $\boldsymbol{D_{1,o}}$ has size $\acute{r} \times \acute{r}$. Matrices $\boldsymbol{B_{1,o}}$ and $\boldsymbol{D_{1,o}}$ contain coefficients corresponding to $\widehat{G\emptyset}_0^{(n)}$, $\widehat{G\emptyset}_1^{(n)}$, $\widehat{G\emptyset}_2^{(n)}$, $\widehat{G\emptyset}_3^{(n)}$ while information associated with the remaining coefficients is stored in matrices $\boldsymbol{A_{1,o}}$ and $\boldsymbol{C_{1,o}}$. The vector of unknowns consists of two parts with $\boldsymbol{T_1}$ containing $\widehat{G\emptyset}_k^{(n)}$ for $n \in \langle -N_M, N_M \rangle, k \in \langle 4, N_T - 1 \rangle$ and $\boldsymbol{T_2}$ containing $\widehat{G\emptyset}_k^{(n)}$ for $n \in \langle -N_M, N_M \rangle, k \in \langle 0,3 \rangle$. Equation (2.8.9) can now be written as

$$A_{1,o}T_1 + B_{1,o}T_2 = R_{11,o}, \quad C_{1,o}T_1 + D_{1,o}T_2 = R_{12,o}, \tag{2.8.10}$$

where $\boldsymbol{R_{11,o}}$ contains elements of $\left(-\boldsymbol{L_{2,o}}T + \boldsymbol{R_{1,o}} \right)$ corresponding to $n \in \langle -N_M, N_M \rangle, k \in \langle 4, N_T - 1 \rangle$ and $\boldsymbol{R_{12,o}}$ contains elements of $\left(-\boldsymbol{L_{2,o}}T + \boldsymbol{R_{1,o}} \right)$ corresponding to $n \in \langle -N_M, N_M \rangle, k \in \langle 0,3 \rangle$. The solution of (2.8.10) can be written in the form

$$T_2 = \left(D_{1,o} - C_{1,o}A_{1,o}^{-1}B_{1,o} \right)^+ \left[R_{12,o} - C_{1,o}A_{1,o}^{-1}R_{11,o} \right],$$
$$T_1 = A_{1,o}^{-1} \left[R_{11,o} - B_{1,o}T_2 \right], \tag{2.8.11}$$

One needs to store only the diagonal blocks of matrices $\boldsymbol{A_{1,o}}$ and $\boldsymbol{B_{1,o}}$. Computational savings result from the construction of $\boldsymbol{A_{1,o}^{-1}}, \boldsymbol{C_{1,o}A_{1,o}^{-1}}, \boldsymbol{C_{1,o}A_{1,o}^{-1}B_{1,o}}, \boldsymbol{A_{1,o}^{-1}R_{11,o}}, \boldsymbol{A_{1,o}^{-1}B_{1,o}}$ block by block rather than working with complete matrices.

(A)   **(B)**
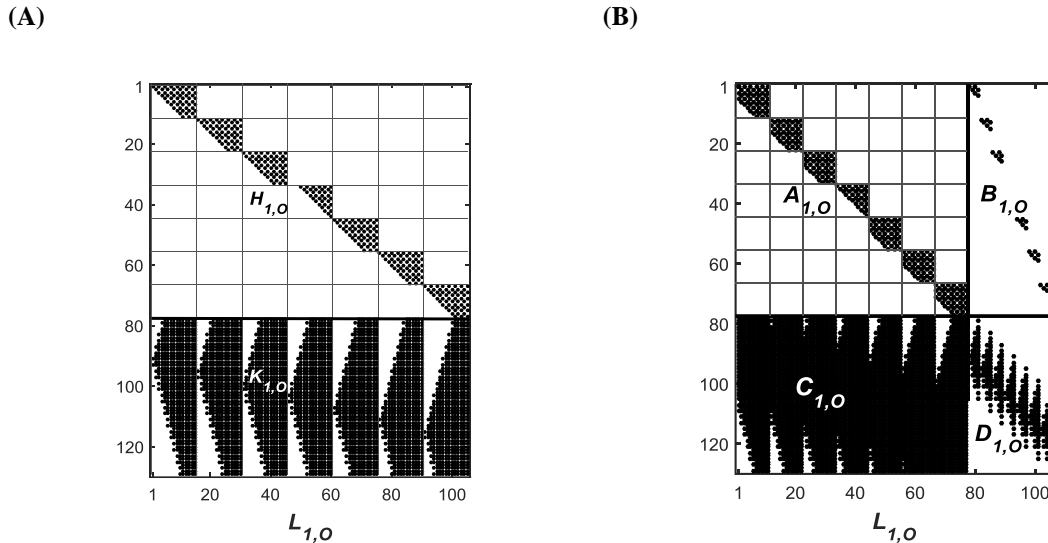
Figure 2.19: Structure of the coefficient matrix $L_{1,0}$ for the over-determined formulation for the momentum equation with $N_T = 15$, $N_M = 3$, and $N_{M,B} = 6$. Black dotes identifies the non-zero elements. Fig. 2.19A displays the initial form of the matrix after placing all boundary relations at its bottom while Fig. 2.19B shows its form after extractions of the largest diagonal matrix $A_{1,0}$ from $L_{1,0}$.

Figure 2.20 displays the Fourier spectra of boundary errors $u_{Le}{}^{(n)}$ and $\theta_{Le}{}^{(n)}$ for the same condition as in Fig.2.8. The errors are distributed over several Fourier modes including modes with $n < N_M$ which is consistent with the least square solution method. Results presented in Fig.2.21A demonstrate that the errors of the over-determined method increase as the Rayleigh number increases but, at the same time, the error for the velocity field is always smaller by an order of magnitude than the error for the classical formulation while the error of the temperature field remains the same as in the classical formulation. Results displayed in Fig.2.21B demonstrate that the errors increase as the groove amplitude increases but, at the same time, the error of the overdetermined formulation for the velocity field remains by an order of magnitude smaller than the error for the classical formulation. This extends the applicability of the IBC method to amplitudes by about 40% larger than those for which the classical formulation provides an acceptable accuracy. Use of the overdetermined formulation reduces the temperature error by a factor of ~2 for large enough groove amplitudes.

Data presented in Fig.2.21 demonstrate that the error decreases when the number of additional Fourier modes used in the boundary relations increases. There is however a

limit to this decrease as any further increase in the number of Fourier modes does not affect these errors. The number of Fourier modes that produces the largest error decrease is referred to as the optimum number and it is approximately equal to half of N_M. Use of an excessively large number of Fourier modes is counterproductive as it does not improve the accuracy of the results.

Results presented in Fig.2.21 suggest that the use of the overdetermined formulation for the temperature boundary conditions is not recommended. Data presented in Fig.2.22 have been obtained using the classical formulation of the temperature boundary conditions and the overdetermined formulation of the velocity boundary conditions. The error distributions displayed in Figs 2.21 and 2.22 are nearly identical. Elimination of the overdetermined formulation for the temperature reduces size of matrix $\boldsymbol{C}_{1,0}$ in Fig.2.19 resulting in a more efficient computing.

(A)   (B)
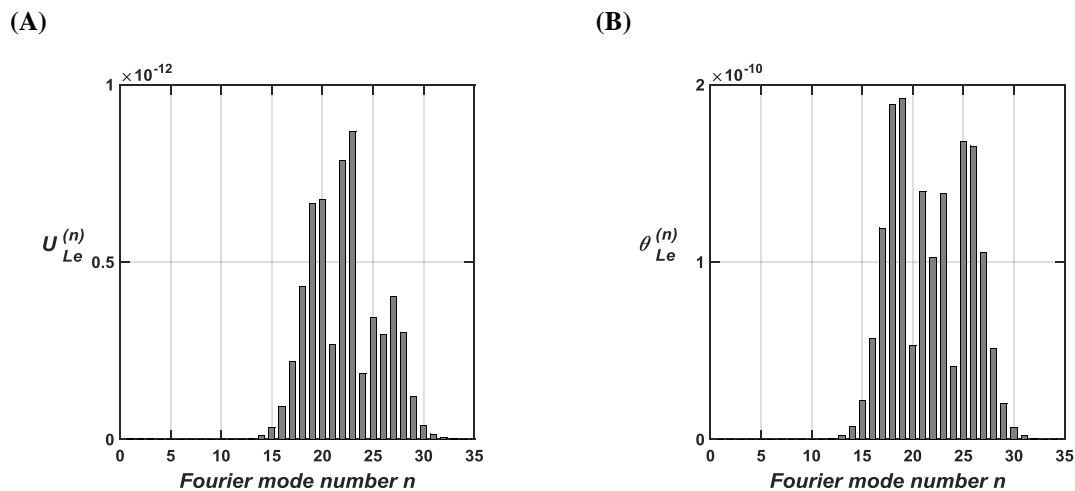
Figure 2.20: Fourier spectra of the error in the enforcement of the boundary conditions along the lower plate for $\alpha = 5$, $y_t = y_b = 0.05$, $Ra_{p,U} = Ra_{p,L} = 500$, $Ra_{uni} = 0$, $Pr = 0.71$, $Re = 5$, $\Omega_{TL} = 0$, $\Omega_{TU} = 0$, $\Omega_C = 0$, $N_T = 50$. This test has been carried out using the overdetermined method with $N_M = 20$ Fourier modes for field equations and $N_{M,B} = 30$ Fourier modes for the boundary relations.
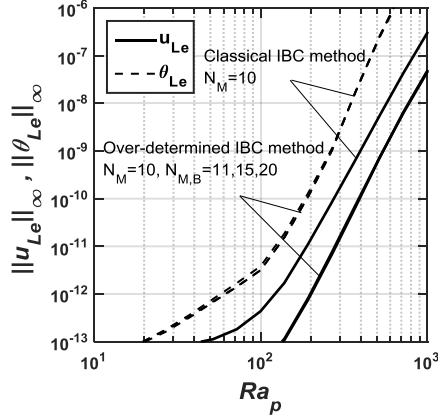
(A)   **(B)**
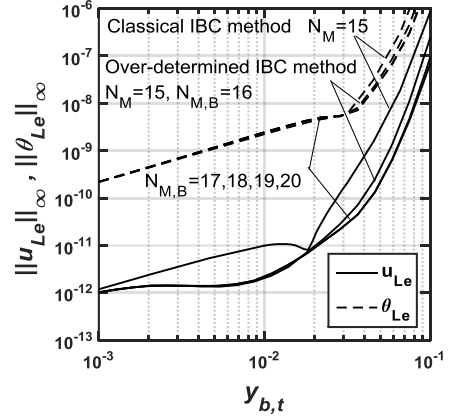
Figure 2.21: Variations of $\|u_{Le}\|_\infty$ and $\|\theta_{Le}\|_\infty$ as functions of the Rayleigh number $Ra_p = Ra_{p,U} = Ra_{p,L}$ for $y_t = y_b = 0.02$ (Fig.2.21A) and as functions of the amplitude $y_{b,t} = y_t = y_b$ for $Ra_{p,U} = Ra_{p,L} = 1000$ (Fig.2.21B). All results have been obtained for $\alpha = 2$, $Re = 1, Ra_{uni} = 0$, $Pr = 0.71$, $\Omega_{TL} = \pi/2$, $\Omega_{TU} = \pi/2$, $\Omega_C = 0$, $N_T = 80$ using the overdetermined method.
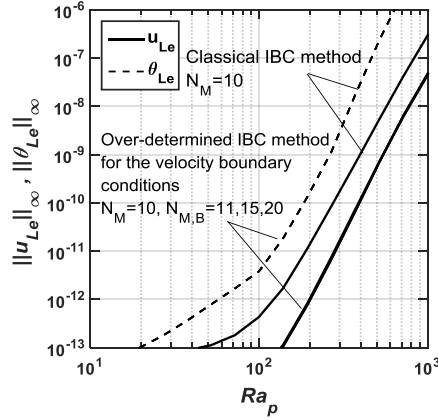
(A)   **(B)**
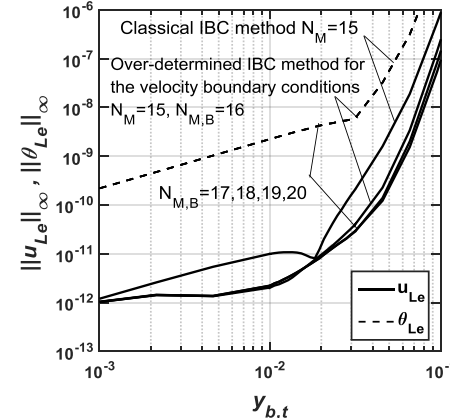
Figure 2.22: Variations of $\|u_{Le}\|_\infty$ and $\|\theta_{Le}\|_\infty$ as functions of the Rayleigh number $Ra_p = Ra_{p,U} = Ra_{p,L}$ for $y_t = y_b = 0.02$ (Fig.2.22A) and as functions of the amplitude $y_{b,t} = y_t = y_b$ for $Ra_{p,U} = Ra_{p,L} = 1000$ (Fig.2.22B). All results have been obtained for $\alpha = 2$, $Re = 1, Ra_{uni} = 0$, $Pr = 0.71$, $\Omega_{TL} = \pi/2$, $\Omega_{TU} = \pi/2$, $\Omega_C = 0$, $N_T = 80$ using the overdetermined method only for the velocity boundary conditions.

2.9. Summary

A gridless, spectrally accurate algorithm for analysis of convection problems in corrugated conduits has been developed. Boussinesq model has used to describe fluid properties. Field equations are expressed with Fourier expansions in stream-wise direction and Chebyshev expansions in the transverse direction with the gravity directed across the conduit. The geometric non-uniformities are treated by placing the corrugated conduit inside this domain and expressing the physical boundary conditions as constraints, i.e. using the Immersed Boundary Conditions (IBC) method. Several steps were taken to improve the efficiency of the algorithm. Numerous tests confirm the spectral accuracy of the solution. The algorithm is suitable for problems involving geometry optimization.

Application of this algorithm to analysis of natural convection in a corrugated slot is described in the next Chapter.

Chapter 3

Natural convection in a corrugated slot

3.1. Introduction

This Chapter presents analysis of the natural convection in a slot formed by two isothermal horizontal corrugated plates and is aimed at the identification of the fundamental features of convection resulting from the presence of geometric non-uniformities. The analysis relies on the algorithm described in Chapter 2 simplified by setting, $Re = 0$, $Ra_{pL} = 0$, $Ra_{pU} = 0$. The schematic diagram of the flow system is shown in Fig 3.1. Section 3.2 describes the model problem which represent a simplified version of the general model problem discussed in Section 2.2. The pressure gradient constraint (3.2.6c) is used instead of the flow rate constraint (2.2.9) as it better represents conditions found in the case of natural convection. Section 3.3 discusses convection resulting from corrugations placed at the lower plate; Section 3.3.1 discusses convection associated with the long wavelength corrugations while Section 3.3.2 deals with convection associated with corrugations of arbitrary wavelengths. Section 3.4 describes convection resulting from placing corrugation at the upper plate. Section 3.5 is devoted to description of convection when both plates are corrugated; Section 3.5.1 discusses the role of the long wavelength corrugations while Section 3.5.2 describes convection associated with corrugations of arbitrary wavelengths. All results presented in Sections 3.3, 3.4 and 3.5 have been determined for the Prandtl number $Pr = 0.71$. Section 3.6 extends the analysis to arbitrary Prandtl numbers. Section 3.7 provides a short summary of the main conclusions.

3.2. Problem Formulation

Consider fluid contained in a slot formed by two horizontal corrugated plates (see Fig.3.1) with geometries specified at Eq. 2.2.1.
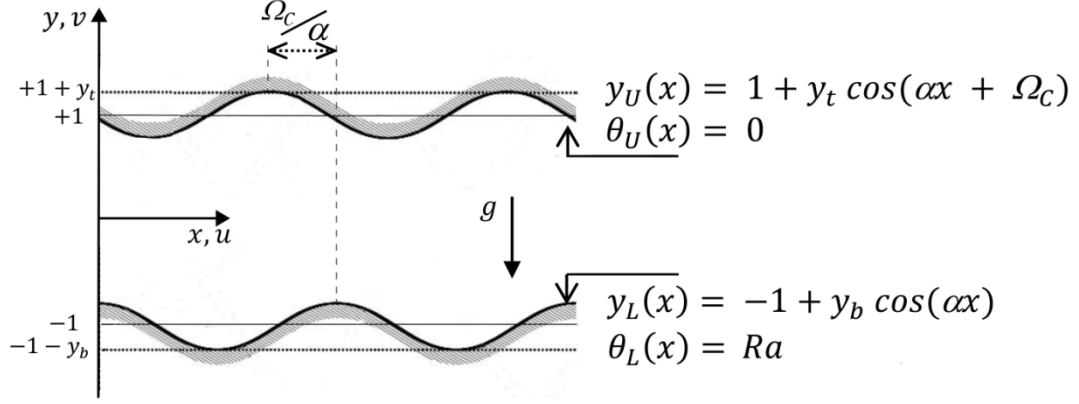
Figure 3.2: Schematic diagram of the flow system.

We define the relative temperature as $\theta^* = T^* - T_U^*$ which leads to the thermal boundary conditions of the form

$$\theta_L^*(y_L^*) = \theta_S^*, \quad \theta_U^*(y_U^*) = 0 \qquad (3.2.1\text{a,b})$$

where $\theta_S^* = T_L^* - T_U^*$. Use of the half of the mean distance between the plates h^* as the length scale and $\kappa^* v^* / (g^* \Gamma^* h^{*3})$ as the temperature scale result in the following expressions for the temperatures

$$\theta_L(y_L) = Ra, \quad \theta_U(y_U) = 0 \qquad (3.2.2\text{a,b})$$

where $Ra = g^* \Gamma^* h^{*3} \theta_S^* / (\kappa^* v^*)$ is the Rayleigh number measuring the intensity of the heating. The field equations have the same forms as Eq. 2.2.6.

There is no externally imposed horizontal pressure gradient and this condition can be expressed as

$$\left. \frac{\partial p}{\partial x} \right|_{mean} = 0. \qquad (3.2.3)$$

The pressure field is normalized in such a way that $p(0,0) = C$ where C is an arbitrary constant. Details of this spectrally accurate algorithm can be found in Chapter 2. (Husain & Floryan 2010; Abtahi et al. 2016).

3.2.1. Evaluation of stresses

Analysis of the system dynamics requires evaluation of forces acting on the plates. Stress vector $\vec{\sigma}_L$ acting on the lower plate can be expressed as

$$\vec{\sigma}_L = [\sigma_{x,L}, \quad \sigma_{y,L}] = [n_{x,L} \quad , n_{y,L}] \begin{bmatrix} \tau_{xx} + p & \tau_{xy} \\ \tau_{yx} & \tau_{yy} + p \end{bmatrix}_{y_L},$$

(3.2.4)

where

$$\tau_{xx} = -2\frac{\partial u}{\partial x}, \quad \tau_{xy} = \tau_{yx} = -\frac{\partial u}{\partial y} - \frac{\partial v}{\partial x}, \quad \tau_{yy} = -2\frac{\partial v}{\partial y}$$

(3.2.5a,b,c)

are the components of the shear tensor and

$$[n_{x,L}, n_{y,L}] = N_L[-\alpha y_b \sin(\alpha x), -1]$$

(3.2.6)

stands for the normal unit vector pointing outwards with $N_L = \{1 + [\alpha y_b \sin(\alpha x)]^2\}^{-1/2}$. The x- and y-components of the stress vector have the following forms

$$\sigma_{x,L} = \sigma_{xv,L} + \sigma_{xp,L} = N_L \left[2\alpha y_b \sin(\alpha x) \frac{\partial u}{\partial x}\Big|_{y_L} + (\frac{\partial u}{\partial y} + \frac{\partial v}{\partial x})\Big|_{y_L} \right] -$$

(3.2.7a)

$$N_L \alpha y_b \sin(\alpha x) p|_{y_L},$$

$$\sigma_{y,L} = \sigma_{yv,L} + \sigma_{yp,L} = N_L \left[\alpha y_b \sin(\alpha x) \left(\frac{\partial u}{\partial y} + \frac{\partial v}{\partial x}\right)\Big|_{y_L} + 2\frac{\partial v}{\partial y}\Big|_{y_L} \right] - N_L p|_{y_L},$$

(3.2.7b)

where $(\sigma_{xv,L}, \sigma_{yv,L})$ and $(\sigma_{xp,L}, \sigma_{yp,L})$ denote viscous and pressure contributions, respectively. The normal $\sigma_{n,L}$ and tangential $\sigma_{t,L}$ components can be expressed as

$$\sigma_{n,L} = \sigma_{nv,L} + \sigma_{np,L} = \tag{3.2.7c}$$

$$N_L{}^2 \left[-2\alpha^2 y_b{}^2 \sin^2(\alpha x) \frac{\partial u}{\partial x}\Big|_{y_L} - \right.$$

$$\left. 2\alpha y_b \sin(\alpha x) \left(\frac{\partial u}{\partial y} + \frac{\partial v}{\partial x}\right)\Big|_{y_L} - 2\frac{\partial v}{\partial y}\Big|_{y_L} \right] + p|_{y_L},$$

$$\sigma_{t,L} = N_L{}^2 \left\{ 2\alpha y_b \sin(\alpha x) \left(\frac{\partial u}{\partial x} - \frac{\partial v}{\partial y}\right)\Big|_{y_L} + [1 - \alpha^2 y_b{}^2 \sin^2(\alpha x)] \left(\frac{\partial u}{\partial y} + \right. \right. \tag{3.2.7d}$$

$$\left. \left. \frac{\partial v}{\partial x}\right)\Big|_{y_L} \right\},$$

where $\sigma_{nv,L}$ and $\sigma_{np,L}$ denote viscous and pressure contributions to the normal component, respectively.

3.2.2. Evaluation of heat transfer

The heat transfer characteristics are expressed in terms of the local Nusselt number $Nu_{loc,L}$ defined as

$$Nu_{loc,L} = \vec{\boldsymbol{n}}_L \cdot \vec{\boldsymbol{q}}_L = n_{x,L} q_{x,L} + n_{y,L} q_{y,L} \tag{3.2.8}$$

where $\vec{\boldsymbol{q}}_L = [q_{x,L}, q_{y,L}] = \left[\frac{\partial \theta}{\partial x}, \frac{\partial \theta}{\partial y}\right]_{y_L}$ stands for the temperature gradient at the plate. The net heat flux leaving the plate is expressed in terms of the mean Nusselt number $Nu_{av,L}$ defined as

$$Nu_{av} = \lambda^{-1} \int_0^\lambda Nu_{loc,L} N_L^{-1} dx. \tag{3.2.9}$$

Similar relations can be developed for the upper plate and the relevant quantities are identified using subscript U. The reader may note that $N_U = \{1 + [\alpha y_t \sin(\alpha x + \Omega_c)]^2\}^{-\frac{1}{2}}$ in this case.

The reader may note that convection does not occur in the absence of the heating, i.e. (u, v, θ) $\rightarrow$ 0, $p \rightarrow C$, $\sigma_{xv,L} \rightarrow 0, \sigma_{xp,L} \rightarrow -N_L \alpha y_b \sin(\alpha x)C$, $\sigma_{yv,L} \rightarrow 0, \sigma_{yp,L} \rightarrow -N_L C$ when $Ra \rightarrow 0$. Similarly, convection does not occur in a smooth heated slot, i.e. (u, v) $\rightarrow$ 0, $\theta \rightarrow \frac{Ra}{2}(1-y)$, $p \rightarrow \frac{Ra}{2Pr}\left(-\frac{y^2}{2}+y\right)+C$, $\sigma_{xv,L} \rightarrow 0, \sigma_{xp,L} \rightarrow 0$, $\sigma_{yv,L} \rightarrow 0, \sigma_{yp,L} \rightarrow -\frac{3Ra}{4Pr}+C$ when (y_b, y_t) $\rightarrow$ 0.

It is convenient for interpretation purposes to define the conduction problem in a slot displayed in Fig.3.1, i.e.

$$\nabla^2 \theta_{cond}=0, \ \theta_{cond,L}(y_L) = Ra, \quad \theta_{cond,U}(y_U) = 0 \tag{3.2.10}$$

which can be solved using an algorithm adapted from Szumbarski & Floryan (1999). One can also define the conductive Nusselt numbers of the form

$$Nu_{cond,loc,L} = \vec{\boldsymbol{n}}_L \cdot \vec{\boldsymbol{q}}_{c,L} = n_{x,L} \left.\frac{\partial \theta_c}{\partial x}\right|_L + n_{y,L} \left.\frac{\partial \theta_c}{\partial y}\right|_L , \tag{3.2.11}$$

$$Nu_{cond,av} = \lambda^{-1} \int_0^\lambda Nu_{cond,loc,L} N_L^{-1} dx.$$

3.3. Convection driven by corrugation placed at the lower plate

A typical pattern of motion resulting from the heating is illustrated in Fig.3.2. The conductive temperature field in the absence of corrugation is uniform in the x-direction and the fluid movement may occur only if the vertical temperature gradient meets critical conditions (Chandrasekhar 1961). Presence of corrugation generates horizontal conductive temperature gradients which lead to the formation of horizontal and vertical pressure gradients which drive the motion. The fluid moves upwards above the corrugation peaks and downwards above the corrugation troughs resulting in the formation of counter rotating horizontal rolls. The topologies of the pressure field at the top and bottom of the slot are different due to the presence of static component as documented by plots of the pressure field with the mode zero $p^{(0)}(y)$ removed displayed in Fig.3.2B. The motion occurs regardless of the intensity of the heating and its

characteristics are determined by the corrugation geometry. The convective motion amplifies the horizontal temperature gradients increasing the convection-driving force until a saturation state is reached where the driving force is balance by the flow resistance. We shall now focus on the detailed description of this motion starting with long wavelength corrugations.

(A)   (B)
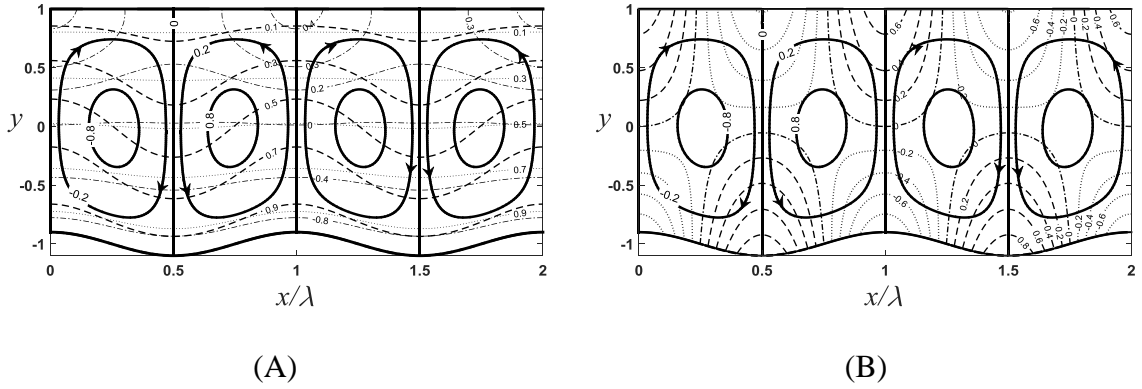
Figure 3.2: The flow topology and the temperature and pressure fields in a slot with $\alpha = 1.53$, $Ra = 200$, $y_b = 0.1$ normalized with their maxima (Fig.3.2A). The solid, dashed, dashed-dotted and dotted lines identify streamlines, isotherms of the complete temperature field, lines of constant pressure and isotherms of the conductive temperature field, respectively. The maxima of the stream function and the temperature, pressure and conduction temperature fields are $|\psi|_{max} = 1.145$, $|\theta|_{max} = 200$, $|p|_{max} = 213.7$, $|\theta_{cond}|_{max} = 200$, respectively. The pressure constant C has been set zero. Pressure field with mode zero eliminated is displayed in Fig.3.2B together with streamlines; dashed and dotted lines identify positive and negative values, while dashed dotted line identifies zeros. This pressure field is normalized with its maximum $|p|_{max} = 24.67$.

3.3.1. Long-wavelength corrugation

Consider the limit $\alpha \to 0$. The solution process begins with domain transformation of the form

$$\xi = \alpha x, \quad \eta = 2\frac{y-1}{2-y_b \cos \xi} + 1,$$

(3.3.1a,b)

where ξ is a slow scale and η maps the corrugated slot into a regular strip $\eta \in$ [-1,1]. The field equations expressed in the (ξ, η)-coordinates take the form of

$$\alpha \frac{\partial u}{\partial \xi} + F_7 \frac{\partial u}{\partial \eta} + F_8 \frac{\partial v}{\partial \eta} = 0, \tag{3.3.2a}$$

$$\frac{\partial^2 u}{\partial \eta^2} + [F_1 - F_2 u - F_3 v]\frac{\partial u}{\partial \eta} + F_4 \frac{\partial^2 u}{\partial \xi \partial \eta} + F_5 \frac{\partial^2 u}{\partial \xi^2} - F_6 u \frac{\partial u}{\partial \xi} - F_6 \frac{\partial p}{\partial \xi} - F_2 \frac{\partial p}{\partial \eta} = 0, \tag{3.3.2b}$$

$$\frac{\partial^2 v}{\partial \eta^2} + [F_1 - F_2 u - F_3 v]\frac{\partial v}{\partial \eta} + F_4 \frac{\partial^2 v}{\partial \xi \partial \eta} + F_5 \frac{\partial^2 v}{\partial \xi^2} - F_6 u \frac{\partial v}{\partial \xi} - F_3 \frac{\partial p}{\partial \eta} + Pr^{-1}F_9 \theta = 0, \tag{3.3.2c}$$

$$\frac{\partial^2 \theta}{\partial \eta^2} + [F_1 - PrF_2 u - PrF_3 v]\frac{\partial \theta}{\partial \eta} + F_4 \frac{\partial^2 \theta}{\partial \xi \partial \eta} + F_5 \frac{\partial^2 \theta}{\partial \xi^2} - PrF_6 u \frac{\partial \theta}{\partial \xi} = 0, \tag{3.3.2d}$$

where the coefficients $F_1, \ldots, F_6$ are defined in Appendix B. The form of the conduction problem (3.2.16) is not given but its solution can be obtained in a similar manner. The boundary conditions assume the following form

$$u(\xi, \pm 1) = 0, \quad v(\xi, \pm 1) = 0, \quad \theta(\xi, -1) = Ra, \quad \theta(\xi, 1) = 0. \tag{3.3.3}$$

The unknowns are represented as power expansions in terms of α, i.e.

$$[u, v, \theta, \theta_c] = [u_0, v_0, \theta_0, \theta_{c0}] + \alpha[u_1, v_1, \theta_1, \theta_{c1}] + \alpha^2[u_2, v_2, \theta_2, \theta_{c2}] + \tag{3.3.4a}$$
$$O(\alpha^3),$$
$$p = \alpha^{-1}p_{-1} + p_0 + \alpha p_1 + O(\alpha^2), \tag{3.3.4b}$$

these expansions are substituted into (3.3.2) - (3.3.3) and the leading-order terms are extracted resulting in a system of the form

$$\frac{\partial v_0}{\partial \eta} = 0, \quad \frac{\partial^2 u_0}{\partial \eta^2} - \frac{G}{2}v_0 \frac{\partial u_0}{\partial \eta} - \frac{1}{4}G^2 \frac{\partial p_{-1}}{\partial \xi} + \frac{1}{4}y_b G(\eta - 1)\sin\xi \frac{\partial p_{-1}}{\partial \eta} = 0, \tag{3.3.5a,b}$$

$$\frac{\partial p_{-1}}{\partial \eta} = 0, \quad \frac{\partial^2 \theta_0}{\partial \eta^2} - Pr\frac{G}{2}v_0 \frac{\partial \theta_0}{\partial \eta} = 0, \tag{3.3.5c,d}$$

$$u_0(\xi, \pm 1) = 0, \ v_0(\xi, \pm 1) = 0, \ \theta_0(\xi, -1) = Ra, \ \theta_0(\xi, 1) = 0, \left.\frac{\partial P_{-1}}{\partial \xi}\right|_{mean} = 0, \tag{3.3.3.5e}$$

whose solution can be expressed as

$$u_0 = 0, \qquad v_0 = 0, \qquad \theta_0 = \theta_{c0} = \frac{Ra}{2}(1 - \eta), \qquad p_{-1} = 0. \tag{3.3.6}$$

The next order system, i.e. system $0(\alpha^1)$, has the form of

$$\frac{\partial v_1}{\partial \eta} = 0, \quad \frac{\partial^2 u_1}{\partial \eta^2} - \frac{1}{4}G^2\frac{\partial p_0}{\partial \xi} + \frac{y_b\,G\sin\xi}{4}(\eta - 1)\frac{\partial p_0}{\partial \eta} = 0, \qquad\qquad (3.3.7\text{a,b})$$

$$-\frac{G}{2}\frac{\partial p_0}{\partial \eta} + \frac{G^2}{4Pr}\theta_0 = 0, \qquad \frac{\partial^2\theta_1}{\partial \eta^2} - \frac{Pr\,G}{2}v_1\frac{\partial\theta_0}{\partial \eta} = 0, \qquad\qquad (3.3.7\text{c,d})$$

$$u_1(\xi,\pm 1) = 0, \quad v_1(\xi,\pm 1) = 0, \quad \theta_1(\xi,\pm 1) = 0, \quad \left.\frac{\partial P_0}{\partial \xi}\right|_{mean} = 0, \qquad (3.3.7\text{e})$$

whose solution can be easily found, i.e.

$$u_1 = \frac{y_b\,Ra}{7680\,Pr}\,(5\eta^4 - 20\eta^3 - 6\eta^2 + 20\eta + 1)\big[(y_b^2 + 16)\sin\xi - 8y_b\sin(2\xi) + \qquad\qquad (3.3.8)$$

$$y_b^2\sin(3\xi)\big]\,, \quad v_1 = 0,$$

$$p_0 = \frac{Ra}{80Pr}\Big\{-20\eta^2 + 40\eta - 2y_b + \frac{10y_b^2}{(2-y_b)} - y_b(-10\eta^2 + 20\eta - 22)\cos\xi\Big\} + C,$$

$$\theta_1 = 0, \theta_{c1} = 0\,.$$

System $0(\alpha^2)$ has the form

$$\frac{\partial v_2}{\partial \eta} - \frac{y_b\sin\xi}{2}(\eta - 1)\frac{\partial u_1}{\partial \eta} + \frac{G}{2}\frac{\partial u_1}{\partial \xi} = 0, \quad \frac{\partial^2 u_2}{\partial \eta^2} - \frac{1}{4}G^2\frac{\partial p_1}{\partial \xi} + \frac{y_b\,G\sin\xi}{4}(\eta - 1)\frac{\partial p_1}{\partial \eta} = 0, \qquad (3.3.9\text{a,b})$$

$$-\frac{G}{2}\frac{\partial p_1}{\partial \eta} + \frac{G^2}{4Pr}\theta_1 = 0, \qquad\qquad (3.3.9\text{c})$$

$$\frac{\partial^2\theta_2}{\partial \eta^2} + \frac{2y_b^2\sin^2\xi - y_b G\cos\xi}{4}(\eta - 1)\frac{\partial\theta_0}{\partial \eta} + \frac{Pr\,y_b\,G\sin\xi}{4}(\eta - 1)u_1\frac{\partial\theta_0}{\partial \eta} - \frac{Pr\,G}{2}v_2\frac{\partial\theta_0}{\partial \eta} = 0, \qquad (3.3.9\text{d})$$

$$u_2(\xi,\pm 1) = 0, \quad v_2(\xi,\pm 1) = 0, \quad \theta_2(\xi,\pm 1) = 0, \quad \left.\frac{\partial P_1}{\partial \xi}\right|_{mean} = 0. \qquad (3.3.9\text{e})$$

Its solution can be written as

$$u_2 = 0, \quad v_2 = \frac{y_b\,Ra}{30720\,Pr}\,[k_1\cos\xi + k_2\cos(2\xi) + k_3\cos(3\xi) + k_4\cos(4\xi) + k_5],$$

$$p_1 = 0,$$

$$\theta_2 = \frac{y_b\,Ra}{12902400}\,[(Ra\,k_6 + k_7)\cos\xi + (Ra\,k_8 + k_9)\cos(2\xi) + Ra\,k_{10}\cos(3\xi) + $$

$$Ra\,k_{11}\cos(4\xi) + Ra\,k_{12}\cos(5\xi) + (Ra\,k_{13} + k_{14})]\,,$$

$$\theta_{c2} = \frac{y_b Ra}{48}(\eta^3 - 3\eta^2 - \eta + 3)\Big[-2\cos\xi - \frac{1}{2}y_b\cos(2\xi) + \frac{3}{2}y_b\Big],$$

$$(3.3.10)$$

with coefficients k_1, …, k_{14} being defined in Appendix B. Stresses associated with convection acting on the plates have the following forms:

$$\sigma_{xv,L} = \sigma_{t,L} = -\alpha \frac{y_b Ra}{Pr}[\frac{1}{10}\sin\xi - \frac{y_b}{40}\sin(2\xi)] + O(\alpha^3), \tag{3.3.11a}$$

$$\sigma_{xp,L} = \alpha\left\{\frac{y_b Ra}{Pr}\left[(\frac{3}{4} + \frac{y_b}{40} - \frac{y_b^2}{8(2-y_b)})\sin\xi - \frac{13y_b}{40}\sin(2\xi)\right] - Cy_b\sin\xi\right\} + O(\alpha^3), \tag{3.3.11b}$$

$$\sigma_{yv,L} = 0(\alpha^2), \qquad \sigma_{yp,L} = \frac{Ra}{Pr}\left[\frac{3}{4} + \frac{y_b}{40} - \frac{y_b^2}{8(2-y_b)} - \frac{13y_b}{20}\cos\xi\right] - C + 0(\alpha^2), \tag{3.3.11c,d}$$

$$\sigma_{n,L} = \sigma_{np,L} = -\frac{Ra}{Pr}\left[\frac{3}{4} + \frac{y_b}{40} - \frac{y_b^2}{8(2-y_b)} - \frac{13y_b}{20}\cos\xi\right] + C + O(\alpha^2), \tag{3.3.11e}$$

$$\sigma_{xv,U} = \sigma_{t,U} = \alpha\frac{y_b Ra}{Pr}[\frac{1}{15}\sin\xi - \frac{y_b}{60}\sin(2\xi)] + O(\alpha^3), \qquad \sigma_{xp,U} = 0 \tag{3.3.11f,g}$$

$$\sigma_{yv,U} = 0(\alpha^2), \qquad \sigma_{yp,U} = \frac{Ra}{Pr}\left[\frac{1}{4} - \frac{y_b}{40} + \frac{y_b^2}{8(2-y_b)} + \frac{3y_b}{20}\cos\xi\right] + C + 0(\alpha^2), \tag{3.3.11h,i}$$

$$\sigma_{n,U} = \sigma_{np,U} = \frac{Ra}{Pr}\left[\frac{1}{4} - \frac{y_b}{40} + \frac{y_b^2}{8(2-y_b)} + \frac{3y_b}{20}\cos\xi\right] + C + O(\alpha^2). \tag{3.3.11j}$$

The above relations show that viscous stresses are proportional to Ra, inversely proportional to Pr and have a complex dependence on y_b. Since $y_b < 2$, analysis of (3.3.11a) shows that $\sigma_{t,L} < 0$ for $x \in (0, \lambda/2)$ which means that shear stress acts towards corrugation peaks. This would result in steepening of the slopes, increase of the peaks' elevation and flattening of the troughs' bottoms if erosion was allowed. If the lower plate was replaced by a membrane, the convection would result in its stretching with the membrane being pulled away from the troughs. The total stretching force per half of the corrugation wavelength $H_{t,L}$

$$H_{t,L} = 2\lambda^{-1}\int_0^{\frac{\lambda}{2}}\sigma_{t,L} N_L^{-1}dx = -\alpha\frac{y_b Ra}{5\pi Pr}, \tag{3.3.12a}$$

The reader may note that the total stretching forces per one corrugation wavelength are zero. The pressure forces associated with the heating are also proportional to Ra, inversely proportional to Pr and have a complex dependence on y_b. While determination of their direction is not in general possible without knowledge of the free constant C, it is nevertheless possible to deduce if the pressure contributes either to the flattening or to the

growth of the corrugations, assuming that surface deformation is allowed. In the former case, the difference Dif_1 between the y-components of forces acting on the upper ($H_{y,peak}$) and the lower parts of the corrugation ($H_{y,trough}$) defined as (see Fig.3.3)

$$Dif_1 = H_{y,peak} - H_{y,trough} = \tag{3.3.13}$$

$$2\lambda^{-1} \int_{-\lambda/4}^{\lambda/4} (\sigma_{yp,L} + \sigma_{yv,L}) dx - \qquad 2\lambda^{-1} \int_{\lambda/4}^{3\lambda/4} (\sigma_{yp,L} + \sigma_{yv,L}) dx = -\frac{13 y_b Ra}{5\pi Pr},$$

must be negative which is always the case, i.e. pressure in the case of the long wavelength corrugations always acts in a manner which contributes to the corrugation flattening.
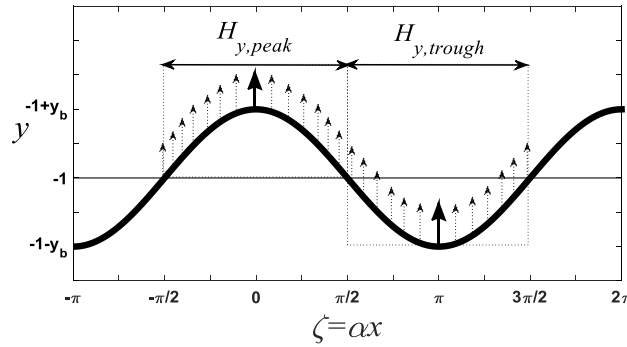
Figure 3.3: Sketch of pressure forces acting on the corrugated plate.

The local and average Nusselt numbers, which can be expressed as

$$Nu_{loc,L} = Nu_{cond,loc,L} = Ra(2 - y_b \cos\xi)^{-1} + O(\alpha^2), \tag{3.3.14a,b}$$

$$Nu_{av} = Nu_{cond,av} = Ra(4 - y_b^2)^{-1/2} + O(\alpha^2),$$

demonstrate that the heat flow is dominated by conduction, its magnitude is proportional to Ra, it is independent of Pr and it increases rapidly with y_b. The reader may note that the local heat flux is largest at the corrugation tip and smallest at the bottom of the trough.

The range of applicability of solution for $\alpha \to 0$ can be determined from comparisons with the solution of the complete system. The difference between both solutions is defined using norm of the form

$$||Er||_{max} \overset{\text{def}}{=} \underbrace{sup}_{0 \le \xi \le 2\pi, \ -1 \le \eta \le 1} |\phi_n(\xi, \eta) - \phi_a(\xi, \eta)|, \tag{3.3.15}$$

where ϕ stands for any of u, v, θ, p and the subscripts "a" and "n" correspond to the asymptotic and complete solutions, respectively. Results presented in Fig.3.4 demonstrate that the error decreases as predicted by the analysis and the asymptotic solution provides acceptable accuracy for $\alpha < 0.1$.
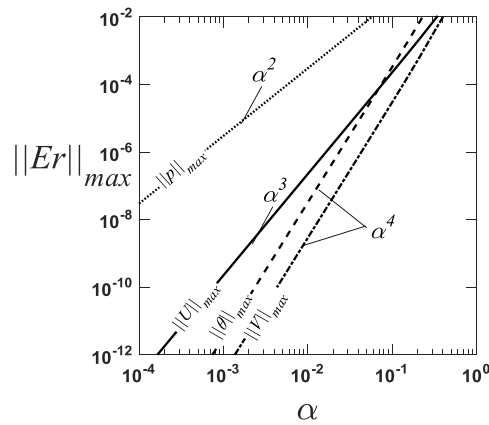
Figure 3.4: Variations of the error $||Er||_{max}$ for u, v, θ, p (see Eq. 3.3.15) as a function of α for $y_b = 0.1, Ra = 150$.

3.3.2 Corrugation with an arbitrary wave number

Typical flow field topologies displayed in Fig.3.5 suggest that the roll size is dictated by the corrugation wavelength. In the case of long wavelengths, the rolls completely fill in the slot (see Fig.3.5A) while convection, as measured by the maximum of the stream function, is very weak (see Fig.3.6A) and the temperature field modulations are relatively small. Reduction of the wavelength down to $\alpha \approx 1$ results in the intensification of convection (see Fig.3.6A) with the rolls completely filling in the slot and with significant modifications of the temperature field (see Fig.3.5B). Further reduction of the wavelength down to $\alpha = 5$ results in the weakening of convection (see Fig.3.6A) with the fluid movement as well as the temperature modifications concentrated in a boundary layer

adjacent to the corrugated plate (see Fig.3.5C); the thickness of this boundary rapidly decreases with an increase of α. Analysis carried out in Section 3.3.1 shows that $|\psi|_{max} = 0(\alpha)$ when $\alpha \to 0$ and analysis carried out using method described in (Hossain & Floryan 2014; 2015a, 2015b) shows that $|\psi|_{max} = 0(\alpha^{-3})$ when $\alpha \to \infty$ (details not given).

(A)   (B)   (C)
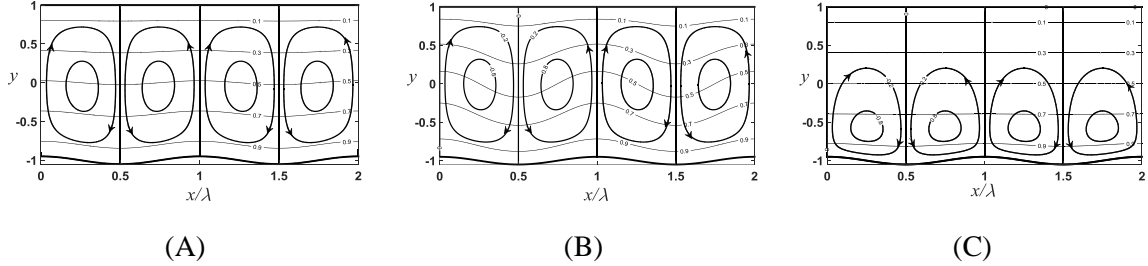
Figure 3.5: The flow and the temperature fields for $Ra = 200$, $y_b = 0.05$ and $\alpha = 0.1$ (Fig.3.5A), $\alpha = 1.53$ (Fig.3.5B) and $\alpha = 5$ (Fig.3.5C) normalized with their maxima. The maxima of the stream function are: a) $|\psi|_{max} = 0.0149$, b) $= 0.7786$, c) $|\psi|_{max} = 0.0040$. The maxima of the temperature are $\theta_{max} = Ra$ in all cases.

The effects of the remaining parameters can be deduced from the other data displayed in Fig.3.6. An increase of y_b results in an increase of $|\psi|_{max}$ initially proportional of y_b, as demonstrated using small amplitude approximation described in Appendix C, but slowing down for larger y_b's as nonlinear effects become more important and convection saturates (see Fig.3.6B). The saturation occurs at smaller y_b's for larger Ra's. An increase of Ra results in an increase of $|\psi|_{max}$ initially proportional to Ra followed by a rapid acceleration for $Ra > 100$ (see Fig.3.6C). This suggests that the system approaches a stability limit as the critical value of the Rayleigh number in the case of smooth plates is $Ra_{cr} = 213.5$ (Rayleigh 1916). The initial rate of growth of $|\psi|_{max}$ can be predicted analytically using the weak convection assumption following (Floryan & Floryan et al. 2015) and (Hossain & Floryan 2013).
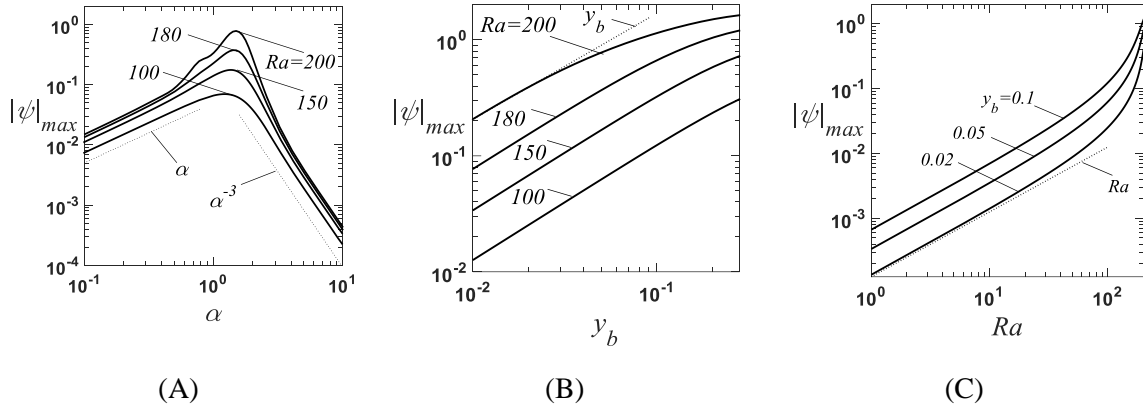
Figure 3.6: Variations of the maximum of the stream function $|\psi|_{max}$ as a function of α for $y_t = 0$, $y_b = 0.05$ (Fig.3.6A), as a function of y_b for $\alpha = 1.53$, $y_t = 0$ (Fig.3.6B), and as a function of Ra for $\alpha = 1.53$, $y_t = 0$ (Fig.3.6C).
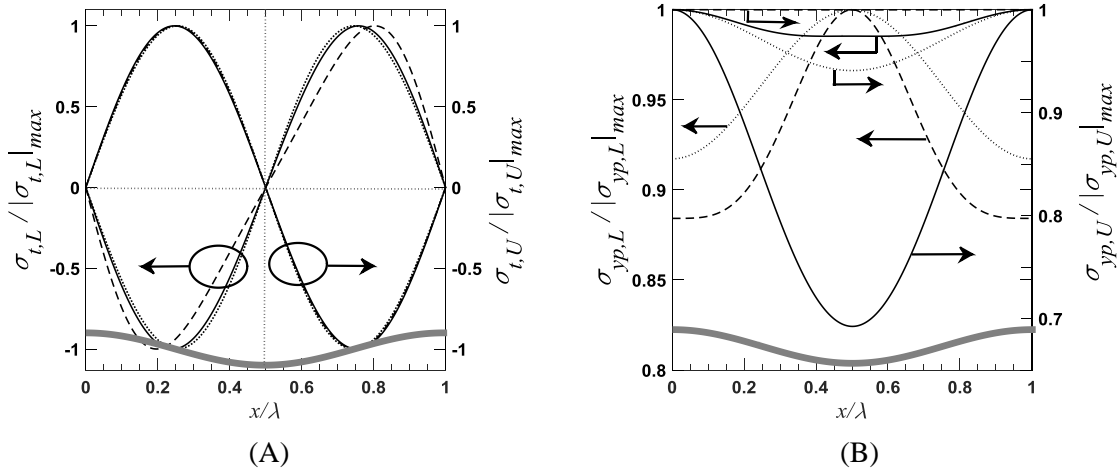
Figure 3.7: Variations of $\sigma_{t,L}$, $\sigma_{t,U}$ (Fig.3.7A) and of $\sigma_{yp,L}$, $\sigma_{yp,U}$ (Fig.3.7B) for $y_b = 0.05$, $y_t = 0$, $Ra = 200$, and $C = 0$. Dotted, solid, and dashed lines correspond to $\alpha = 0.1, 1.53, 5$. The maxima used for normalizations are: $|\sigma_{t,L}|_{max} = 0.1416, 6.8594, 0.3629$; $|\sigma_{t,U}|_{max} = 0.0947, 6.2586, 0.0041$; $|\sigma_{yp,L}|_{max} = 220.7034, 211.3108, 224.9411$; $|\sigma_{yp,U}|_{max} = 72.2485, 84.6565, 70.6266$.

Variations of forces acting on both plates are illustrated in Fig.3.7. Distribution of shear stresses is very similar for all α's, i.e. they always act towards corrugation peaks contributing to the corrugation build up if such an effect was permitted. Distribution of the *y*-component of pressure forces associated with the heating shows qualitative change with the maxima occurring at the corrugation troughs for small and large α's but at the corrugation tips for medium α's. Contours of Dif_1 displayed in Fig.3.8 show that pressure

may act in a manner consistent with corrugation build up but only if Ra exceeds the critical value of 192.6, only for a certain finite range of α's and only for a sufficiently small corrugation amplitude. Pressure always contributes to the flattening of the corrugation if < 192.6, α's are either excessively small or excessively large, and amplitude is too big. In particular, pressure supports corrugation built up for $Ra = 193$, 196, 200, 201 when $\alpha \in$ (1.42, 1.53), (1.31, 1.65), (1.24, 1.73), (1.13, 1.88) and $y_t <$ 0.016, 0.051, 0.076, 0.12, respectively. Details of the system response have been determined using the small-amplitude solution described in Appendix C.
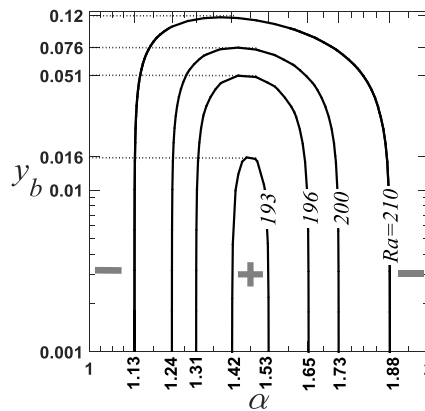
Figure 3.8: Contour plots of $Dif_1 = 0$ (see Eq.3.3.13) in the (α, y_b)-plane for $y_t = 0$.

Changes of the heat transfer illustrated in Fig.3.9A demonstrate the existence of a range of α where convective effects play a role. To help with interpretation, we represent the temperature field θ as a superposition of the conductive and convective components, i.e.

$$\theta = \theta_{cond} + \theta_{conv}, \tag{3.3.16}$$

where θ_{cond} represents solution of the conduction problem (3.2.16) and θ_{conv} has been determined by subtracting θ_{cond} from θ. The average Nusselt number can be similarly represented as a superposition of Nusselt numbers associated with each field, i.e.

$$Nu_{av} = Nu_{cond,av} + Nu_{conv,av}. \tag{3.3.17}$$

The conductive part has a well-known smooth-slot limit, i.e. $Nu_{cond,av} \rightarrow Ra/2$ when y_b $\rightarrow 0$. Results displayed in Fig.3.9 permit to follow changes of both $Nu_{cond,av}$ and $Nu_{conv,av}$ as functions of the corrugation geometry. Figure 3.9A displays variations of the excess heat flow above that occurring in the smooth slot, i.e. $\frac{Nu_{av}}{Ra} - \frac{1}{2}$. The limit of this quantity for the long wavelength corrugations can be easily determined using solution from Section 3.3.1, i.e.

$$\lim_{\alpha \to 0}\left(\frac{Nu_{av}}{Ra} - \frac{1}{2}\right) = \frac{1}{2}\left\{\left[1 - \left(\frac{y_b}{2}\right)^2\right]^{-1/2} - 1\right\} \approx \frac{y_b^2}{16} \approx 1.56 * 10^{-4}. \tag{3.3.18}$$

The heat flow in the limit of $\alpha \to 0$ is always a bit higher than in the smooth slot and this is due to the conduction modifications which are functions of y_b. Increase of α away from this limit increases the conductive effect but, at $\alpha \approx 0.4$ convective effects begin to play a role and the heat flow increases above that expected from the pure conduction. Convective effects peak at $\alpha \approx 1.53$ and then rapidly decrease with the heat flow being again dominated by conduction. The upper limit of this growth can be easily determined as conductive heat flow cannot be larger than that in a slot whose height has been reduced by half of the corrugation amplitude, i.e. $\lim_{\alpha \to \infty} Nu_{cond,av} = \frac{Ra}{(2-y_b)}$. The character of variations of convective effects are well illustrated in Fig.3.9B. These effects need to be accounted for only for medium α's as they decrease as α^4 when $\alpha \to 0$ and as α^{-7} when $\alpha \to \infty$. The dependence of the heat transfer modifications as a function of the corrugation amplitude can be deduced from the results displayed in Fig.3.9C. Nu_{av} increases away from the smooth-slot limit of $Ra/2$ proportionally to y_b^2, as shown in Appendix C, and then this growth begins to saturate when the amplitude becomes excessively large (see Fig. 3.9C). This saturation is associated with the fact that increase of the amplitude increases the wetted area which in turn increases dissipation. While horizontal temperature gradients, which are responsible for driving this convection, increase with an increase of y_b, the increase of dissipation eventually begins to slow down the growth of intensity of convection. Results displayed in Fig.3.9D demonstrate that the convective heat flow initially increases proportionally to Ra^3 with this growth rapidly

accelerating when Ra approaches the critical value for the smooth-slot limit where it gives rise to transition to a secondary state. Variations of the local Nusselt number displayed in Fig.3.10A demonstrate that the maxima of $Nu_{loc,L}$ occur at the corrugation peaks for small and large α's but at the corrugation troughs for medium α's. This effect is associated with a larger role of convective effects for medium α's and their negligible role for large and small α's. The changeover is well illustrated in Fig.3.10B displaying variations of the difference Dif_2 between $Nu_{loc,L}$ at $x = 0$ and at $x = \lambda/2$, i.e. between the peak and the bottom of the trough, defined as

$$Dif_2 = Nu_{loc,L}(0) - Nu_{loc,L}(\lambda/2) \,, \tag{3.3.19}$$

as a function of α and y_b. The changeover can occur only if Ra exceeds the critical value of 161.9, only for a certain finite range of α's and only for a sufficiently small corrugation amplitude. Most of the heat flow occurs around the corrugations peaks if Ra is sufficiently small, α's are either sufficiently small or sufficiently large, and amplitude is sufficiently large. In particular, most of heat flow occurs in the vicinity of the corrugation troughs for $Ra = 162, 165, 180, 200$ when $\alpha \in (1.26, 1.29), (1.11, 1.45), (0.91, 1.73), (0.78, 1.95)$, respectively. Details of the system response have been determined using the small-amplitude solution described in Appendix C.
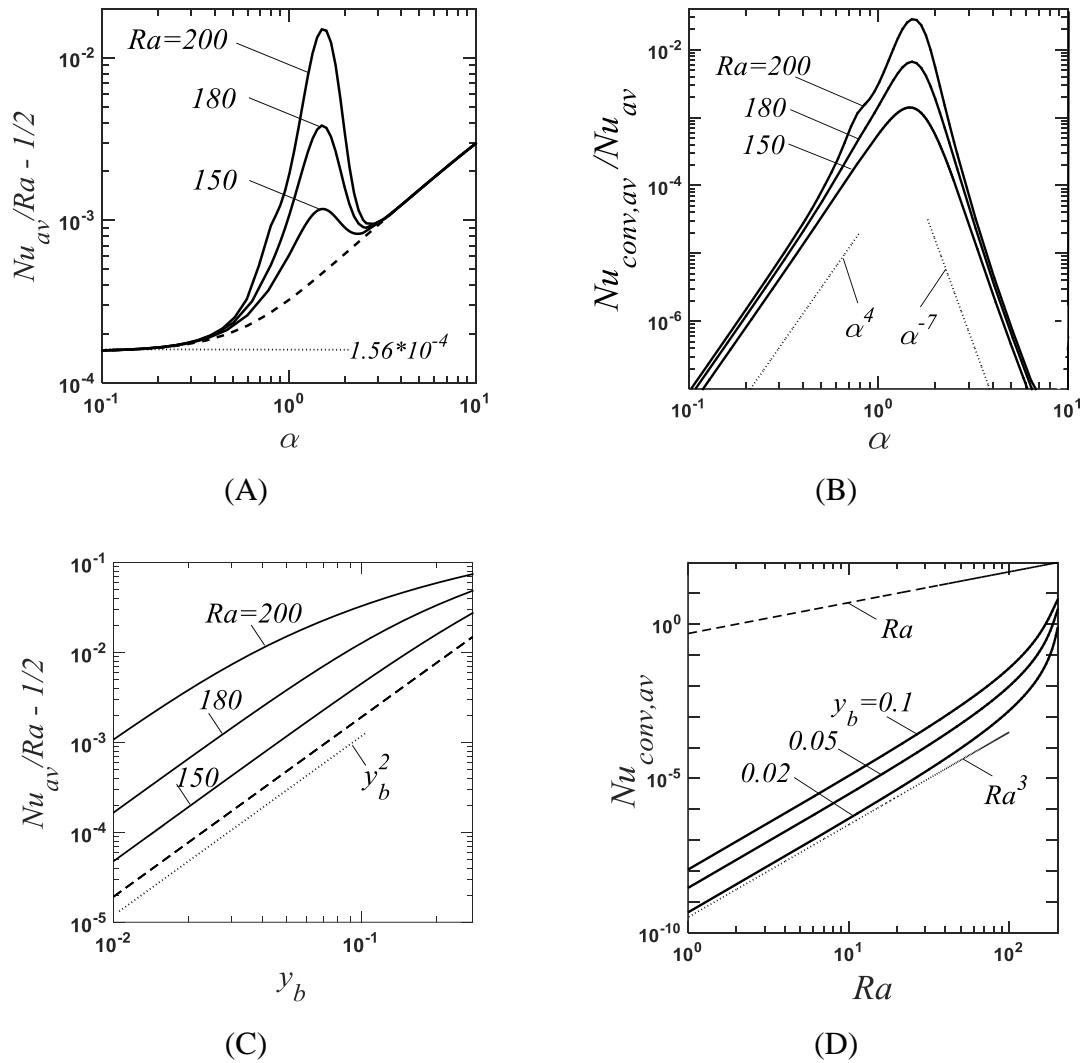
Figure 3.9: Variations of the excess heat flow due to corrugation $\frac{Nu_{av}}{Ra} - 1/2$ (Fig.3.9A) and the ratio of the convective and average Nusselt numbers $Nu_{conv,av}/Nu_{av}$ (Fig.3.9b) as functions of the wave number α for $y_b = 0.05$, $y_t = 0$; variations of the excess heat flow due to corrugation $\frac{Nu_{av}}{Ra} - 1/2$ as a function of y_b for $\alpha = 1.53$, $y_t = 0$ (Fig.3.9C) and variations of $Nu_{conv,av}$ as a function of Ra for $\alpha = 1.53$, $y_t = 0$ (Fig.3.9D). Thin dotted lines represent asymptotes. Dashed lines correspond to the conductive Nusselt number $Nu_{cond,av}$; such lines for different y_b's overlap in Fig.3.9D.
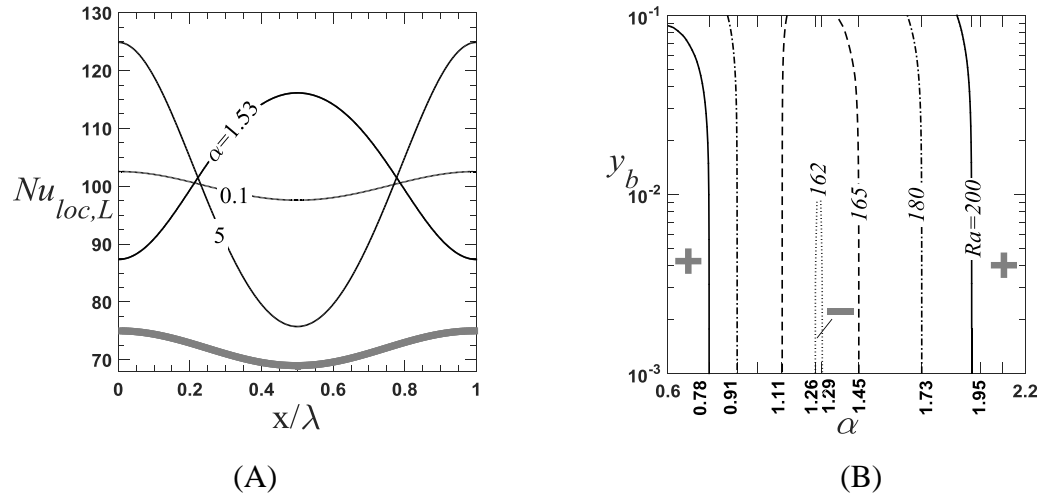
Figure 3.10: Variations of the local Nusselt number $Nu_{loc,L}$ as a function of x for $Ra = 200$, $y_b = 0.05, y_t = 0$, $\alpha = 0.1$, 1.53, 5 (Fig.3.10A) and contour plots of $Dif_2 = 0$ (see Eq.3.3.19) in the (α, y_b)-plane (Fig.3.10B).

3.4. Convection driven by corrugation placed at the upper plate

Pattern of motion for the same conditions as used in Fig.3.2 but with the corrugation moved to the upper plate is displayed in Fig.3.11. The fluid flows upwards below the corrugation trough and downwards below the corrugation peak. The flow topology is the same as in the case of corrugation placed at the lower plate displayed in Fig.3.2. One can map both topologies using the up/down symmetry combined with a phase shift of $\lambda/2$. Because of that, the global convection characteristics for corrugation at the upper plate can be deduced from the known characteristics of convection associated with corrugation at the lower plate. The system response is qualitatively similar to that found in the case of a smooth slot subject to periodic heating either at the lower or upper plates (Winters & Young 2009).
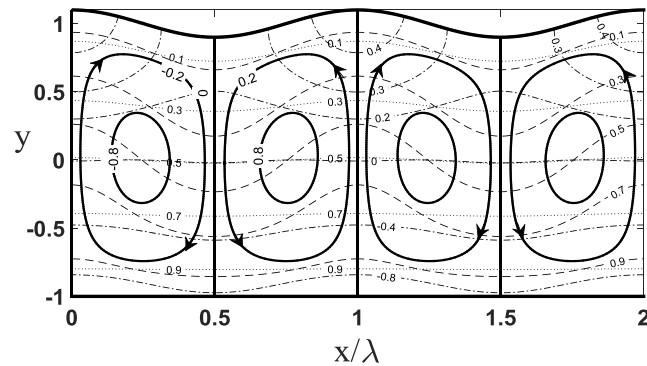
Figure 3.11: The flow topology and the temperature and pressure fields in a slot with $\alpha = 1.53$, $y_t = 0.1$ for the same heating conditions as in Fig.3.2, i.e. $Ra = 200$, normalized with their maxima. The solid, dashed, dashed-dotted and dotted lines identify streamlines, isotherms of the complete temperature field, lines of constant pressure and isotherms of the conductive temperature field, respectively. The maxima of the stream function and the temperature, pressure and conduction temperature fields are $|\psi|_{max} = 1.1452, |\theta|_{max} = 200, |p|_{max} = 213.7, |\theta_{cond}|_{max} = 200$, respectively. The pressure constant has been set at $C = 0$.

3.5. Convection driven by corrugations placed at both plates

Patterns of motion displayed in Fig. 3.12 demonstrate a strong dependence on the phase shift Ω_C between the lower and upper corrugations. Convection forms a single layer of rolls in the case of the "wavy slot" with the fluid rising up above peaks of the lower corrugation and flowing down above its troughs (see Fig.3.12 A). As Ω_C increases from 0 to π, the rolls begin to deform, the inflow stagnation points form in the middle of the slot and the rolls split into two layers when $\Omega_C = \pi$ with the slot assuming the "converging-diverging" form. This transition is very rapid as illustrated in Figs 3.12C, D, E which display flow topologies for $\Omega_C = 0.995\,\pi$, $0.999\,\pi$ and π. We shall begin detailed discussion with the long wavelength corrugations, i.e. with the limit $\alpha \rightarrow 0$.

(A)   (B)   (C)

(D)   (E)   (F)
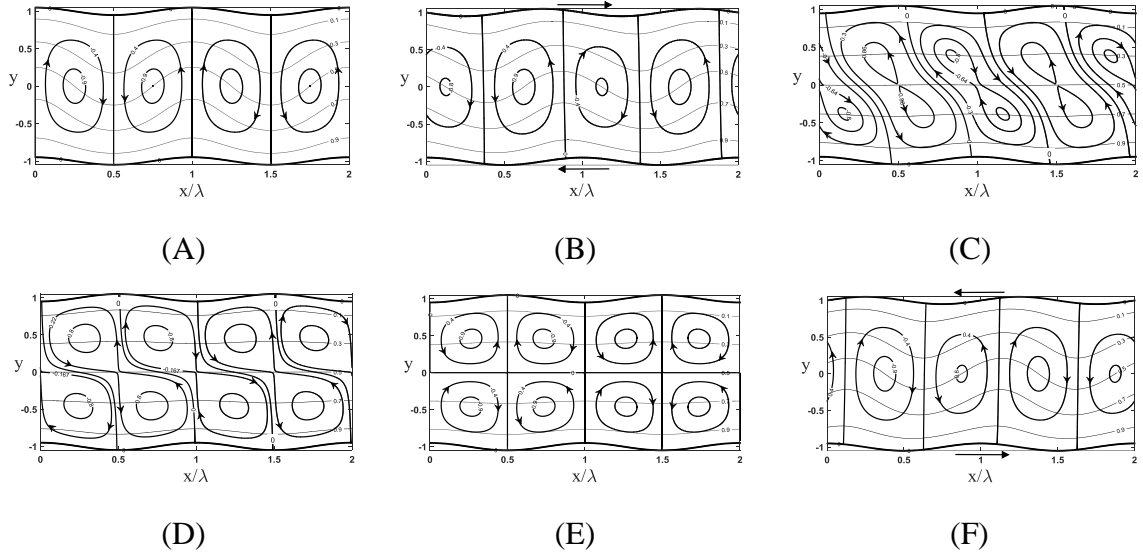
Figure 3.12: Flow and temperature fields for $\alpha = 1.53$, $Ra = 200$, $y_t = y_b = 0.05$ and A) $\Omega_C = 0$ (the "wavy" slot), B) $\Omega_C = \pi/2$, C) $\Omega_C = 0.995\,\pi$, D) $\Omega_C = 0.999\,\pi$, E) $\Omega_C = \pi$ (the "converging-diverging" slot), and F) $\Omega_C = 3\pi/2$, The maxima of the stream function, the average Nusselt numbers and the conduction Nusselt numbers in Figs A,…F are: $|\psi|_{max} = 1.1696, 1.0709, 0.0232, 0.0179, 0.0173, 1.0709$, $Nu_{av} = 106.6463, 104.7624, 100.2124, 100.2110, 100.2109, 104.7624$, $Nu_{cond,av} = 100.1741, 100.1922, 100.2103, 100.2103, 100,2103, 100.1922$, respectively.

3.5.1. Long-wavelength corrugation

Transformation of the form

$$\xi = \alpha x, \quad \eta = 2\frac{y-1-y_t cos(\xi+\Omega_C)}{2+y_t cos(\xi+\Omega_C)-y_b \cos \xi}+1 \tag{3.5.1}$$

maps the corrugated slot into a regular strip $\eta \in [-1,1]$ and introduces the slow scale ξ. The field equations assume form (3.3.2) with the coefficients defined in Appendix D. The solution process follows method described in Section 3.3.1. The three leading-order systems are described in Appendix D. Their solutions have the following forms

$$u_0 = 0, \tag{3.5.2a-c}$$
$$u_1 = \frac{Ra}{1536\ Pr}(\eta^2 - 1)\left\{L_u + \sum_{n=1}^{3}\left[LS_{u,n}sin(n\xi) + LC_{u,n}cos(n\xi)\right]\right\}, \quad u_2 = 0,$$

$$v_0 = 0, \quad\quad v_1 = 0, \tag{3.5.3a-b}$$
$$v_2 = \frac{Ra}{7680\ Pr}(\eta^2 - 1)\left\{L_v + \sum_{n=1}^{6}\left[LS_{v,n}sin(n\xi) + LC_{v,n}cos(n\xi)\right]\right\},$$

$$p_{-1} = 0, \tag{3.5.4a-c}$$
$$p_0 = -\frac{Ra}{40\ Pr(2-y_b+y_t cos\Omega_C)}\left\{L_p + LS_{p,1}sin(\xi) + LC_{p,1}cos(\xi)\right\} + C,$$
$$p_1 = 0$$

$$\theta_0 = \frac{Ra}{2}(1 - \eta), \quad\quad \theta_1 = 0, \tag{3.5.5a-c}$$
$$\theta_2 = L_\theta + \sum_{n=1}^{7}\left[LS_{\theta,n}sin(n\xi) + LC_{\theta,n}cos(n\xi)\right],$$

where all coefficients L, LS and LC are given in Appendix D. The x-components of stresses as well as the tangential stresses acting on each plate can be easily determined, i.e.

$$\sigma_{xv,L} = \sigma_{t,L} = -\alpha\frac{Ra}{120Pr}\left\{L_{vL} + \sum_{n=1}^{2}\left[LS_{vL,n}sin(n\xi) + LC_{vL,n}cos(n\xi)\right]\right\} + O(\alpha^3), \tag{3.5.6a}$$

$$\sigma_{xv,U} = \sigma_{t,U} = \alpha \frac{Ra}{120Pr}\left\{L_{vU} + \sum_{n=1}^{2}\left[LS_{vU,n}sin(n\xi) + LC_{vU,n}cos(n\xi)\right]\right\} + O(\alpha^3), \qquad (3.5.6b)$$

$$\sigma_{xp,L} = \alpha\left\{\frac{y_b Ra}{80\ Pr(2-y_b+y_t\ cos\ \Omega_C)}\left\{L_{pL} + \sum_{n=1}^{2}\left[L_{pL,n}sin(n\xi) + LC_{pL,n}cos(n\xi)\right]\right\} - \qquad (3.5.6c)$$

$$Cy_b\ sin\ \xi\right\} + O(\alpha^2),$$

$$\sigma_{xp,U} = \alpha\left\{\frac{y_t Ra}{80\ Pr(2-y_b+y_t\ cos\ \Omega_C)}\left\{L_{pU} + \sum_{n=1}^{2}\left[LS_{pU,n}sin(n\xi) + LC_{pU,n}cos(n\xi)\right]\right\} + \qquad (3.5.6d)$$

$$C\ y_t\ sin(\xi + \Omega_C)\right\} + O(\alpha^2),$$

where all coefficients *L, LC* and *LS* are also given in Appendix D. The reader may note the appearance of aperiodic terms which have interesting physical consequences discussed latter in this presentation. It is instructive to write these distributions for $y_b = y_t = S$ for three special Ω_C's whose significance will become obvious later in the discussion, i.e.

$$\Omega_C = 0:\ \ \sigma_{t,L} = -\alpha\frac{SRa}{6Pr}\sin\xi, \qquad (3.5.7a)$$

$$\sigma_{t,U} = \alpha\frac{SRa}{6Pr}\sin\xi,$$

$$\Omega_C = \frac{\pi}{2}:\ \ \sigma_{t,L} = -\alpha\frac{SRa}{120Pr}[12\sin\xi + 8\cos\xi - 5S\sin(2\xi) + S\cos(2\xi) - 5S], \qquad (3.5.7b)$$

$$\sigma_{t,U} = \alpha\frac{SRa}{120Pr}[8\sin\xi + 12\cos\xi - 5S\sin(2\xi) - S\cos(2\xi) - 5S],$$

$$\Omega_C = \pi:\ \ \sigma_{t,L} = -\alpha\frac{SRa}{120Pr}[4\sin\xi - 2S\sin(2\xi)], \qquad (3.5.7c)$$

$$\sigma_{t,U} = -\alpha\frac{SRa}{120Pr}[4\sin\xi - 2S\sin(2\xi)].$$

The total forces acting in the *x*-direction per unit length of the slot are determined through integration, i.e.

$$F_{x,L} = F_{xv,L} + F_{xp,L} = \lambda^{-1}\int_0^\lambda \sigma_{xv,L}\ N_L^{-1}dx + \lambda^{-1}\int_0^\lambda \sigma_{xp,L}\ N_L^{-1}dx = \qquad (3.5.8a)$$

$$+\alpha\frac{y_b y_t Ra}{24Pr}\sin\Omega_C - \alpha\frac{3y_b y_t Ra}{40Pr}\sin\Omega_C + O(\alpha^2) = -\alpha\frac{y_b y_t Ra}{30Pr}\sin\Omega_C + O(\alpha^2),$$

$$F_{x,U} = F_{xv,U} + F_{xp,U} = \lambda^{-1} \int_0^\lambda \sigma_{xv,U} \, N_U^{-1} dx + \lambda^{-1} \int_0^\lambda \sigma_{xp,U} \, N_U^{-1} dx = \tag{3.5.8b}$$

$$-\alpha \frac{y_b y_t Ra}{24 Pr} \sin \Omega_C + \alpha \frac{3 y_b y_t Ra}{40 Pr} \sin \Omega_C + O(\alpha^2) = \alpha \frac{y_b y_t Ra}{30 Pr} \sin \Omega_C + O(\alpha^2),$$

where $F_{x,L}$ and $F_{x,U}$ denote forces acting at the lower and upper plates, respectively, and $F_{xv,L}$, $F_{xv,U}$ and $F_{xp,L}$, $F_{xp,U}$ denote their shear (viscous) and pressure components, respectively. The reader may note that these forces do not balance out within one period as the aperiodic terms generate a net force, with pressure opposing shear and prevailing. Forces at the upper and lower plates are equal but act in the opposite directions producing a moment M with the magnitude

$$M = F_{x,U} * 2 = \alpha \frac{y_b y_t Ra}{15 Pr} \sin \Omega_C + O(\alpha^2) \tag{3.5.9}$$

which attempts to change the relative position of the plates. Positive M corresponds to the upper plate being pushed to the right. Appearance of this moment correlates with the lack of symmetry between the intensity of the clockwise and anti-clockwise rotations in the neighboring cells (see Fig.3.12). This dynamical system has two states of equilibria defined by $M = 0$, i.e. the "wavy" slot with $\Omega_C = 0$ and the "converging-diverging" slot with $\Omega_C = \pi$. The second state is unstable as any small displacement from this position results in the formation of a moment which attempts to change the relative position of both plates until the "wavy" configuration is achieved, assuming that a relative movement of both plates is possible. The reader may note that $\Omega_C = \pi/2$ results in the largest M. Moment created by a single corrugation may be small but a significant force may be created when many wavelengths are involved.

The shear stresses are directed towards the corrugation peaks, thus, potentially contributing to the corrugation build up although this may not be obvious from the functional form (3.5.6). Distributions of stresses for $\Omega_C = 0$, $\frac{\pi}{2}$, π displayed in Fig.3.13 demonstrate this effect. The same comments apply to the stretching force which would affect membrane dynamics if the slot was formed by such membranes. The stretching

force has a periodic component, which changes direction within each corrugation half-wavelength, as well as an average, non-zero component which pulls the complete membrane in a direction dictated by the phase shift Ω_C. The magnitude of the periodic component can be estimated by integrating shear stress between corrugation's peak and trough, i.e.

$$H_{t,L} = 2\lambda^{-1}\int_0^{\frac{\lambda}{2}}\sigma_{t,L}\,N_L^{-1}dx = -\alpha\frac{Ra}{120\pi Pr}(24y_b + 16y_t cos\Omega_C - \tag{3.5.10a}$$

$$5\pi y_b y_t sin\Omega_C),$$

$$H_{t,U} = 2\lambda^{-1}\int_{\frac{\lambda}{2}-\frac{\Omega_C}{\alpha}}^{\lambda-\frac{\Omega_C}{\alpha}}\sigma_{t,U}\,N_U^{-1}dx = -\alpha\frac{Ra}{120\pi Pr}(24y_t + 16y_b cos\Omega_C + \tag{3.5.10b}$$

$$5\pi y_b y_t sin\Omega_C),$$

In the special cases of $\Omega_C = 0, \frac{\pi}{2}, \pi$ these forces become $H_{t,L} = -\alpha\frac{S\,Ra}{3\pi Pr}$, $-\alpha\frac{S\,Ra}{120\pi Pr}(24 - 5\pi S)$, $-\alpha\frac{S\,Ra}{15\pi Pr}$, and $H_{t,U} = -\alpha\frac{S\,Ra}{3\pi Pr}$, $-\alpha\frac{S\,Ra}{120\pi Pr}(24 + 5\pi S)$, $-\alpha\frac{S\,Ra}{15\pi Pr}$, respectively.
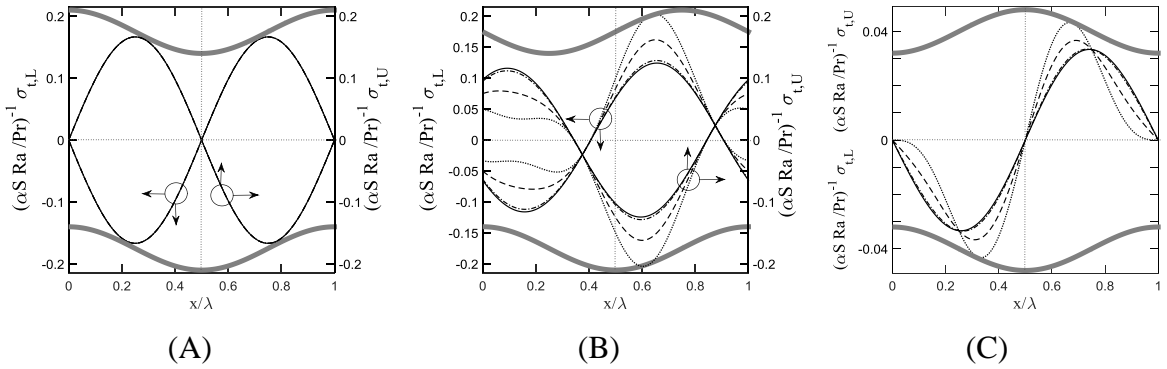
Figure 3.13: Distributions of tangential stresses acting on both plates for $\Omega_C = 0$ (Fig.3.13A), $\Omega_C = \frac{\pi}{2}$ (Fig.3.13B), $\Omega_C = \pi$ (Fig.3.13C) for $Ra =200$. Solid, dashed-dotted, dashed, and dotted lines correspond to $y_b = y_t = S = 0.05, 0.1, 0.5, 1$, respectively. All lines overlap in Fig.3.13A.

The *y*-components of forces acting on the plates can also be easily determined resulting in the following expressions

$$\sigma_{yv,L} = 0(\alpha^2), \tag{3.5.11a-b}$$

$$\sigma_{yp,L} = \frac{Ra}{40\,Pr(2-y_b+y_t cos\Omega_C)}(L_1 sin\xi + L_2 cos\xi + L_3) + C + O(\alpha^2),$$

$$\sigma_{yv,U} = O(\alpha^2), \qquad (3.5.11\text{c-d})$$

$$\sigma_{yp,U} = -\frac{Ra}{40\,\Pr(2-y_b+y_t cos\Omega_C)}(L_4 sin\xi + L_5 cos\xi + L_6) + C + O(\alpha^2),$$

which demonstrate that pressure plays the dominant role. To answer the question if the pressure attempts to flatten corrugations, we compute difference between the total pressure force acting on the part of the corrugation that bulges inwards $H_{y,peak}$ and on the part that bulges outwards $H_{y,trough}$. Such differences for the lower $(Dif_{1,L})$ and upper $(Dif_{1,U})$ plates are defined as follows:

$$Dif_{1,L} = H_{y,peak,L} - H_{y,trough,L} = 2\lambda^{-1}\int_{-\frac{\lambda}{4}}^{\frac{\lambda}{4}}(\sigma_{yp,L} + \sigma_{yv,L})dx - \qquad (3.5.12\text{a})$$

$$2\lambda^{-1}\int_{\frac{\lambda}{4}}^{\frac{3\lambda}{4}}(\sigma_{yp,L} + \sigma_{yv,L})dx = -\frac{Ra}{20\pi\Pr}(52y_b - 12y_t cos\Omega_C),$$

$$Dif_{1,U} = H_{y,peak,U} - H_{y,trough,U} = 2\lambda^{-1}\int_{\frac{\lambda}{4}-\frac{\Omega_C}{\alpha}}^{\frac{3\lambda}{4}-\frac{\Omega_C}{\alpha}}(\sigma_{yp,U} + \sigma_{yv,U})dx - \qquad (3.5.12\text{b})$$

$$2\lambda^{-1}\int_{-\frac{\lambda}{4}-\frac{\Omega_C}{\alpha}}^{\frac{\lambda}{4}-\frac{\Omega_C}{\alpha}}(\sigma_{yp,U} + \sigma_{yv,U})dx = -\frac{Ra}{5\pi\Pr}(7y_t + 3y_b cos\Omega_C),$$

Negative $Dif_{1,L}$ and positive $Dif_{1,U}$ imply flattening which takes the place when both corrugations have similar amplitudes.

The local and average Nusselt numbers can be expressed as

$$Nu_{loc,L} = Nu_{loc,U} = \frac{Ra}{2+y_t cos(\xi+\Omega_C)-y_b cos\xi} + O(\alpha^2), \qquad (3.5.13\text{a,b})$$

$$Nu_{av} = \frac{Ra}{\sqrt{4-y_b^2-y_t^2+2y_b y_t\,cos\Omega_C}} + O(\alpha^2).$$

The ratio R of the Nusselt numbers for slots with corrugations placed at both plates and at a single plate can be expressed as

$$R = \sqrt{\frac{4-y_b^2}{4-y_b^2-y_t^2+2y_b y_t\,cos\Omega_C}}, \qquad (3.5.14)$$

and its analysis shows that the heat transfer is increased only when $cos\Omega_C < \frac{y_t}{2y_b}$. In the case of equal amplitudes, the heat transfer is increased when $\pi/3 < \Omega_C < 5\pi/3$. This suggests a possible use of the positioning of the upper corrugation as a heat transfer control device as one can significantly increase/decrease the heat flow by simply changing the phase shift.

3.5.2. Corrugations with an arbitrary wave number

Discussion presented in the previous Section demonstrates that the phase shift Ω_C may potentially have a very strong effect on the convection. Results presented in Fig.3.14 illustrate the order of magnitude changes in the intensity of motion when Ω_C changes from 0 to π. The most intense motion occurs at $\alpha \approx 1.53$ and it rapidly decreases for both smaller and larger α's (see Fig.3.15A). The asymptotes do not depend on Ω_C and are $|\psi|_{max} = 0(\alpha)$ when $\alpha \to 0$ and $|\psi|_{max} = 0(\alpha^{-3})$ when $\alpha \to \infty$, i.e. are the same as for convection in a slot with one corrugated plate. $|\psi|_{max}$ increases initially proportionally to the amplitude of the corrugation, as shown in Fig.3.15B, until a saturation process is initiated and the rate of growth slows down. This saturation occurs fastest for $\Omega_C \approx 0$ when the convection is most intense. The intensity of convection initially increases proportionally to Ra, as illustrated in Fig.3.15C, and then it rapidly accelerates which suggests that the system may be approaching a stability limit. The most rapid acceleration is observed for $\Omega_C \approx \pi/2$.
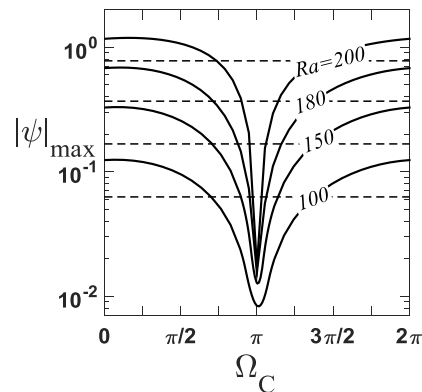
Figure 3.14: Variations of the maximum of the stream function $|\psi|_{max}$ as a function of the phase shift Ω_C for $y_b = y_t = 0.05$, $\alpha = 1.53$. Dashed lines correspond to a single corrugated plate.

(A)   (B)   (C)
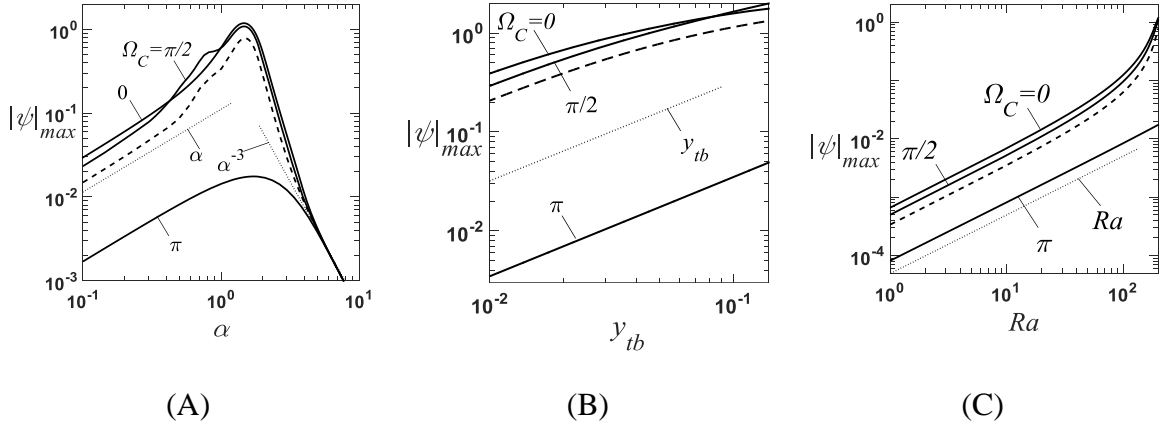
Figure 3.15: Variations of the maximum of the stream function $|\psi|_{max}$ as a function of α for $y_t = y_b = 0.05$, $\Omega_C = 0, \pi/2, \pi$ and $Ra = 200$ (Fig.3.15A), as a function of $y_{tb} = y_t = y_b$ for $\alpha = 1.53$, $Ra = 200$, $\Omega_C = 0, \pi/2, \pi$ (Fig.3.15B), and as a function of Ra for $\alpha = 1.53$, $y_t = y_b = 0.05$, $\Omega_C = 0, \pi/2, \pi$ (Fig.3.15C). Dashed-lines correspond to corrugation placed only on the lower plate.

Variations of the *x*-components of all forces acting at both plate per one corrugation wavelength as functions of Ω_C illustrated in Fig.3.16 demonstrate that their maxima occur for $\Omega_C \approx 7/12 \; \pi$ and $17/12 \; \pi$, the pressure force always opposes the viscous force and, since it is much stronger, it determines the direction of the total force. Results presented in Fig.3.17A demonstrate that the moment *M* changes rapidly as a function of the corrugation wave number with the largest magnitude attained for $\alpha \approx 1.5$ and this magnitude rapidly increases with *Ra*. Use of corrugations with smaller wave numbers reduces *M* proportionally to α and use of larger α's reduces *M* proportionally to α^{-11}. Figure 3.17B demonstrates that *M* is positive for $\Omega_C \in (0, \pi)$ and negative for $\Omega_C \in (\pi, 2\pi)$, it changes smoothly in the whole range of Ω_C, the maxima of $|M|$ occur at $\Omega_C \approx 7/12 \; \pi$ and $17/12 \; \pi$, and the zeros correspond to the two special points, i.e. to $\Omega_C = 0, \pi$.
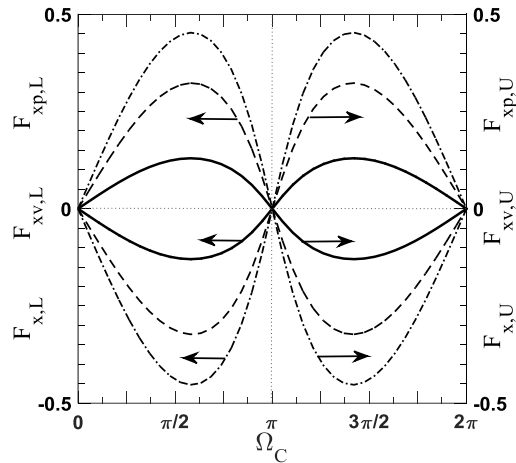
Figure 3.16: Variations of the x-component of shear forces at the lower ($F_{xv,L}$) and upper ($F_{xv,U}$) plates (dashed lines), the x-component of pressure forces at the lower ($F_{xp,L}$) and upper ($F_{xp,U}$) plates (Dashed-dotted lines) as well as their sums ($F_{x,L}, F_{x,U}$; solid lines) as functions of the phase shift Ω_C for $\alpha = 1.53$, $Ra = 200$, $y_t = y_b = 0.05$.

(A)

(B)
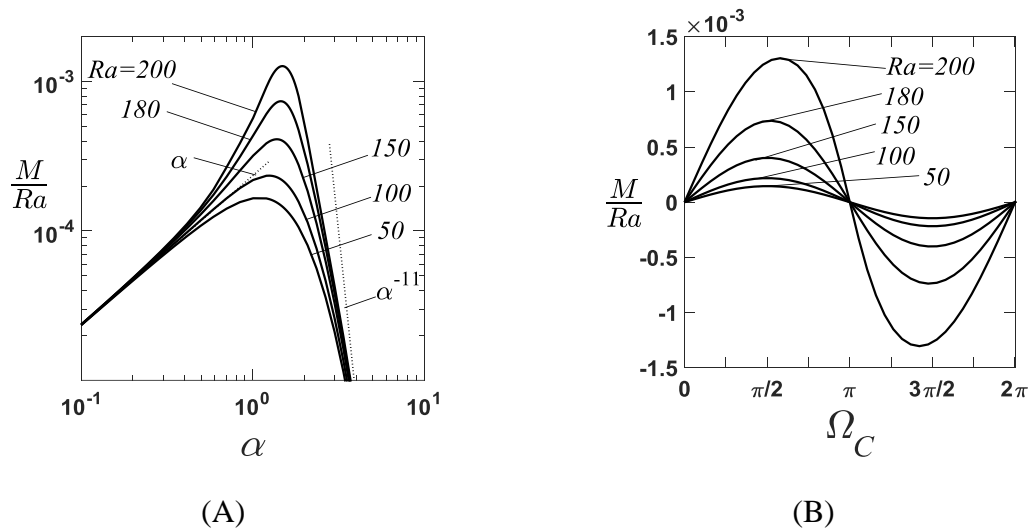
Figure 3.17: Variations of the moment M as a function of α for $\Omega_C = \frac{\pi}{2}$ (Fig.3.17A) and as a function of Ω_C for $\alpha = 1.49$ (Fig.3.17B) for $y_t = y_b = 0.05$.
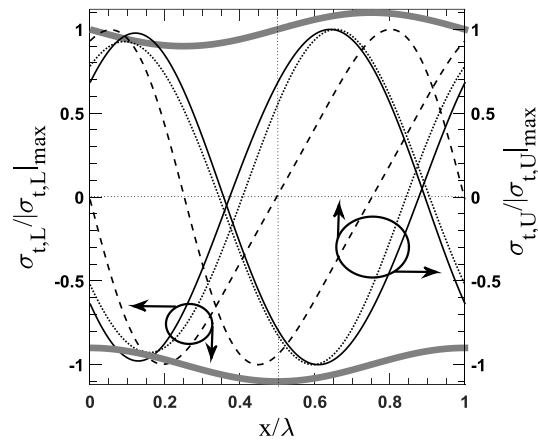
Figure 3.18: Variations of tangential stresses acting at the lower ($\sigma_{t,L}$) and upper ($\sigma_{t,U}$) plates as functions of x for $Ra = 200$, $y_b = y_t = 0.05$, $\alpha = 0.1$ (dotted lines), $\alpha = 1.53$ (solid lines) and $\alpha = 5$ (dashed lines) for $\Omega_C = \pi/2$.

Figure 3.18 displays a typical distribution of the tangential stress acting on the plates. These distributions are very similar for all α's and for all Ω_C's i.e. the shear is directed towards the corrugation peak and, thus, it would contribute to the corrugation build up if such an effect was permitted. Distributions of the *y*-component of pressure forces have different form at the lower and upper plates (Fig.3.19). Their net effect can be assessed by evaluating $Dif_{1,L}$ and $Dif_{1,U}$ (see Eq.3.5.12). At the lower plate, the pressure maxima generally occur at the corrugation troughs except for medium α's where the maxima occur at the corrugation peaks but only if the phase difference is not too close to $\Omega_C = \pi$. Pressure contributes to the corrugation build up at the lower plate when $Dif_{1,L} > 0$. Results displayed in Fig.3.20 demonstrate that this occurs only for a finite range of medium α's, for *Ra*'s which are large enough and for corrugation amplitudes which are small enough. Distributions of pressure forces at the upper plate have maxima always overlapping with the troughs which lead to $Dif_{1,U} < 0$ and, as a result, these forces would always contribute to the corrugation built up if such an effect was allowed.
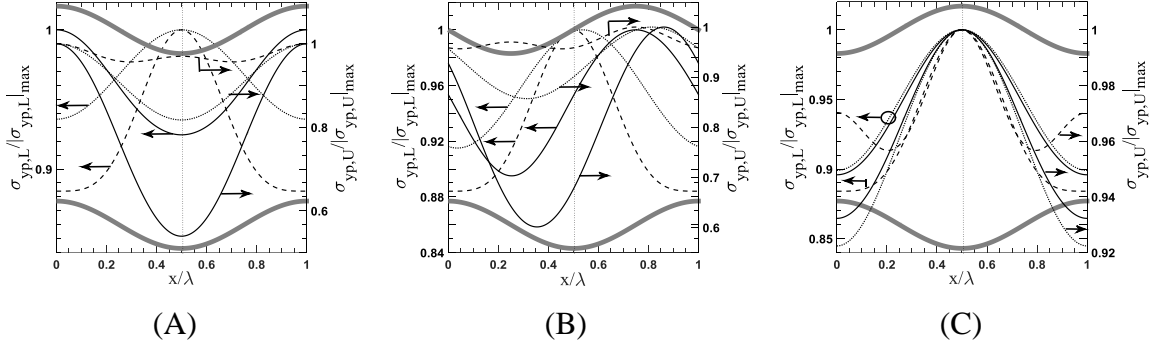
Figure 3.19: Variations of the y-component of forces acting at the lower ($\sigma_{yp,L}$) and upper ($\sigma_{yp,U}$) plates as functions of x for $Ra = 200$, $y_b = y_t = 0.05$, $\alpha = 0.1$ (dotted lines), $\alpha = 1.53$ (solid lines) and $\alpha = 5$ (dashed lines) for $\Omega_C = 0$ (Fig.3.19A), $\Omega_C = \pi/2$ (Fig.3.19B) and $\Omega_C = \pi$ (Fig.3.19C).
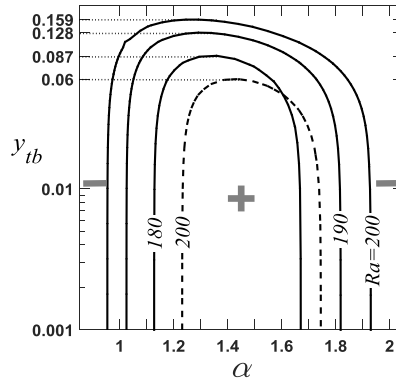
Figure 3.20: Contour plots of $Dif_{1,L} = 0$ (see Eq. (3.5.12)) in the (α, y_{tb})-plane for $y_t = y_b = y_{tb}$ and $\Omega_C = 0, \pi$ (solid and dashed lines, respectively).

To illustrate the magnitude of various forces, consider $Ra = 200$, air as the working fluid and the reference temperature $T_U^* = 20°C$ which result in the following material properties: $v^* = 1.511 * 10^{-5}\, m^2/s$, $k^* = 0.0257\, W/(m\,K)$, $c^* = 1005\, J/(kg\,K)$, $\kappa^* = 2.12 * 10^{-5}\, m^2/s$, $\Gamma^* = 3.43 * 10^{-3} 1/K$, $\rho^* = 1.205\, kg/m^3$. Substitution of this information as well as the numerical value of g into definition of Ra results in a relation between the mean temperature difference θ_s^* and the slot half-height h^* of the form $\theta_s^* * h^{*3} = 1.9 * 10^{-6}$. Use of slot with heights $h^* = 0.1, 0.01, 0.005, 0.004$ leads to temperature differences $\theta_s^* = 0.0019, 1.9, 15.23, 29.75$, respectively. Computations carried out for $\alpha = 1.53$, $\Omega_c = \pi/2$ and $y_b = y_t = 0.05$ give forces $F_{xv,L}^* = 3.65 *$

$10^{-10}N$ and $F^*_{xp,L} = 5.11 * 10^{-10}N$ acting per slot segments of length of $\lambda^* = 0.4107$, 0.0410, 0.0205, 0.0164 m, respectively, and unit width. These forces increase to $F^*_{xv,L} = 9.71 * 10^{-10}, 1.63 * 10^{-9}, F^*_{xp,L} = 1.38 * 10^{-9}, 2.37 * 10^{-9}$ when corrugation height is increases to $y_b = y_t = 0.1, 0.15$, respectively.

The Nusselt number strongly depends on Ω_C with the largest heat flow corresponding to the "wavy" configuration ($\Omega_C = 0$) and the smallest corresponding to the "converging-diverging" configuration ($\Omega_C = \pi$), as illustrated in Fig.3.21. The range of variations of Nu_{av} increases significantly with an increase of Ra (see Fig.3.21).

It is convenient to start discussion of Nu_{av} dependence on the slot geometry by looking at the limit of $y_t \to 0$, $y_b \to 0$ which gives $Nu_{av} \to Ra/2$. Results displayed in Fig.3.22A illustrate variations of the heat flow above the smooth slot limit, i.e. $\frac{Nu_{av}}{Ra} - \frac{1}{2}$. The limit of this quantity for $\alpha \to 0$ determined using solution from Section 5.1 has the form

$$\lim_{\alpha \to 0} \left(\frac{Nu_{av}}{Ra} - \frac{1}{2} \right) = \frac{1}{2} \left\{ \frac{1}{\left(\left(1 - \left(\frac{y_b}{2}\right)^2 - \left(\frac{y_t}{2}\right)^2 + \frac{y_b y_t \cos\Omega_C}{2} \right)^{\frac{1}{2}} \right)} - 1 \right\} \approx \frac{y_b^2 + y_t^2 - 2 y_b y_t \cos\Omega_C}{16},$$

(5.15)

i.e. it shows a strong dependence on Ω_C. To illustrate this point, evaluate (3.5.15) for $y_b = y_t$ and a few characteristic values of Ω_C, i.e.

$$\Omega_C = 0 : \quad \frac{Nu_{av}}{Ra} - \frac{1}{2} \approx \frac{(y_b - y_t)^2}{16} = 0,$$

$$\Omega_C = \pi/2 : \quad \frac{Nu_{av}}{Ra} - \frac{1}{2} \approx \frac{y_b^2 + y_t^2}{16} = \frac{y_b^2}{8} = 3.12 * 10^{-4},$$

$$\Omega_C = \pi : \quad \frac{Nu_{av}}{Ra} - \frac{1}{2} \approx \frac{(y_b + y_t)^2}{16} = \frac{y_b^2}{4} = 6.25 * 10^{-4}.$$

(5.16)

Equations (3.5.16) show that the heat transfer for $\alpha \to 0$ can be either larger or equal to that in a smooth slot depending on the phase difference. This conclusion is well

illustrated in Fig.3.22A which shows that $\frac{Nu_{av}}{Ra} - \frac{1}{2}$ either approaches an amplitude-dependent constant or decreases to zero as $\alpha \to 0$ depending on the value of Ω_C. An increase of α away from this limit increases the heat flow mainly due to an increase of the corrugation-driven conductive effects. At $\alpha \approx 0.4$ convective effects begin to play a role and the heat flow increases above that expected from the pure conduction, but only if Ω_C is not too close to π as convective effects play nearly no role for the "converging-diverging" configuration. The convective effects peak at $\alpha \approx 1.53$ for all Ω_C's which are not too close to π and then they rapidly decrease with the heat flow being again dominated by the conduction and with its increase resulting from the corrugation-driven changes in the conduction. The upper limit on this growth corresponds to conduction in a slot whose height has been reduced by half of the corrugations' amplitudes, i.e. $\lim_{\alpha \to \infty} Nu_{cond,av} = \frac{Ra}{(2-y_b-y_t)}$. The variations of the convective effects are well illustrated in Fig.3.22B. These effects need to be accounted for only Ω_C's which are not too close to π and only for a range of medium α's as they decrease as α^4 when $\alpha \to 0$ and as α^{-7} when $\alpha \to \infty$. The dependence of the heat transfer modifications on the corrugation amplitude is illustrated in Fig.3.22C. Nu_{av} increases away from the smooth- slot limit of $Ra/2$ proportionally to y_{tb}^2 for all Ω_C's with Nu_{av} for $\Omega_C \approx \pi$ being at least two orders of magnitude smaller than Nu_{av} for $\Omega_C \approx 0$. This growth begins to saturate when the amplitude becomes excessively large as illustrated in Fig.3.22C with the earliest saturation occurring for $\Omega_C \approx 0$ which corresponds to the strongest convection. Results displayed in Fig.3.22D demonstrate that the convective heat flow initially increases proportionally to Ra^3 with this growth rapidly accelerating when Ra approaches the critical value which gives rise to transition to a secondary state in a smooth slot.

Distributions of the local convective and conductive Nusselt numbers displayed in Fig.3.23 demonstrate that the conductive heat flux is directed from the lower to the upper corrugation peaks while the convective heat flux is directed from the lower to the upper corrugation troughs. The direction of the convective heat flux changes for small enough and large enough α's as it is directed from the lower to the upper corrugation peaks, similarly as in the case of only one plate being corrugated (see Section 3.2).
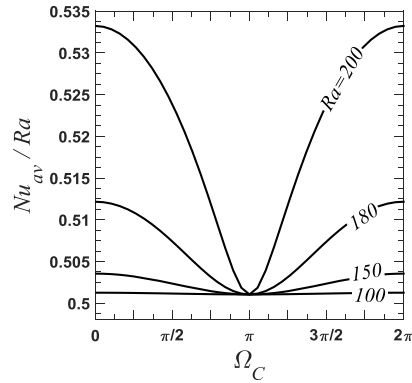
Figure 3.21: Variations of the average Nusselt number Nu_{av} as a function of the phase shift Ω_C for $y_t = y_b = 0.05$, $\alpha = 1.53$.
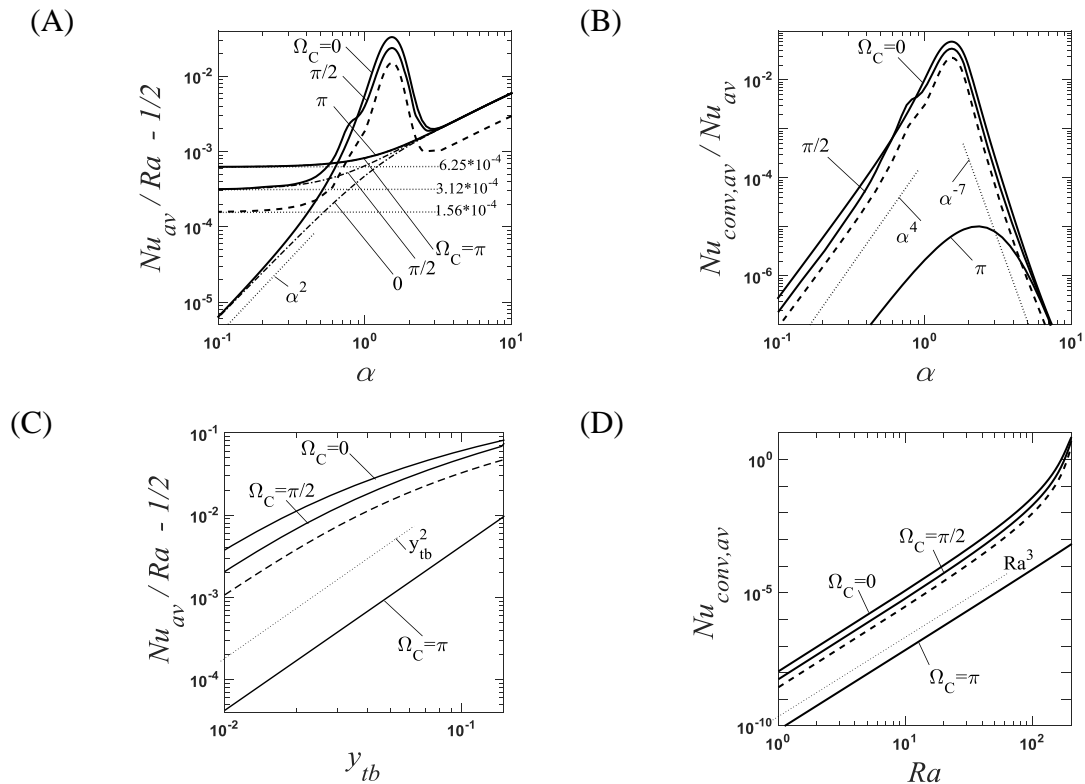
Figure 3.22: Variations of the excess heat flow due to corrugation $\frac{Nu_{av}}{Ra} - 1/2$ (Fig.3.22A) and the ratio of the average convective and the average Nusselt numbers $Nu_{conv,av}/Nu_{av}$ (Fig.3.22B) as functions of the wave number α for $Ra = 200$, $y_b = y_t = 0.05$ and $\Omega_C = 0, \frac{\pi}{2}, \pi$; variations of the excess heat flow due to corrugation $\frac{Nu_{av}}{Ra} - 1/2$ as a function $y_{tb} = y_b = y_t$ for $\alpha = 1.53$, $Ra = 200$, $\Omega_C = 0, \frac{\pi}{2}, \pi$ (Fig.3.22C) and variations of $Nu_{conv,av}$ as a function of Ra for $\alpha = 1.53$, $y_b = y_t = 0.05$, $\Omega_C = 0, \frac{\pi}{2}, \pi$ (Fig.3.22D). Thin dotted lines represent asymptotes. Dashed lines correspond to the corrugation at the lower plate only. Dashed-dotted lines in Fig.22A describe the conductive effects; the dashed-dotted and solid lines overlap for $\Omega_C = \pi$.
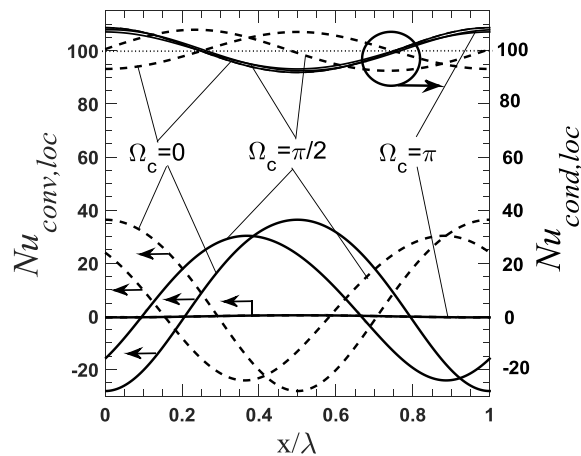
Figure 3.23: Variations of the local convective ($Nu_{conv,loc,L}$, $Nu_{conv,loc,U}$) and conductive ($Nu_{cond,loc,L}$, $Nu_{cond,loc,U}$) Nusselt numbers at the lower (solid lines) and upper (dashed lines) plates as functions of x for $Ra = 200$, $y_b = y_t = 0.05$, $\alpha = 1.53$ and $\Omega_C = 0, \frac{\pi}{2}, \pi$. Lines for $Nu_{cond,loc,U}$ and $Nu_{cond,loc,L}$, and for $Nu_{conv,loc,L}$ and $Nu_{conv,loc,U}$ overlap when $\Omega_C = \pi$.

3.6. Effects of the Prandtl number

Results presented in the previous sections have been obtained for $Pr = 0.71$. As convection is driven by the horizontal temperature gradients which are dominated by conductive effects, one should expect increase of convection intensity as Pr is reduced. Results displayed in Fig. 3.24A confirm this prediction. The most intense convection occurs for $\alpha \approx 1.53$ and it decreases for $\alpha \to 0$ and for $\alpha \to \infty$ always in the same manner regardless of the value of Pr as illustrated in Fig.3.24B. The heat transfer process displays the same characteristics with conduction dominating its increase above the smooth-slot limit for both small and large α's and convection dominating this increase for $\alpha = 0(1)$, as illustrated in Fig.3.25A. The increase of Pr leads to larger convective corrections as convective transport becomes stronger than the conductive transport. This process is well illustrated in Fig.3.25B displaying variations of Nu_{av} as a function Pr. $Nu_{cond,av}$ does not depend on Pr while $Nu_{conv,av}$ changes significantly. The convective part becomes stronger as Pr increases and reaches the limiting state for $Pr > 1$.

(A) (B)
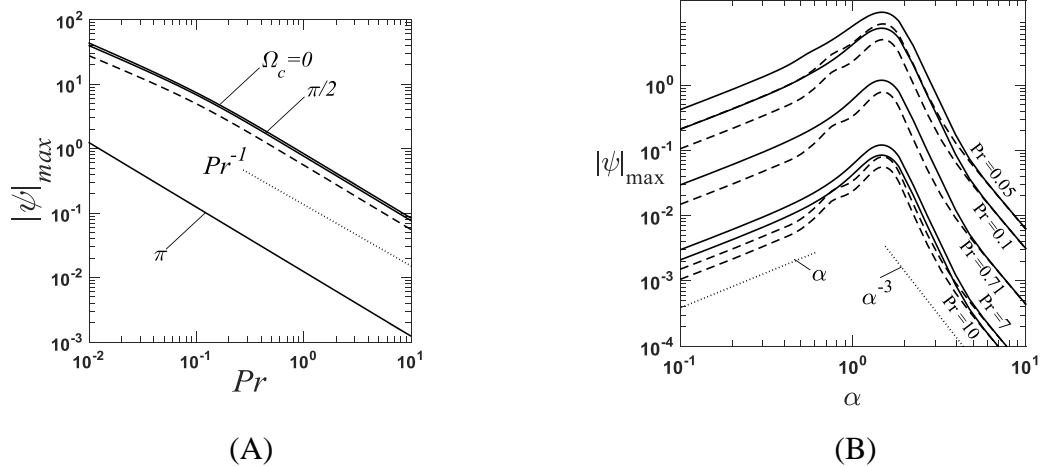
Figure 3.24: Variations of the maximum of the stream function $|\psi|_{max}$ as a function of Pr (Fig.3.24A) for $\Omega_C = 0, \pi/2, \pi$, $y_t = y_b = 0.05$, $Ra = 200$, and as a function of α (Fig.3.24B) for $y_t = y_b = 0.05$, $\Omega_C = 0$, $Ra = 200$. The dashed lines correspond to the lower plate corrugated with $y_t = 0$, $y_b = 0.05$. Dotted lines identify asymptotes.

(A) (B)
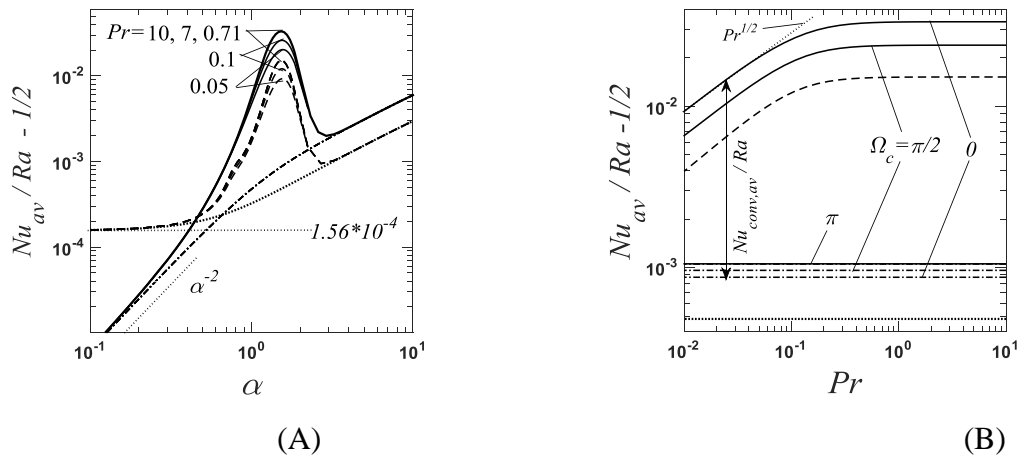
Figure 3.25: Variations of the average Nusselt number Nu_{av} as a function of α (Fig.3.25A) and as a function of Pr (Fig.3.25B). Results displayed in Fig.3.25A are for both plates being corrugated with $y_t = y_b = 0.05$, $\Omega_C = 0$, $Ra = 200$ (solid lines) and include the conductive Nusselt number $Nu_{cond,av}$ (dashed-dotted line).The same figure displays variations of Nu_{av} (dashed lines) and $Nu_{cond,av}$ (dotted line) for the lower plate corrugated with $y_t = 0$, $y_b = 0.05$. Results displayed in Fig.3.25B are for both plates being corrugated with $y_t = y_b = 0.05$, $\Omega_C = 0, \frac{\pi}{2}, \pi$, $Ra = 200$, $\alpha = 1.53$ (solid lines) and include $Nu_{cond,av}$ (dashed-dotted lines). Lines for Nu_{av} and $Nu_{cond,av}$ overlap when $\Omega_C = \pi$. The same figure displays variations of Nu_{av} (dashed lines) and $Nu_{cond,av}$ (dotted line) for the lower plate corrugated with $y_t = 0$, $y_b = 0.05$. Thin dotted lines identify asymptotes.

3.7. Summary

Analysis of natural convection in a horizontal slot formed by two corrugated, isothermal plates has been carried out under subcritical heating conditions. The corrugations have the form of sinusoidal grooves and can be placed either at the lower plate, or at the upper plate or at both plates. It has been shown that corrugations create horizontal temperature gradients which lead to the formation of vertical and horizontal pressure gradients which drive the motion regardless of the intensity of the heating. Convection has the form of pairs of counter-rotating rolls.

The most intense convection occurs at wave number $\alpha \approx 1.53$. The intensity of convection initially increases proportionally Ra and then its growth rapidly accelerates when Ra approaches conditions giving rise to secondary flows in smooth slots. An increase of the corrugation amplitude results in an increase of the convection intensity proportionally to the amplitude but the system begins to saturate and the growth slows down when an excessively large amplitude is reached. Placement of corrugations on both plates may either significantly increase or decrease the convection intensity depending on the phase shift between both corrugation systems. The most intense convection results from the phase shift $\Omega_c = 0$ ("wavy" slot), and the weakest convection corresponds to $\Omega_c = \pi$ ("converging-diverging" slot). Reduction of the Prandtl number increases the strength of convection proportionally to Pr^{-1}.

The presence of the corrugation affects the conductive heat transfer as well as it creates convection-driven heat flow. The conductive heat transfer increases with an increase of the corrugation wave number; this growth is limited from above in the limit of $a \to \infty$. by conduction in a smooth slot whose height is reduced by half of the corrugation amplitude. The convective part of the heat flow is relevant only for $a = 0(1)$ as it rapidly decreases in the limits of $a \to 0$ and $a \to \infty$. The most effective corrugation wave number as far as maximization of the heat flow is concerned is $\alpha \approx 1.53$. Convection also creates forces acting on the plates. Conditions under which these forces act in a

manner which results in the growth of corrugation have been identified assuming that either erosion or surface deformations are allowed.

Chapter 4

Conclusion and Recommendations

4.1 Conclusions

Natural convection in a horizontal slot bounded by corrugated isothermal plates has been studied. A mathematical model based on the Boussinesq approximation has been used to describe fluid movement. This model involves two transport parameters, e.g. the Rayleigh number and the Prandtl number. Corrugations with simple sinusoidal shapes have been considered. Such corrugations are fully parametrized in terms of the corrugation wave number and the corrugation amplitude.

The presence of corrugations results in an irregular solution domain and this necessitates development of the proper solution methodologies. A grid-less, spectrally-accurate algorithm based on Immersed Boundary Conditions (IBC) concept has been developed. The algorithm uses Fourier expansions in the horizontal direction and Chebyshev expansions in the vertical direction. The field equations have been discretized using a regular, rectangular computational domain with the irregular flow domain placed inside the computational domain. The Galerkin procedure has been used to construct the relevant algebraic equations. Constraints have replaced the flow and thermal boundary conditions. The Tau procedure has been used for their inclusion in the discretized problem. The solution procedure relies on the iterative process with the nonlinear terms taken from the previous iteration resulting in a first order fixed-point method. The iterative process consists of solving the energy equation followed by solution of the flow equations. An efficient solver has been developed for solution of the linear algebraic systems arising during each iteration step. Numerous tests confirm the spectral accuracy of the solution. Limitations of the algorithm have been discussed and correlated with the severity of the geometry. A method for extension of the algorithm to more extreme geometries using the over-determined formulation has been presented. The discretization process results in an algorithm capable of determination of the flow and temperature

fields for any combinations of the geometric parameters without the need to construct any grids and, thus, it is suitable for use in geometry optimization problems.

The analysis of convection has been focused on the so-called subcritical heating conditions, i.e. conditions which do not result in transition to secondary convection. Corrugations have been placed either at the lower plate or the upper plate, or at both plates. The slot geometry has been parametrized in terms of the corrugation wave number α, the upper (y_t) and lower (y_b) corrugation amplitudes and the phase shift Ω_c between the upper and lower corrugation systems. It has been shown that corrugations create horizontal temperature gradients that lead to the formation of vertical and horizontal pressure gradients which drive the motion regardless of the intensity of the heating. Convection has the form of pairs of counter-rotating rolls whose size is dictated by the corrugation wavelength. Rolls fill in the slot completely except for the short wavelength corrugations where the motion is confined to a thin layer adjacent to the corrugated plate.

When the corrugation is placed at the lower plate, the most intense convection occurs for the corrugation wavelengths comparable to the slot height. The intensity of convection rapidly decreases as the corrugation wavelength is either increased or decreased away from its optimum. It has been found that the optimal wavelength corresponds to $\alpha \approx 1.53$ regardless of the Rayleigh number Ra, the Prandtl number Pr and the corrugation amplitude. The intensity of convection initially increases proportionally Ra and then its growth rapidly accelerates when Ra approaches conditions giving rise to secondary flows in smooth slots. An increase of the corrugation amplitude results in an increase of the convection intensity proportionally to the amplitude but the system begins to saturate and the growth slows down when an excessively large amplitude is used. Transfer of the corrugation to the upper plate results in a similar convection whose properties can be deduced from the properties of convection occurring when the corrugation is placed at the lower plate. Placement of corrugations on both plates may either significantly increase or decrease the convection intensity depending on the phase shift between both corrugation systems. The most intense convection results from the phase shift $\Omega_c = 0$ ("wavy" slot) and it is almost twice as strong as convection driven by corrugation placed

at just one plate, and the weakest convection corresponds to $\Omega_c = \pi$ ("converging-diverging" slot). The latter convection is very weak and has no practical significance. Reduction of the Prandtl number increases the strength of convection proportionally to Pr^{-1}.

Convection creates forces acting on the plates. It has been shown that the shear forces would always attempt to build up the corrugation while the role of the pressure forces depends on the corrugation wave number, the corrugation amplitude and position of the corrugation either at the lower or upper plate. When the upper plate is corrugated, pressure always contributes to the plate flattening. When the lower plate is corrugated, pressure generally contributes to the flattening except for a range of $\alpha = 0(1)$ which must be combined with a sufficiently small corrugation amplitude and a sufficiently large Rayleigh number. The built up of the corrugations is likely to occur under such conditions as both pressure and shear act in the same manner. When both plates are corrugated, the horizontal forces create a moment which attempts to change plates' relative position. There are two states of equilibria corresponding to the elimination of this moment, i.e. the "wavy" slot and the "converging-diverging" slot. The latter one is unstable as small departures from this state create a moment which attempts to change the relative position of the plates until the "wavy" configuration is reached.

The presence of corrugation affects the conductive heat transfer and also creates convection-driven heat flow. The former increases with an increase of the corrugation wave number; this growth is limited from above in the limit of $\alpha \to \infty$ by conduction in a smooth slot whose height is reduced by half of the corrugation amplitude. The convective part of the heat flow is relevant only for $\alpha = 0(1)$ as it rapidly decreases in the limits of $\alpha \to 0$ and $\alpha \to \infty$. The most effective corrugation wave number as far as maximization of the heat flow is concerned is $\alpha \approx 1.53$. The magnitude of the heat flow may change by an order of magnitude depending on the corrugation phase shift. The maximum heat flow occurs in the "wavy" slot while the minimum heat flow corresponds to the "converging-diverging" slot. The additional heat flow associated with the introduction of the corrugation is of the order of 5% of the heat flow in a smooth slot.

4.2 Recommendations for future work

This thesis considers only the primary convection, i.e. convection which occurs when the Rayleigh number is not too large. It is expected that when the heating intensity reaches a certain critical magnitude, the system may go through transition to a secondary state. Both the form of such secondary convection as well as conditions leading to its onset are not known and should be investigated.

This thesis considers only corrugations of sinusoidal shape. The convection properties associated with other corrugation shapes are not known and should be investigated. It is of interest to determine if an optimal corrugation shape exists. The shape which leads to the most intense convection is considered optimal.

Finally, this thesis considers just the two-dimensional corrugations. It would be of interest to determine the form of convection associated with the three-dimensional corrugations as such are most likely to occur in nature.

References

Abtahi, A., Hossain, M. Z., and Floryan, J. M., 2016, Spectrally Accurate Algorithm for Analysis of Convection in Corrugated Conduits, Journal of Computers and Mathematics with Applications 72, 2636–2659.

Ahlers, G., Grossmann, S., and Lohse, D., 2009, Heat Transfer and Large Scale Dynamics in Turbulent Rayleigh–Bénard Convection, Rev. Mod. Phys. 81, 503–537.

Asgarian, A. , Hossain, M. Z., and Floryan, J. M., Rayleigh-Bénard Convection Driven by a Long Wavelength Heating, To appear in J. of Theoretical and Computational Fluid Mechanics.

Beltrame, P., Knobloch, E., Hänggi, P.,and Thiele, U., 2011, Rayleigh and Depinning Instabilities of Forced Liquid Ridges on Heterogeneous Substrates, Phys. Rev. E 83, 016305.

Bénard, H., 1900, Les tourbillons cellulaires dans une nappe liquide, Revue Générale Science Pure et Applique 11, 1261-1271.

Bergles A. E., 1998, Handbook of Heat Transfer, McGraw-Hill, New York, NY, USA, 3rd edition.

Bergles, A. E., 2001, The implications and challenges of enhanced heat transfer for the chemical process industries, Chemical Engineering Research and Design 79, 437–444.

Bodenschatz, E., Pesch, W. and Ahlers, G., 2000, Recent developments in Rayleigh-Benard convection, Ann. Rev. Fluid Mech. 32, 709-778.

Cabal, A., Szumbarski, J., and Floryan, J. M., 2001, Numerical simulation of flows over corrugated walls, Comp. & Fluids 30, 753–776.

Canuto, C., Hussaini, M. Y., Quarteroni, A., and Zang, T. A., 2006, Spectral Methods: Fundamentals in single domains, Springer-Verlag, Berlin Heidelberg.

Chandrasekhar, S., 1961, Hydrodynamic and Hydromagnetic Stability, Oxford University Press.

Chilla, F., and Schumacher, J., 2012, New Perspectives in Turbulent Rayleigh–Bénard Convection, Eur. Phys. J. E. 35, 58–82.

Choi, K. S., and Orchard, D., 1997, Turbulence management using riblets for heat and momentum transfer, Exp. Thermal Fluid Sci. 15, 109–124.

Del Rey Fernandez, D. C., Husain, S. Z., and Floryan, J. M., 2010, Immersed boundary conditions method for heat conduction problems in slots with time-dependent geometry, Int. J. Numer. Meth. Fluids 67, 478–500.

Deng, J., Shao, X. M., and Ren, A. L., 2006, A new modification of the immersed-boundary method for simulating flows with complex moving boundaries, Int. J. of Num. Meth. Fluids 52, 1195–1213.

Dewan, A., Mahanta, P., Sumithra Raju, K., and Suresh Kumar, P. , 2004, Review of passive heat transfer augmentation techniques, Proceedings of the Institution of Mechanical Engineers, Part A, J. Power and Energy 218, 509-527.

Finney, M. A., Cohen, J. D., McAllister, S. S., and Jolly, W. M., 2012, On the Need for a Theory of Wildland Fire Spread, International Journal of Wildland Fire, CSIRO Publishing, dx.doi.org/10.1071/WF11117.

Floryan, D., and Floryan, J. M., 2015, Drag reduction in heated channels, J. Fluid Mech. 765, 353-395.

Floryan, J. M., 1986, Conformal-mapping-based coordinate generation for flows in periodic configurations, J. Comp. Phys. 62, 221–247.

Floryan, J. M., and Zemach, C., 1987, Schwarz-Christoffel transformations - a general approach, J. Comp. Phys. 72, 347–371.

Floryan, J. M., and Rasmussen, H., 1989, Numerical analysis of viscous flows with free surfaces, Appl. Mech. Rev. 42, 323–341.

Floryan, J. M., and Zemach, C., 1993, Schwarz-Christoffel methods for conformal mappings of regions with a periodic boundary, J. Comp. Applied Math 46, 77–102.

Floryan, J. M., 2007, Three-dimensional instabilities of laminar flow in a rough channel and concept of hydraulically smooth wall, Eur. J. Mech. B/Fluids 26, 305-329.

Freund, G., Pesch, W., and Zimmermann, W., 2011, Rayleigh–Bénard Convection in the Presence of Spatial Temperature Modulations, J. Fluid Mech. 673, 318–348.

Gamrat, G., Favre-Marinet, M., Le Person, S. , Bavière, R. , Ayela, F., 2008, An experimental study and modelling of roughness effects on laminar flow in microchannels, J. Fluid Mech. 594, 399–423.

Glimm, J., Grove, J. W., Li, X. L., Shyue, K. M., Zeng, Y., and Zhang, Q., Three-dimensional front tracking, SIAM J. Sci. Computing 19, 703–727.

Hamed, M., and Floryan, J. M., 1998, Numerical simulation of unsteady nonisothermal capillary interfaces, J. Comp. Phys. 145, 110–140.

Harlow, F. H., and Welch, J. E., 1966, Numerical study of large amplitude free surface motions, Phys. Fluids 9, 842–851.

Herwig, H., Gloss, D., and Wenterodt, T., 2008, A new approach to understanding and modelling the influence of wall roughness on friction factors for pipe and channel flows, J. Fluid Mech. 613, 35–53.

Hirt, C. W. , and Nichols, B. D., 1981, Volume of fluid (VOF) method for the dynamics of free boundaries, J. Comp. Phys. 39, 201–225.

Hossain, M. Z., and Floryan, J. M., 2013a, Instabilities of Natural Convection in a Periodically Heated Layer, J. Fluid Mech. 733, 33-67.

Hossain, M. Z., and Floryan, J. M., 2013b, Heat Transfer due to Natural Convection in a Periodically Heated Slot, ASME Journal of Heat Transfer 135, 022503.

Hossain, M. Z., and Floryan, J. M., 2014, Natural Convection in a Fluid Layer Periodically Heated from Above, Physical Review E 90, 023015.

Hossain, M. Z., and Floryan, J. M., 2015a, Mixed Convection in a Periodically Heated Channel, J. Fluid Mech. 768, 51-90.

Hossain, M. Z., and Floryan, J. M., 2015b, Natural Convection in a Horizontal Fluid Layer Periodically Heated from Above and Below, Phys. Rev. E 92, 02301.

Hughes, G. O., and Griffiths, R.W., 2008, Horizontal Convection, Ann. Rev. Fluid Mech. 40, 185–208.

Husain, S. Z., and Floryan, J. M., 2007, Immersed boundary conditions method for unsteady flow problems described by the Laplace operator, Int. J. Numer. Meth. Fluids 56, 1765–1786.

Husain, S. Z., and Floryan, J. M., 2008, Implicit spectrally-accurate method for moving boundary problems using immersed boundary conditions concept, J. Comp. Phys. 227, 4459–4477.

Husain, S. Z., Floryan, J. M., and Szumbarski, J., 2009, Over-determined formulation of the immersed boundary conditions method, Comput. Methods Appl. Mech. Engrg. 199, 94–112.

Husain, S. Z., and Floryan, J. M., 2010, Spectrally-Accurate Algorithm for Moving Boundary Problems for the Navier-Stokes Equations, J. Comp. Phys. 229, 2287-2313.

Husain, S. Z., and Floryan, J. M., 2013, Effective solvers for the immersed boundaries method, Computers & Fluids 84, 127–140.

Husain, S. Z., and Floryan, J. M., 2014, Efficient over-determined implementation of the immersed boundary conditions method, Computers & Fluids 105, 194–203.

Hyman, J. M., 1984, Numerical methods for tracking of interfaces, Physica 12D, 396–407.

Jacobi, A. M., and Shah, R. K., 1998, Air-side flow and heat transfer in compact heat exchangers: A discussion of enhancement mechanisms, Heat Transfer Eng. 19, 29-41.

Kim, J., Kim, D., and Choi, H., 2001, An immersed boundary finite-volume method for simulation of flows in complex geometries, J. Comp. Phys. 171, 132–150.

Krishnan, M., Ugaz, V. M., and Burns, M. A., 2002, PCR in a Rayleigh-Bénard Convection Cell, Science, 298, 793.

Lenardic, A., Moresi, L., Jellinek, A. M., andManga, M., 2005, Continental insulation, mantle cooling, and the surface area of oceans and continents, Earth Planet. Sci. Lett. 234, 317–333.

Lograni, P. M., Oliviera, M. M., and Blaskovich, T., 2003, Comparison of heat transfer augmentation techniques, AIAA J. 41, 337-362.

Lohse, D., and Xia, K. Q., 2010, Small-scale properties of turbulent Rayleigh–Bénard convection, Annu. Rev. Fluid. Mech. 42, 335–364.

Marcq, S., and Weiss, J., 2012, Influence of sea ice lead-width distribution on turbulent heat transfer between the Ocean and the Atmosphere, Cryosphere 6, 143–156.

Maxworthy, T., 1997, Convection into Domains with Open Boundaries, Annu. Rev. Fluid. Mech. 29, 327–71.

McCoy, J. H., Brunner, W., Pesch, W., and Bodenschatz, E. ,2008, Self-Organization of Topological Defects due to Applied Constraints, Phys. Rev. Lett. 101, 254102.

Mittal, R., Iaccarino, G., 2005, Immersed boundary methods, Annu. Rev. Fluid Mech. 37, 239–261.

Nicolas, X., 2002, Bibliographical review on the Poiseuille-Rayleigh-Bénard flows: the mixed convection flows in horizontal rectangular ducts heated from below, International Journal of Thermal Sciences, 71, 961-1016.

Peskin, C. S., 2002, The immersed boundary method, Acta Numerica 11, 479–517.

Rayleigh, J. W. S., 1916, On convection currents in a horizontal layer of fluid, when the higher temperature is on the under side, Phil. Mag. 32, 529-546.

Ripesi, P., Biferale, L., Sbragaglia, M., and Wirth, A., 2014, Natural convection with mixed insulating and conducting boundary conditions: low- and high-Rayleigh-number regimes, J. Fluid Mech. 742, 636-663.

Rizwam, A. M., Dennis, L. Y.C, and Liu, C., 2008, A review on the generation, determination and mitigation of urban heat island, J. Environmental Sci. 20, 120-128.

Seiden, G., Weiss, S., McCoy, J. H., Pesch, W., and Bodenschatz, E., 2008, Pattern forming system in the presence of different symmetry-breaking mechanisms, Phys. Rev. Lett. 101, 214503.

Sethian, J. A., 1999, Level set methods and fast marching methods: evolving interfaces in computational geometry, Fluid Mechanics, Computer Vision and Materials Science, Cambridge University Press.

Sethian, J. A., and Smereka, P., 2003, Level set methods for fluid interfaces, Ann. Rev. Fluid Mech. 35, 341–372.

Siddique, M., Khaled, A. R. A., Abdulhafiz, N. I., and Boukhary, A. Y., 2010, Recent advances in heat transfer enhancements: A review report, Int. J. Chemical Engineering 1-28.

Siggers, J. H., Kerswell, R. R., and Balmforth, N. J., 2004, Bounds on horizontal convection, J. Fluid Mech. 517, 55–70.

Sobhan, C. B., and Garimella, S. V., 2001, A comparative analysis of studies on heat transfer and fluid flow in microchannels, Microscale Thermophysical Engineering 5, 293-311.

Stalio, E., and Nobile, E., 2003, Direct numerical simulation of heat transfer over riblets, Int. J. Heat Fluid Flow 24, 356–371.

Szumbarski, J., and Floryan, J. M., 1999, A direct spectral method for determination of flows over corrugated boundaries, J. Comp. Phys. 153, 378–402.

Taira, K., and Colonius, T., 2007, The immersed boundary method: a projection approach, J. Comp. Phys. 225, 2118–2137.

Weiss, S., Seiden, G., and Bodenschatz, E., 2012, Pattern Formation in Spatially Forced Thermal Convection, New Journal of Physics 14, 053010.

Winters, K. B., and Young, W. R., 2009, Available Potential Energy and Buoyancy Variance in Horizontal Convection, J. Fluid Mech. 629, 221–230.

Xia, G., Chai, L., Zhou, M., and Wang, H., 2011, Effects of structural parameters on fluid flow and heat transfer in a microchannel with aligned fan-shaped reentrant cavities, Int. J. Thermal Sciences 50, 411-419.

Appendices

Appendix A. Evaluation of the inner products of Chebyshev polynomials and their derivatives, and evaluation of the integrals of Chebyshev polynomials.

Chebyshev polynomials satisfy the following relations

$$T_0(y) = 1, \ T_1(y) = y, \ T_{k+1}(y) = 2yT_k(y) - T_{k-1}(y) \quad \text{for } k \geq 2, \tag{A.1a}$$

$$D^n T_{k+1}(\hat{y}) = 2nD^{n-1}T_k(\hat{y}) + 2\hat{y}D^n T_k(\hat{y}) - D^n T_{k-1}(\hat{y}) \qquad \text{for} \quad n \geq 1. \tag{A.1b}$$

The inner product of two Chebyshev polynomials is defined as

$$\langle T_j(\hat{y}), T_k(\hat{y}) \rangle = \int_{-1}^{1} T_j(\hat{y})T_k(\hat{y}) \, \omega(\hat{y})d\hat{y}, \tag{A.2}$$

where $\omega = (1 - \hat{y}^2)^{-1/2}$ is the weight function. Its evaluation results in

$$\langle T_j, T_k \rangle = \frac{\pi}{2} C_k \delta_{ik} \begin{cases} 0 & \text{for} & j \neq k \\ \pi & \text{for} & j = k = 0 \\ \pi/2 & \text{for} & j = k > 0 \end{cases}, \tag{A.3}$$

where $\delta_{i,k}$ is the Kronecker delta and $C_k = \begin{cases} 2, & k = 0 \\ 1, & k \geq 1 \end{cases}$.

The first, second, and forth derivatives of a Chebyshev polynomial can be expressed in terms of the Chebyshev polynomials as follows:

$$DT_k = 2k \sum_{l=0}^{l=k-1} \frac{1}{C_l} T_l, \ k - l = odd, \ k \geq i + 1, \tag{A.4a}$$

$$D^2 T_k = \sum_{l=0}^{l=k-2} \frac{1}{C_l} k(k^2 - l^2)T_l, \ k - l = even, \ k \geq l + 2, \tag{A.4b}$$

$$D^3 T_k = \sum_{l=0}^{l=k-2} \frac{1}{c_l} k(k^2 - l^2) \left[2l \sum_{z=0}^{z=l-1} \frac{1}{c_z} T_z \right],$$

$$k - l = even, l - z = odd, \quad k \geq l + 2, l \geq z + 1, \tag{A.4c}$$

$$D^4 T_k = \sum_{l=0}^{l=k-2} \frac{1}{c_l} k(k^2 - l^2) D^2 T_l, \quad k - l = even, \ k \geq l + 2. \tag{A.4c}$$

The inner products of the derivatives of the Chebyshev polynomials and the Chebyshev polynomials by themselves can be evaluated explicitly resulting in the following relations

$$\langle T_j, DT_k \rangle = k\pi, \qquad\qquad \text{for} \quad k - j = odd, \ k \geq j + 1, \tag{A.5a}$$

$$\langle T_j, D^2 T_k \rangle = k(k^2 - j^2)\frac{\pi}{2}, \qquad\qquad \text{for} \ \ k - j = even, \ k \geq j + 2, \tag{A.5b}$$

$$\langle T_j, D^3 T_k \rangle = \sum_{i=0}^{l=k-2} \frac{1}{c_i} k(k^2 - l^2)[\pi l],$$

$$\text{for} \ \begin{cases} k - l = even, & k \geq l + 2 \\ l - j = odd, & l \geq j + 1 \end{cases}, \tag{A.5c}$$

$$\langle T_j, D^4 T_k \rangle = \sum_{i=0}^{l=k-2} \frac{1}{c_i} k(k^2 - l^2) \left[l(l^2 - j^2)\frac{\pi}{2} \right],$$

$$\text{for} \ \begin{cases} k - l = even, \ k \geq l + 2 \geq j + 4 \\ i - j = even, & l \geq j + 2 \end{cases}. \tag{A.5d}$$

The integral of the Chebyshev polynomial $I_k(\hat{y}) = \int_{-1}^{\hat{y}} T_k(\hat{y}) d\hat{y}$ can be evaluated analytically resulting in

$$I_0(\hat{y}) = T_1(\hat{y}) + 1, \tag{A.6a}$$

$$I_1(\hat{y}) = \frac{T_2(\hat{y}) - 1}{4}. \tag{A.6b}$$

$$I_k(\hat{y}) = \frac{1}{2}\left[\frac{T_{k+1}(\hat{y}) - (-1)^{k+1}}{k+1} - \frac{T_{k-1}(\hat{y}) - (-1)^{k-1}}{k-1} \right], \qquad k > 1. \tag{A.6c}$$

Appendix B. Solution for the long wavelength corrugations ($\alpha \to 0$) placed at the lower plate.

This Appendix provides definitions of various coefficients used in the development of analytic solution for the long wavelength corrugations.

Coefficients used in Eq. (3.3.2) in Chapter 3:

$$F_1 = \frac{\eta_{xx}}{\eta_x^2 + \eta_y^2} = \alpha^2 \frac{2y_b^2\sin^2\xi - y_b G \cos\xi}{4}(\eta - 1) + O(\alpha^4), \tag{B.1}$$

$$F_2 = \frac{\eta_x}{\eta_x^2 + \eta_y^2} = -\alpha \frac{y_b G \sin\xi}{4}(\eta - 1) + O(\alpha^3),$$

$$F_3 = \frac{\eta_y}{\eta_x^2 + \eta_y^2} = \frac{G}{2} - \alpha^2 \frac{y_b^2 G \sin^2\xi}{8}(\eta - 1)^2 + O(\alpha^4),$$

$$F_4 = \frac{2\alpha \eta_x}{\eta_x^2 + \eta_y^2} = -\alpha^2 \frac{y_b G \sin\xi}{2}(\eta - 1) + O(\alpha^4),$$

$$F_5 = \frac{\alpha^2}{\eta_x^2 + \eta_y^2} = \alpha^2 \frac{G^2}{4} + O(\alpha^4),$$

$$F_6 = \frac{\alpha}{\eta_x^2 + \eta_y^2} = \alpha \frac{G^2}{4} + O(\alpha^3),$$

$$F_7 = \eta_x = -\alpha \frac{y_b \sin\xi}{G}(\eta - 1),$$

$$F_8 = \eta_y = \frac{2}{G},$$

$$F_9 = \frac{1}{\eta_x^2 + \eta_y^2} = \frac{G^2}{4} - \alpha^2 \left(\frac{y_b G \sin\xi}{4}\right)^2 (\eta - 1)^2 + O(\alpha^4),$$

$$G = 2 - y_b \cos\xi,$$

Coefficients used in Eqs (3.3.10) in Chapter 3:

$$k_1 = (52y_b^2 + 64)\eta^5 + (-260y_b^2 - 320)\eta^4 + (88y_b^2 + 192)\eta^3 + (328y_b^2 + 320)\eta^2 + \tag{B.2}$$
$$(-140y_b^2 - 256)\eta - 68y_b^2 - 320,$$

$$k_2 = (-4y_b^3 - 16y_b)\eta^5 + (20y_b^3 + 80y_b)\eta^4 + (8y_b^3 + 416y_b)\eta^3 + (-40y_b^3 -$$
$$544y_b)\eta^2 + (-4y_b^3 - 400y_b)\eta + 20y_b^3 + 464y_b,$$

$$k_3 = (-4y_b^2)\eta^5 + (20y_b^2)\eta^4 + (-184y_b^2)\eta^3 + (152y_b^2)\eta^2 + (188y_b^2)\eta - 172y_b^2,$$

$$k_4 = (y_b^3)\eta^5 + (-5y_b^3)\eta^4 + (22y_b^3)\eta^3 + (-14y_b^3)\eta^2 + (-23y_b^3)\eta + 19y_b^3,$$

$$k_5 = (-5y_b^3 - 80y_b)\eta^5 + (25y_b^3 + 400y_b)\eta^4 + (-14y_b^3 - 224y_b)\eta^3 + (-26y_b^3 -$$
$$416y_b)\eta^2 + (19y_b^3 + 304y_b)\eta + 16y_b,$$

$$k_6 = 5(y_b^4 + 36y_b^2 + 64)(\eta^7 - 7\eta^6 - \frac{21}{5}\eta^5 + 35\eta^4 + 7\eta^3 - 105\eta^2 + \frac{51}{5}\eta + 77),$$

$$k_7 = -537600\eta^3 + 1612800\eta^2 + 537600\eta - 1612800,$$

$$k_8 = -80(y_b^3 + 7y_b)(\eta^7 - 7\eta^6 - \frac{21}{5}\eta^5 + 35\eta^4 + 7\eta^3 - 105\eta^2 + \frac{51}{5}\eta + 77),$$

$$k_9 = -134400y_b(\eta^3 - 3\eta^2 - \eta + 3),$$

$$k_{10} = 10(y_b^4 + 30y_b^2)(\eta^7 - 7\eta^6 - \frac{21}{5}\eta^5 + 35\eta^4 + 7\eta^3 - 105\eta^2 + \frac{51}{5}\eta + 77),$$

$$k_{11} = -65y_b^3(\eta^7 - 7\eta^6 - \frac{21}{5}\eta^5 + 35\eta^4 + 7\eta^3 - 105\eta^2 + \frac{51}{5}\eta + 77),$$

$$k_{12} = 5y_b^4(\eta^7 - 7\eta^6 - \frac{21}{5}\eta^5 + 35\eta^4 + 7\eta^3 - 105\eta^2 + \frac{51}{5}\eta + 77),$$

$$k_{13} = -15(y_b^3 + \frac{16}{3}y_b)(\eta^7 - 7\eta^6 - \frac{21}{5}\eta^5 + 35\eta^4 + 7\eta^3 - 105\eta^2 + \frac{51}{5}\eta + 77),$$

$$k_{14} = 403200y_b(\eta^3 - 3\eta^2 - \eta + 3),$$

Appendix C. Solution for the small corrugation amplitude ($y_b \rightarrow 0$) with corrugations placed at the lower plate.

The unknowns are represented in the form of power expansions in terms of the corrugation amplitude of the form

$$[u, v, \theta, P] = [u_0, v_0, \theta_0, P_0] + y_b[u_1, v_1, \theta_1, P_1] + O(y_b{}^2), \tag{C.1}$$

the expansions are substituted into (3.2.5) in Chapter 3 and the leading order terms are extracted resulting in the following system

$$\frac{\partial u_0}{\partial x} + \frac{\partial v_0}{\partial y} = 0, \quad \frac{\partial p_0}{\partial x} = 0 \quad -\frac{\partial p_0}{\partial y} + Pr^{-1}\theta_0 = 0, \quad Pr^{-1}\nabla^2\theta_0 = 0. \tag{C.2}$$

The system of order $O(y_b{}^1)$ has the form of

$$\frac{\partial u_1}{\partial x} + \frac{\partial v_1}{\partial y} = 0, \quad -\frac{\partial p_1}{\partial x} + \nabla^2 u_1 = 0, \quad -\frac{\partial p_1}{\partial y} + \nabla^2 v_1 + Pr^{-1}\theta_1 = 0, \tag{C.3}$$

$$Pr^{-1}\nabla^2\theta_1 - v_1\frac{\partial\theta_0}{\partial y} = 0.$$

Use of expansions (C.1) in the boundary conditions leads to the following expressions:

$$y = 1: \tag{C.4}$$
$$u_0 + y_b u_1 + O(y_b{}^2) = 0, \ v_0 + y_b v_1 + O(y_b{}^2) = 0, \ \theta_0 + y_b\theta_1 + O(y_b{}^2) = 0,$$

$$y = -1 + y_b\cos(\alpha x): \tag{C.5}$$
$$u_0 + y_b u_1 + O(y_b{}^2) = 0, \ v_0 + y_b v_1 + O(y_b{}^2) = 0, \ \theta_0 + y_b\theta_1 + O(y_b{}^2) = Ra.$$

Transfer of (C.5) into the mean plate position results in the following form of these boundary conditions:

$y = -1$: (C.6)

$$u_0 + \frac{\partial u_0}{\partial y} y_b \cos(\alpha x) + y_b u_1 + O(y_b{}^2) = 0,$$

$$v_0 + \frac{\partial v_0}{\partial y} y_b \cos(\alpha x) + y_b v_1 + O(y_b{}^2) = 0,$$

$$\theta_0 + \frac{\partial \theta_0}{\partial y} y_b \cos(\alpha x) + y_b \theta_1 + O(y_b{}^2) = Ra.$$

Boundary conditions for the leading-order system have the form of

$y = 1$: $u_0 = 0, v_0 = 0, \theta_0 = 0,$ (C.7)

$y = -1$: $u_0 = 0, v_0 = 0, \theta_0 = Ra,$ (C.8)

and the boundary condition for system of order $O(y_b{}^1)$ have the form of

$at\ y = 1$: $u_1 = 0, v_1 = 0, \theta_1 = 0,$ (C.9)

$at\ y = -1$: $u_1 = 0, v_1 = 0, \theta_1 = \frac{Ra}{2} \cos(\alpha x).$ (C.10)

Solution of (C.2) subject to (C.7) - (C.8) has the following form

$$u_0 = 0, \qquad v_0 = 0, \qquad \theta_0 = \frac{Ra}{2}(1 - y), \qquad p_0 = \frac{Ra}{2\ Pr}\left(y - \frac{1}{2}y^2\right). \qquad \text{(C.11)}$$

Solution of (C.3) subject to (C.9) and (C.10) is assumed to be of the form

$$[v_1, \theta_1, P_1] = [\widehat{v_1}, \widehat{\theta_1}, \widehat{P_1}](y) \cos(\alpha x), \qquad u_1 = \widehat{u_1}(y) \sin(\alpha x). \qquad \text{(C.12)}$$

Substitution of (C.12) into (C.3) and elimination of $\widehat{u_1}, \widehat{\theta_1}, \widehat{P_1}$ leads to a single 6th order equations for $\widehat{v_1}$ in the following form

$$(D^2 - \alpha^2)^3 \widehat{v_1} = -\alpha^2 \frac{Ra}{2} \widehat{v_1} \qquad \text{(C.13)}$$

subject to boundary conditions of the form

$$y = 1 \quad : \quad \widehat{v_1} = 0, \quad D\widehat{v_1} = 0, \quad (D^2 - \alpha^2)^2\,\widehat{v_1} = 0, \tag{C.14}$$

$$y = -1 \quad : \quad \widehat{v_1} = 0, \quad D\widehat{v_1} = 0, \quad (D^2 - \alpha^2)^2\widehat{v_1} = \alpha^2\frac{Ra}{2Pr} \tag{C.15}$$

where $D = d/dy$. Solution of (C.13) - (C.15) can be expressed in terms of exponentials $e^{\varepsilon y}$ with the exponents ε defined by the roots of the following polynomial

$$(\varepsilon^2 - \alpha^2)^3 = -\alpha^2\frac{Ra}{2}, \tag{C.16}$$

which have the following forms

$$\varepsilon_{1,2} = \mp\alpha\sqrt{1 - (\frac{Ra}{2\alpha^4})^{\frac{1}{3}}}, \tag{C.17}$$

$$\varepsilon_{3,4} = \mp\alpha\sqrt{1 + \frac{1}{2}(1 + i\sqrt{3})(\frac{Ra}{2\alpha^4})^{\frac{1}{3}}},$$

$$\varepsilon_{5,6} = \mp\alpha\sqrt{1 + \frac{1}{2}(1 - i\sqrt{3})(\frac{Ra}{2\alpha^4})^{\frac{1}{3}}}.$$

The solution has the form of

$$\widehat{v_1} = \sum_{k=1}^{6} c_k e^{\varepsilon_k y} \tag{C.18}$$

where all c_k's are determined numerically from the boundary conditions. The remaining unknowns are determined using the following formulae

$$\widehat{u_1} = -\frac{1}{\alpha}D\widehat{v_1}, \qquad \widehat{\theta_1} = \frac{Pr}{\alpha^2}(D^2 - \alpha^2)^2\widehat{v_1}, \qquad \widehat{P_1} = \frac{1}{\alpha^2}(D^3 - \alpha^2 D)\widehat{v_1}. \tag{C.19}$$

The range of applicability of the above solution can be determined from the plot of variations of solution error defined as

$$||Er||_{max} \stackrel{def}{=} \underbrace{sup}_{0 \leq x \leq \lambda, \ 0 \leq y \leq 1} |\phi_n(x,y) - \phi_a(x,y)|, \tag{C.20}$$

where ϕ stands for any flow quantity, as a function of y_b displayed in Fig. C.1.
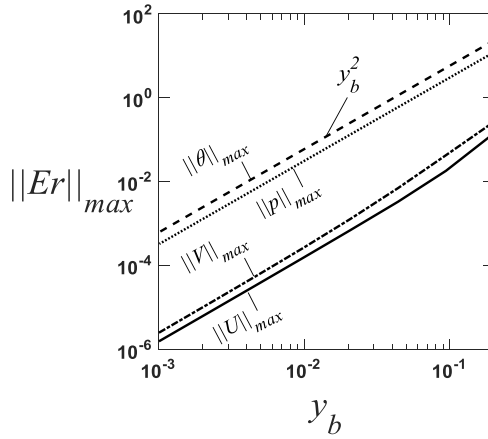

Figure C.1: Variations of the error of the small-amplitude solution $||Er||_{max}$ for u, v, θ, p (see Eq.C.20 for definition) as a function of the corrugation amplitude for $\alpha = 1.53$, $Ra = 200$, $y_t = 0$.

Physical quantities of interest are:

$$\sigma_{yp,L} = -\frac{3Ra}{4\,Pr} - y_b \left[\frac{Ra}{Pr} + \widehat{P}_1(-1)\right] \cos(\alpha x) + O(y_b{}^2), \tag{C.21}$$

$$Dif_1 = \sigma_{yp,L}(0) - \sigma_{yp,L}(\pi) = -2y_b \left[\frac{Ra}{Pr} + \widehat{P}_1(-1)\right] + O(y_b{}^3), \tag{C.22}$$

$$Dif_2 = H_{y,upper} - H_{y,lower} = -\frac{4y_b}{\pi}\left[\frac{Ra}{Pr} + \widehat{P}_1(-1)\right] + O(y_b{}^2), \tag{C.23}$$

$$Nu_{av} = \frac{Ra}{2} + O(y_b{}^2) \ , \qquad Nu_{loc,L} = \frac{Ra}{2} - y_b D\widehat{\theta}_1(-1)\cos(\alpha x) + O(y_b{}^2). \tag{C.24}$$

Appendix D. Solution for the long wavelength corrugations ($\alpha \to 0$) placed at both plates.

This Appendix provides definitions of various coefficients used in the development of analytic solution for the long wavelength corrugations as well as definitions of differential systems describing different levels of approximations.

Coefficients used in Eqs (3.3.2) in Chapter 3:

$$F_1 = \frac{\eta_{xx}}{\eta_x^2 + \eta_y^2} = \alpha^2 \frac{\left(2M_3^2 + M_1 G\right)\eta + M_2 G + 2M_3 M_4}{4} + O(\alpha^4), \qquad \text{(D.1)}$$

$$F_2 = \frac{\eta_x}{\eta_x^2 + \eta_y^2} = \alpha \frac{G(M_3 \eta + M_4)}{4} + O(\alpha^3),$$

$$F_3 = \frac{\eta_y}{\eta_x^2 + \eta_y^2} = \frac{G}{2} - \alpha^2 \frac{G(M_3 \eta + M_4)^2}{8} + O(\alpha^4),$$

$$F_4 = \frac{2\alpha \eta_x}{\eta_x^2 + \eta_y^2} = \alpha^2 \frac{G(M_3 \eta + M_4)}{2} + O(\alpha^4),$$

$$F_5 = \frac{\alpha^2}{\eta_x^2 + \eta_y^2} = \alpha^2 \frac{G^2}{4} + O(\alpha^4),$$

$$F_6 = \frac{\alpha}{\eta_x^2 + \eta_y^2} = \alpha \frac{G^2}{4} + O(\alpha^3),$$

$$F_7 = \eta_x = \alpha \frac{M_3 \eta + M_4}{G},$$

$$F_8 = \eta_y = \frac{2}{G},$$

$$F_9 = \frac{1}{\eta_x^2 + \eta_y^2} = \frac{G^2}{4} - \alpha^2 \frac{G^2(M_3 \eta + M_4)^2}{16} + O(\alpha^4),$$

$$G = 2 + M_1,$$

$$M_1 = y_t \cos(\xi + \Omega_C) - y_b \cos\xi,$$

$$M_2 = y_t \cos(\xi + \Omega_C) + y_b \cos\xi,$$

$$M_3 = y_t \sin(\xi + \Omega_C) - y_b \sin\xi,$$

$$M_4 = y_t \sin(\xi + \Omega_C) + y_b \sin\xi.$$

The leading-order systems are:

$O(\alpha^0)$ $\dfrac{\partial v_0}{\partial \eta} = 0,$ $\dfrac{\partial^2 u_0}{\partial \eta^2} - \dfrac{G}{2} v_0 \dfrac{\partial u_0}{\partial \eta} - \dfrac{G^2}{4} \dfrac{\partial p_{-1}}{\partial \xi} - \dfrac{G(M_3\eta + M_4)}{4} \dfrac{\partial p_{-1}}{\partial \eta} = 0,$ $\dfrac{\partial p_{-1}}{\partial \eta} = 0,$ (D.2a)

$$\dfrac{\partial^2 \theta_0}{\partial \eta^2} - \dfrac{\Pr G}{2} v_0 \dfrac{\partial \theta_0}{\partial \eta} = 0$$

$u_0(\xi, \pm 1) = 0,$ $v_0(\xi, \pm 1) = 0,$ $\theta_0(\xi, -1) = Ra,$ $\theta_0(\xi, 1) = 0,$ (D.2b)

$$\left. \dfrac{\partial P_{-1}}{\partial \xi} \right|_{mean} = 0.$$

$O(\alpha^1)$ $\dfrac{\partial v_1}{\partial \eta} = 0,$ $\dfrac{\partial^2 u_1}{\partial \eta^2} - \dfrac{G^2}{4} \dfrac{\partial p_0}{\partial \xi} - \dfrac{G(M_3\eta + M_4)}{4} \dfrac{\partial p_0}{\partial \eta} = 0,$ $-\dfrac{G}{2} \dfrac{\partial p_0}{\partial \eta} + \dfrac{G^2}{4 Pr} \theta_0 = 0,$ (D.3a)

$$\dfrac{\partial^2 \theta_1}{\partial \eta^2} - \dfrac{\Pr G}{2} v_1 \dfrac{\partial \theta_0}{\partial \eta} = 0,$$

$u_1(\xi, \pm 1) = 0,$ $v_1(\xi, \pm 1) = 0,$ $\theta_1(\xi, \pm 1) = 0,$ $\left. \dfrac{\partial P_0}{\partial \xi} \right|_{mean} = 0.$ (D.3b)

$O(\alpha^2)$ $\dfrac{\partial v_2}{\partial \eta} + \dfrac{(M_3\eta + M_4)}{2} \dfrac{\partial u_1}{\partial \eta} + \dfrac{G}{2} \dfrac{\partial u_1}{\partial \xi} = 0,$ $\dfrac{\partial^2 u_2}{\partial \eta^2} - \dfrac{G^2}{4} \dfrac{\partial p_1}{\partial \xi} - \dfrac{G(M_3\eta + M_4)}{4} \dfrac{\partial p_1}{\partial \eta} = 0,$ (D.4a-c)

$$-\dfrac{G}{2} \dfrac{\partial p_1}{\partial \eta} + \dfrac{G^2}{4 Pr} \theta_1 = 0,$$

$$\dfrac{\partial^2 \theta_2}{\partial \eta^2} + \dfrac{(2M_3^2 + M_1 G)\eta + M_2 G + 2 M_3 M_4}{4} \dfrac{\partial \theta_0}{\partial \eta} - \dfrac{\Pr G(M_3\eta + M_4)}{4} u_1 \dfrac{\partial \theta_0}{\partial \eta} - \dfrac{\Pr G}{2} v_2 \dfrac{\partial \theta_0}{\partial \eta} = 0,$$ (D.4d)

$u_2(\xi, \pm 1) = 0,$ $v_2(\xi, \pm 1) = 0,$ $\theta_2(\xi, \pm 1) = 0,$ $\left. \dfrac{\partial P_1}{\partial \xi} \right|_{mean} = 0.$ (D.4e)

Coefficients used in Eqs (3.5.2) - (3.5.4) in Chapter 3:

$L_u = 24 \left[y_t^2 y_b (\eta^2 + \frac{4}{3}\eta - \frac{1}{5}) cos^3 \Omega_C - \frac{1}{2} y_t^2 y_b (\eta^2 + \frac{4}{3}\eta - \frac{1}{5}) cos\Omega_C + \frac{8}{3} y_t y_b \eta \right] sin\Omega_C,$ (D.5)

$LS_{u,1} = -4 y_b y_t^2 (\eta^2 - 4\eta - \frac{1}{5}) cos^2\Omega_C - \left[y_t(3y_b^2 + y_t^2 + 16)\eta^2 + y_t(-4 y_b^2 + 4 y_t^2 + 64)\eta - \frac{3}{5} y_b^2 y_t - \frac{1}{5} y_t^3 - \frac{16}{5} y_t \right] cos\Omega_C + (y_b^3 + 4y_t^2 y_b + 16 y_b)(\eta^2 - 4\eta - \frac{1}{5}),$

$LC_{u,1} = \left[2 y_b y_t^2 \left(\eta^2 + 12\eta - \frac{1}{5} \right) cos\Omega_C - (y_b^2 y_t + y_t^3 + 16 y_t)\eta^2 - (20 y_b^2 y_t + 4 y_t^3 + 64 y_t)\eta + \frac{1}{5} y_b^2 y_t + \frac{1}{5} y_t^3 + \frac{16}{5} y_t \right] sin\Omega_C,$

$LS_{u,2} = 8 \left[-2 y_t^2 \left(\eta^2 + 4\eta - \frac{1}{5} \right) cos^2\Omega_C + 2 \left(\eta^2 - \frac{1}{5} \right) y_b y_t cos\Omega_C + (y_t^2 - y_b^2)\eta^2 + 4(y_b^2 + y_t^2)\eta + \frac{1}{5}(y_b^2 - y_t^2) \right],$

$$LC_{u,2} = 16y_t\left[-y_t(\eta^2+4\eta-\tfrac{1}{5})cos\Omega_C + y_b(\eta^2-\tfrac{1}{5})\right]sin\Omega_C,$$

$$LS_{u,3} = -4y_t^3\left(\eta^2+4\eta-\tfrac{1}{5}\right)cos^3\Omega_C - 3y_t\left[(y_b^2-y_t^2)\eta^2+\left(-\tfrac{4}{3}y_b^2-4y_t^2\right)\eta-\tfrac{1}{5}y_b^2+\tfrac{1}{5}y_t^2\right]cos\Omega_C + y_b^3(\eta^2-4\eta-\tfrac{1}{5}),$$

$$LC_{u,3} = 3\left[-\tfrac{4}{3}y_t^3\left(\eta^2+4\eta-\tfrac{1}{5}\right)cos^2\Omega_C + 2y_t^2y_b\left(\eta^2+\tfrac{4}{3}\eta-\tfrac{1}{5}\right)cos\Omega_C + y_t^3\left(\tfrac{1}{3}\eta^2+\tfrac{4}{3}\eta-\tfrac{1}{15}\right) - y_b^2y_t(\eta^2-\tfrac{4}{3}\eta-\tfrac{1}{5})\right]sin\Omega_C,$$

$$L_v = 2y_ty_b^2\left[(y_b+\tfrac{5}{2}y_t)\eta^3-\tfrac{5}{2}y_b\eta^2+(3y_b-\tfrac{61}{2}y_t)\eta-\tfrac{19}{2}y_b\right]cos^2\Omega_C - 5y_ty_b\left[(y_b^2+y_t^2+8)\eta^3+\tfrac{5}{2}(y_t^2-y_b^2)\eta^2+\tfrac{1}{5}(-y_b^2-y_t^2-168)\eta+\tfrac{1}{10}y_b^2-\tfrac{1}{10}y_t^2\right]cos\Omega_C +$$
$$\tfrac{1}{4}(5y_b^4-8y_ty_b^3+(10y_t^2+80)y_b^2+5y_t^4+80y_t^2)\eta^3+\tfrac{1}{4}(-25y_b^4+20y_b^3y_t+25y_t^4-400y_b^2+400y_t^2)\eta^2+\tfrac{1}{4}(19y_b^4-24y_ty_b^3+(198y_t^2+304)y_b^2+19y_t^4+304y_t^2)\eta+\tfrac{1}{4}y_b^4+19y_ty_b^3-\tfrac{1}{4}y_t^4+4y_b^2-4y_t^2,$$

$$LS_{v,1} = -13y_t\left[-2y_ty_b(\eta^3-\tfrac{5}{13}\eta^2-\tfrac{125}{13}\eta-\tfrac{43}{13})+(y_b^2+y_t^2+\tfrac{16}{13})\eta^3+(-\tfrac{75}{13}y_b^2+5y_t^2+\tfrac{80}{13})\eta^2+(15y_b^2+\tfrac{35}{13}y_t^2-\tfrac{16}{13})\eta-\tfrac{69}{13}y_b^2-\tfrac{17}{13}y_t^2-\tfrac{80}{13}\right]sin\Omega_C,$$

$$LC_{v,1} = -26y_t^2y_b\left[\eta^3-\tfrac{5}{13}\eta^2-\tfrac{125}{13}\eta-\tfrac{43}{13}\right]cos^2\Omega_C + 39y_t\left[(y_b^2+\tfrac{1}{3}y_t^2+\tfrac{16}{39})\eta^3+(-\tfrac{5}{3}y_b^2+\tfrac{5}{3}y_t^2+\tfrac{80}{39})\eta^2+(-\tfrac{55}{39}y_b^2+\tfrac{35}{39}y_t^2-\tfrac{16}{39})\eta-\tfrac{80}{39}+\tfrac{17}{39}y_b^2-\tfrac{17}{39}y_t^2\right]cos\Omega_C - 13y_b\left[(y_b^2+y_t^2+\tfrac{16}{13})\eta^3+(-5y_b^2+\tfrac{75}{13}y_t^2-\tfrac{80}{13})\eta^2+(\tfrac{35}{13}y_b^2+15y_t^2-\tfrac{16}{13})\eta+\tfrac{17}{13}y_b^2+\tfrac{69}{13}y_t^2+\tfrac{80}{13}\right],$$

$$LS_{v,2} = 2y_t\left\{2y_t^2y_b\left(\eta^3-\tfrac{5}{2}\eta^2-21\eta-\tfrac{19}{2}\right)cos^2\Omega_C - 3y_t\left[\tfrac{1}{3}y_t^2(\eta+5)(\eta^2-1)+(y_b^2+\tfrac{4}{3})\eta^3+(-\tfrac{10}{3}y_b^2+\tfrac{20}{3})\eta^2-(y_b^2+\tfrac{100}{3})\eta-\tfrac{14}{3}y_b^2-\tfrac{116}{3}\right]cos\Omega_C + y_b\left[y_t^2\left(\eta^3+\tfrac{15}{2}\eta^2+19\eta+\tfrac{9}{2}\right)+(y_b^2+4)\eta^3-\tfrac{15}{2}y_b^2\eta^2+(19y_b^2+60)\eta-\tfrac{9}{2}y_b^2\right]\right\}sin\Omega_C,$$

$$LC_{v,2} = -4y_t^3y_b\left(\eta^3-\tfrac{5}{2}\eta^2-21\eta-\tfrac{19}{2}\right)cos^3\Omega_C + y_t\left[(2\eta^3+10\eta^2-2\eta-10)y_t^3+y_t(6y_b^2\eta^3-20y_b^2\eta^2-6y_b^2\eta-28y_b^2+8\eta^3+40\eta^2-200\eta-232)+y_b^3(\eta^3-\tfrac{5}{2}\eta^2+3\eta-\tfrac{19}{2})\right]cos^2\Omega_C + \tfrac{1}{2}y_t^4(-2\eta^3-10\eta^2+2\eta+10)+\tfrac{1}{2}y_t^2[-8\eta^3+40(y_b^2-1)\eta^2+200\eta+56y_b^2+232]-y_b^3y_t(\eta^3-\tfrac{5}{2}\eta^2+3\eta-\tfrac{19}{2})+y_b^2(\eta-1)[(y_b^2+4)\eta^2+(-4y_b^2-16)\eta-5y_b^2-116],$$

$$LS_{v,3} = 3y_t\left[\tfrac{4}{3}y_t^2(\eta^3+5\eta^2+47\eta+43)cos^2\Omega_C - 2y_ty_b\left(\eta^3+\tfrac{5}{3}\eta^2-\tfrac{19}{3}\eta+\tfrac{43}{3}\right)cos\Omega_C - \tfrac{1}{3}y_t^2(\eta^3+5\eta^2+47\eta+43)+y_b^2(\eta^3-\tfrac{5}{3}\eta^2-\tfrac{19}{3}\eta-\tfrac{43}{3})\right]sin\Omega_C,$$

$$LC_{v,3} = -4y_t^3(\eta^3 + 5\eta^2 + 47\eta + 43)cos^3\Omega_C + 6y_t^2 y_b\left(\eta^3 + \tfrac{5}{3}\eta^2 - \tfrac{19}{3}\eta + \tfrac{43}{3}\right)cos^2\Omega_C -$$

$$3y_t\left[y_t^2(-\eta^3 - 5\eta^2 - 47\eta - 43) + y_b^2(\eta^3 - \tfrac{5}{3}\eta^2 - \tfrac{19}{3}\eta - \tfrac{43}{3})\right]cos\Omega_C +$$

$$y_b[y_t^2(-3\eta^3 - 5\eta^2 + 19\eta - 43) + y_b^2(\eta^3 - 5\eta^2 + 47\eta - 43)],$$

$$LS_{v,4} = 3y_t^2\left\{\tfrac{2}{3}y_t^2(\eta^3 + 5\eta^2 + 23\eta + 19)cos^3\Omega_C - \tfrac{4}{3}y_t y_b\left(\eta^3 + \tfrac{5}{2}\eta^2 + 3\eta + \right.\right.$$

$$\left.\tfrac{19}{2}\right)cos^2\Omega_C + \left[-\tfrac{1}{3}y_t^2(\eta^3 + 5\eta^2 + 23\eta + 19) + y_b^2(\eta^3 - \tfrac{11}{3}\eta)\right]cos\Omega_C +$$

$$\left.\tfrac{1}{3}y_t y_b(\eta^3 + \tfrac{5}{2}\eta^2 + 3\eta + \tfrac{19}{2})\right\}sin\Omega_C,$$

$$LC_{v,4} = -2y_t^4(\eta^3 + 5\eta^2 + 23\eta + 19)cos^4\Omega_C + 4y_t^3 y_b\left(\eta^3 + \tfrac{5}{2}\eta^2 + 3\eta + \tfrac{19}{2}\right)cos^3\Omega_C -$$

$$2y_t\left[y_t^3(-\eta^3 - 5\eta^2 - 23\eta - 19) + \tfrac{3}{2}y_b^2 y_t(\eta^3 - \tfrac{11}{3}\eta) + y_b^3(\eta^3 - \tfrac{5}{2}\eta^2 + 3\eta - \right.$$

$$\left.\tfrac{19}{2})\right]cos^2\Omega_C + y_t y_b\left[y_t^2(-3\eta^3 - \tfrac{15}{2}\eta^2 - 9\eta - \tfrac{57}{2}) + y_b^2(\eta^3 - \tfrac{5}{2}\eta^2 + 3\eta - \right.$$

$$\left.\tfrac{19}{2})\right]cos\Omega_C + \tfrac{1}{4}y_t^4(-\eta^3 - 5\eta^2 - 23\eta - 19) + \tfrac{1}{4}y_t^2(6y_b^2\eta^3 - 22y_b^2\eta) +$$

$$2y_b^3 y_t(\eta^3 - \tfrac{5}{2}\eta^2 + 3\eta - \tfrac{19}{2}) - \tfrac{1}{4}y_b^4(\eta^3 - 5\eta^2 + 23\eta - 19),$$

$$LS_{v,5} = LC_{v,5} = LS_{v,6} = 0,$$

$$LC_{v,6} = \tfrac{1}{2}y_b^3 y_t(2\eta^3 - 5\eta^2 + 6\eta - 19)sin^2\Omega_C,$$

$$L_p = -6y_t^2 cos^2\Omega_C - 8y_t\left(-\tfrac{5}{4}\eta^2 + \tfrac{5}{2}\eta + y_b + \tfrac{1}{4}\right)cos\Omega_C - 10(y_b - 2)\eta^2 + 20(y_b -$$

$$2)\eta - 6y_b^2 + 2y_b.$$

$$LS_{p,1} = y_t(5\eta^2 - 10\eta - 9)(-y_t cos\Omega_C + y_b - 2)sin\Omega_C,$$

$$LC_{p,1} = 5(-y_t cos\Omega_C + y_b - 2)\left[-y_t\left(\eta^2 - 2\eta - \tfrac{9}{5}\right)cos\Omega_C + y_b\left(\eta^2 - 2\eta + \tfrac{11}{5}\right)\right],$$

Coefficients $L_\theta, LS_{\theta,n}, LC_{\theta,n}$ are not given due to their length. Instead, θ_2 is expressed combining all polynomials of η in the form shown below as this is more convenient for computations:

$$\theta_2 = \frac{Ra}{8}[Z_1\eta^7 + Z_2\eta^6 + Z_3\eta^5 + Z_4\eta^4 + Z_5\eta^3 + Z_6\eta^2 + Z_7\eta + Z_8], \tag{D.6a}$$

$$\begin{bmatrix}Z_1\\Z_2\\Z_3\\Z_4\\Z_5\\Z_6\\Z_7\\Z_8\end{bmatrix} = \left(RaG^3\begin{bmatrix}\frac{-1}{80640}&0&\frac{1}{26880}&0\\0&\frac{-1}{11520}&0&\frac{1}{3840}\\\frac{1}{19200}&0&\frac{-1}{6400}&0\\0&\frac{1}{2304}&0&\frac{-1}{768}\\\frac{-1}{11520}&0&\frac{1}{3840}&0\\0&\frac{-1}{768}&0&\frac{1}{256}\\\frac{19}{403200}&0&\frac{-19}{134400}&0\\0&\frac{11}{11520}&0&\frac{-11}{3840}\end{bmatrix} + \begin{bmatrix}0&0&0&0\\0&0&0&0\\0&0&0&0\\0&0&0&0\\\frac{1}{6}&0&\frac{1}{3}&0\\0&\frac{1}{2}&0&1\\\frac{-1}{6}&0&\frac{-1}{3}&0\\0&\frac{-1}{2}&0&-1\end{bmatrix}\right) \times \begin{bmatrix}M_1 G\\M_2 G\\M_3^2\\M_3 M_4\end{bmatrix}. \tag{D.6b}$$

Coefficients of Eqs (3.5.6) in Chapter 3:

$$L_{vL} = -5y_t y_b sin\Omega_C, \tag{D.7}$$

$$LS_{vL,1} = 12y_b + 8y_t cos\Omega_C, \qquad LS_{vL,2} = 4y_t^2 cos^2\Omega_C + y_t y_b cos\Omega_C - 3y_b^2 - 2y_t^2,$$

$$LC_{vL,1} = 8y_t sin\Omega_C, \qquad LC_{vL,2} = 2y_t^2 sin(2\Omega_C) + y_t y_b sin\Omega_C,$$

$$L_{vU} = -5y_t y_b sin\Omega_C,$$

$$LS_{vU,1} = 8y_b + 12y_t cos\Omega_C, \qquad LS_{vU,2} = 6y_t^2 cos^2\Omega_C - y_t y_b cos\Omega_C - 2y_b^2 - 3y_t^2,$$

$$LC_{vU,1} = 12y_t sin\Omega_C, \qquad LC_{vU,2} = 3y_t^2 sin(2\Omega_C) - y_t y_b sin\Omega_C,$$

$$L_{pL} = -6y_t(2 - y_b + y_t\, cos\, \Omega_C)sin\Omega_C,$$

$$LS_{pL,1} = -6y_t^2 cos^2\Omega_C + y_t(-16y_b + 56)cos\Omega_C - 12y_b^2 - 3y_t^2 - 56y_b + 120,$$

$$LS_{pL,2} = y_t(-32y_b + 12)cos\Omega_C + 26y_b^2 + 3y_t^2 - 52y_b,$$

$$LC_{pL,1} = -3y_t^2 sin(2\Omega_C), \qquad LC_{pL,2} = -12y_t y_b sin\Omega_C,$$

$$L_{pU} = 6y_b(2 - y_b + y_t\, cos\, \Omega_C)sin\Omega_C,$$

$$LS_{pU,1} = 12y_t^2 cos^3\Omega_C + (16y_t y_b + 24y_t)cos^2\Omega_C + (12y_b^2 - 24y_b + 40)cos\Omega_C,$$

$$LS_{pU,2} = 28y_t^2 cos^3\Omega_C - (22y_t y_b - 56y_t)cos^2\Omega_C - (14y_t^2 + 6y_b^2 - 12y_b)cos\Omega_C -$$
$$28y_t + 14y_t y_b,$$

$$LC_{pU,1} = 12\left[y_t^2 cos^2\Omega_C + \left(\frac{4}{3}y_t y_b + 2y_t\right)cos\Omega_C + y_b^2 - 2y_b + \frac{10}{3}\right]sin\Omega_C,$$

$$LC_{pU,2} = (28y_t cos\Omega_C + 6y_b)(2 - y_b + y_t\, cos\, \Omega_C)sin\Omega_C.$$

Coefficients of Eqs (3.5.11) in Chapter 3:

$$L_1 = -6y_t(2 - y_b + y_t\, cos\, \Omega_C)sin\Omega_C, \tag{D.8}$$

$$L_2 = -(2 - y_b + y_t\, cos\, \Omega_C)(-6y_t cos\Omega_C + 26y_b),$$

$$L_3 = -6y_t^2 cos^2\Omega_C + y_t(28 - 8y_b)cos\Omega_C - 6y_b^2 - 28y_b + 60,$$

$$L_4 = 14y_t(2 - y_b + y_t\, cos\, \Omega_C)sin\Omega_C,$$

$$L_5 = -(2 - y_b + y_t\, cos\, \Omega_C)(14y_t cos\Omega_C + 6y_b),$$

$$L_6 = -6y_t^2 cos^2\Omega_C - y_t(8y_b + 12)cos\Omega_C - 6y_b^2 + 12y_b - 20.$$

Curriculum Vitae

Seyed Arman Abtahi

Education

Jan 2015 – Feb 2017	**MESc., Mechanical Engineering** Western University, London, Canada Emphasis on Flow Control, Hydrodynamic Stability, and Convection	GPA: 94.75/100 (3.93/4)
Sept 2010 – July 2014	**B.Sc., Mechanical Engineering** Isfahan University of Technology, Isfahan, Iran Emphasis on Fluids, HVAC, Thermodynamics, Control systems, and Energy Systems.	GPA: 18.02/20 (3.96/4)

Publications

- A. Abtahi, M. Z. Hossain, J. M. Floryan, Spectrally Accurate Algorithm for Analysis of Convection in Corrugated Conduits, Journal of Computers and Mathematics with Applications, 72 (2016) 2636–2659.
- A. Abtahi, J. M. Floryan, Natural Convection in a Corrugated Slot, Journal of Fluid Mechanics, doi:10.1017/jfm.2017.73.
- A. Abtahi, J. M. Floryan, On the Analysis of Flow in Heated and Corrugated Conduits, International Congress of Theoretical and Applied Mechanics, Montreal, Canada, (August 2016).
- A. Abtahi, J. M. Floryan, Natural Convection and Thermal Drift, (Submitted).

Work and Teaching Experiences

Research Assistant (2015-2017)	**Complex Flow Systems Laboratory,** Western University, London, Ontario, Canada
Teaching Assistant (2015-2017)	**Running Tutorials, and Lab sessions**, Western University, London, Ontario, Canada Heat Transfer, Fluid Mechanics, Fluid Machinery, Thermodynamics.

Honors and Awards

2015-2017	- Western Graduate Research Scholarship, Western University, Ontario, Canada.